Investigation of the role of prolyl isomerase A in protein misfolding associated with neurodegenerative diseases

Dissertation

for the award of the degree

'Doctor rerum naturalium' (Dr.rer.nat.)

of the Georg-August-Universität Göttingen

within the doctoral degree program of Biology

of the Georg-August University School of Science(GAUSS)

Submitted by

Maria Babu

from Kerala, India.

Göttingen, 2022

Thesis Committee

Prof. Dr. Markus Zweckstetter
Structure Determination of Proteins Using NMR, Max-Planck-Institute for Multidisciplinary Sciences, Göttingen
Translational Structural Biology, German Center for Neurodegenerative Disease, Göttingen

Prof. Dr. Tiago Outeiro
Department of Experimental Neurodegeneration, University Medical Center, Göttingen

Dr. Stefan Karpitschka
Max-Planck-Institute for Dynamics and Self-Organization, Göttingen

Members of the examination board

Reviwer: Prof. Dr. Markus Zweckstetter
Second Reviewer: Prof. Dr. Tiago Outeiro

Further members of the examination board

Dr. Stefan Karpitschka
Max-Planck-Institute for Dynamics and Self-Organization, Göttingen

Prof. Dr. Kai Tittmann
Department of Molecular Enzymology, Center of Molecular Biosciences, Göttingen

Prof. Dr. Stefan Pöhlmann
Infection Biology Unit, German Primate Center, Göttingen

Dr. Johannes Söding
Quantitative Biology and Bioinformatics, Max-Planck-Institute for Multidisciplinary Sciences, Göttingen

Date of the oral examination: January 20, 2023

Acknowledgments

First of all, I would like to express my deepest gratitude to my supervisor Prof. Markus Zweckstetter for giving me the great opportunity to work on exciting projects in a motivating atmosphere. Thank you for your patience, insightful guidance, and constructive feedback which enabled me to gain new perspectives and grow better as a scientist. The enthusiasm you had for the projects, and the encouragement you provided were truly motivating.

I am very grateful to Prof. Tiago Outeiro and Dr. Stefan Karpitschka, for being part of my thesis advisory committee, for providing useful feedback, and for the words of encouragement during every other meeting.

My sincere thanks to Dr. Stefan Becker for performing crystallographic studies and for the helpful discussions.

Many thanks to Kerstin Overkamp and Sol Cima for providing the peptides and proteins I needed for my work.

I am deeply thankful to my immediate supervisor Dr. Filippo Favretto. In the early years, with little knowledge of Biology, I relied on your support and reassurance for a long time, and you have always been there to help me. I am grateful for all you taught me, for the guidance you gave me, and for always looking out for me inside and outside the lab.

I am very grateful to all my wonderful colleagues in the lab- Alain, Marija, David, Timo, Adriana, Pijush, Tina, Antonia, Taekyung, Christian, Jeff, Lisa, Conny, Sol, Matthew, Gwladys, Milan, Zheng, Irina, Anton, Reshma, Debdeep and Fiamma. I would like to thank you all for your constant support, encouragement, and valuable suggestions that helped me power through challenging situations and learn better. Thanks for being part of my happiest moments and helping me through the frustrating ones. A special thanks to Dr. Marija Rankovic for teaching me everything about phase separation and for your encouraging words in challenging situations. Special thanks also to Dr. Alain Ibanez de Opakua for being a great support all through these years. Thank you for all the insightful discussions, I have learned from you how to look at things in a realistic way.

Special thanks to the great effort of Conny and Sol, our lab coordinators, in order to provide a highly organized atmosphere to work. Through these years, their constant availability and willingness to help have made things easier.

My sincere thanks go to everyone at the NMR2 department at MPI-NAT, for their support at the instruments and for the interesting discussions.

I am grateful to all my friends in Goettingen, especially Revathi, Amal, DV, Harry, Akshay, and Lakshmi, who made this journey overall a delightful one. Thank you for making me feel home away from home.

Finally, my deepest gratitude to my family-Appa, Amma, and Kunju for being my constant support throughout this journey. Thank you for continually reminding me of my capabilities, and for always being proud of me.

Abstract

Misfolded proteins and disrupted homeostasis are key characteristics of neurodegenerative diseases. There is a strong association between intrinsically disordered proteins and pathogenic misfolding in neurodegenerative diseases. As a result of their exposed amino acid chain, intrinsically disordered proteins are highly vulnerable to aberrant interactions, which are frequently triggered by mutations or any cellular perturbations that modulate their functional conformation. Although abnormal interactions and misfolding start with a few intrinsically disordered proteins in most diseases, many interactor proteins essential for proper cellular function eventually co-aggregate with the misfolding proteins. Loss of crucial proteins into aggregates leads to disrupted homeostasis and neuronal death.

Prolyl isomerases are a class of chaperones that bind to proline residues and enhance their cis/trans isomerization rate. Through their unique action on proline residues, prolyl isomerases play an essential role in maintaining protein homeostasis: they assist in the de novo protein folding of globular proteins and regulate the misfolding of intrinsically disordered proteins. In this work, we investigated the involvement of prolyl isomerase A (PPIA)-the most abundant kind of prolyl isomerase- in two different cases of pathogenic protein misfolding: a) protein misfolding in C9orf72-Amyotrophic Lateral Sclerosis (ALS)/Frontotemporal Dementia (FTD) and b) protein misfolding from biomolecular condensates.

In the first part of the thesis, we uncovered a novel neurotoxic pathway that results from the inhibition of PPIA in the neurodegenerative diseases-ALS and FTD. Hexanucleotide repeat expansion mutation in the C9orf72 gene is the most common cause of familial ALS and FTD. The toxicity of this mutation is attributed to the aberrant interactions of the disordered dipeptide repeat polymers that are translated from the repeat expanded region. Here, we showed that proline/arginine repeat polymers bind to the catalytic activity site of PPIA. As a result, these repeats inhibited PPIA's de novo protein folding activity, which is essential in maintaining cellular homeostasis. NMR spectroscopy and X-Ray crystallography studies revealed the structural basis of proline/arginine repeat polymer binding to PPIA. It provided insights into the importance of the specific combination of proline and arginine residues in the inhibition of PPIA activity. In summary, our data revealed a pathway that can lead to disrupted homeostasis in C9orf72-ALS/FTD due to the loss of function of PPIA.

In the second part, we investigated the regulatory role of prolyl isomerase on biomolecular condensation. Biomolecular condensates are enriched in proline-rich intrinsically disordered

proteins, many of which are involved in neurodegeneration associated misfolding. The high concentration of proteins inside the condensate puts them at increased risk of undergoing pathogenic interactions, emphasizing the need for tight regulation. Despite the abundance of proline residues in intrinsically disordered sequences, the regulatory role of prolyl isomerases on the liquid-liquid phase separation of intrinsically disordered proteins remains unknown. Our study shows that PPIA can migrate into self-assembled liquid-like droplets of Alzheimer's disease protein Tau and complex coacervates of a proline/arginine repeat polymer with RNA. At increased concentrations of PPIA, the two proline-rich condensates dissolved back into the mixed state. Binding and isomerization studies of PPIA with the proline/arginine repeat polymer and Tau protein provided information into the mechanism of chaperoning of liquid-liquid phase separation by PPIA. Our studies established a regulatory function of PPIA on the liquid-liquid phase separation of proline-rich intrinsically disordered proteins.

Publications

The whole of the research in this thesis has already been published (listed below). The excerpts directly taken from these publications are represented in italic font. Figures reprinted from these publications are indicated in their corresponding legends.

Peptidyl Prolyl Isomerase A Modulates the Liquid-Liquid Phase Separation of Proline-Rich IDPs

Journal of the American Chemical Society 144.35, 16157-16163 (2022) ; DOI: https://doi.org/10.1021/jacs.2c07149

Authors: *Maria Babu, Filippo Favretto, Marija Rankovic and Markus Zweckstetter*

Author Contributions: *MB produced protein, designed and conducted NMR experiments, LLPS assays, and FRAP experiments, as well as acquired and analyzed data; FF supervised NMR experiments; MR supervised microscopy experiment;. MZ designed and supervised the project. MB and MZ wrote the paper.*

Proline/arginine dipeptide repeat polymers derail protein folding in amyotrophic lateral sclerosis

Nature communications 12.1, 3396 (2021); DOI: https://doi.org/10.1038/s41467-021-23691-y

Authors: *Maria Babu, Filippo Favretto, Alain Ibáñez de Opakua, Marija Rankovic, Stefan Becker, Markus Zweckstetter*

Author Contributions: *M.B. prepared protein, designed and conducted folding assays, ITC and NMR experiments, as well as data acquisition and analysis; F.F. performed ITC, prepared protein, and supervised protein preparation as well as NMR experiments; A.I.d.O. and M.R. helped in experimental design; S.B. performed crystallization and determined the structure of the PPIA/PR20 complex; M.Z. designed and supervised the project. M.B., S.B., and M.Z. wrote the paper.*

Contents

1. Introduction 1
1.1. Neurodegenerative diseases 1
1.2. Protein misfolding and disrupted homeostasis in neurodegeneration 1
1.2.1. General aspects of protein misfolding in neurodegeneration 1
1.2.2. Disrupted homeostasis in C9orf72-ALS/FTD 4
1.2.3. Biomolecular condensates- protein misfolding interface in neurodegenerative diseases 7
1.3. Peptidyl prolyl isomerases and protein homeostasis 11
1.3.1. Peptidyl prolyl isomerase: mode of action 11
1.3.3. Peptidyl prolyl isomerase in protein folding and misfolding 13
1.4. Aims of the work 14
2. Materials and Methods 16
2.1 Materials 16
2.1.1. Chemicals 16
2.1.2. Equipment 18
2.1.3. Software 19
2.2. Protein and peptide synthesis 19
2.2.1. Expression and purification of PPIA 19
2.2.2. Expression and purification of Tau 20
2.2.3. Synthesis of dipeptide repeat polymers 22
2.3. RNase T1 protein refolding assay 22
2.3.1. Principle 22
2.3.2. Experimental condition 23
2.4. X- Ray crystallography 23
2.5. NMR spectroscopy 24
2.5.1. Introduction to NMR 24
2.5.2. Binding studies using NMR titration 30
2.5.3. Quantification of PPIA-enhanced isomerization in PR20 34
2.6. Isothermal titration calorimetry 36
2.6.1. Principle 36
2.6.2. Experimental protocol and analysis 37
2.7. LLPS assays 38
2.7.1. PR20/tRNA LLPS 38
2.7.2. Tau LLPS 39

2.8. FRAP 41
2.8.1. Principle 41
2.8.2. FRAP of PR20/tRNA droplets 41
2.8.3. FRAP of Tau droplets 41
2.8.4. Analysis 42
3. Results: Part 1 43
3.1. PR repeat polymers interact with prolyl isomerases in vivo 43
3.2. PR repeat polymers inhibit protein folding activity 43
3.3. PR repeat polymers bind to the active site of PPIA 45
3.4. PPIA does not interact with other proline or arginine containing dipeptide repeat polymers 46
3.5. Interaction of PPIA with PR repeat polymer depends on the repeat length 48
3.6. Structure of PR repeat polymer in complex with PPIA 49
4. Discussion: Part 1 52
4.1. PR repeat polymers disrupt protein homeostasis in C9orf72- ALS/FTD by inhibiting PPIA 52
4.2. Toxicity of PPIA/PR repeat polymer interaction will enhance with increase in the length of repeats 55
5. Results: Part 2 56
5.1. PPIA and its activity site mutant bind with different affinities to PR repeat polymers 56
5.2. PPIA modulates PR20/RNA condensate 58
5.3. PPIA enhances the isomerization of prolines in PR20 60
5.4. PPIA and its activity site mutant have weak affinities towards Tau 63
5.5. PPIA modulates the droplets of Tau 66
6. Discussion: Part 2 69
6.1. PPIA modulates the condensate of proline rich IDPs 69
6.2. Isomerization of prolines in Tau by PPIA must be crucial for its dissolution 69
6.3. Outlook 70
7. References 71
8. Appendix 89
8.1. Protein and plasmid sequences 89
8.2. Supplementary Figures 91
8.3. X-Ray data 95
8.4. Resonance Assignments 97

List of figures

Figure 1: Deposits of misfolded proteins in neurodegenerative diseases. 2
Figure 2: Schematic representation of IDP misfolding in neurodegeneration. 3
Figure 3: C9orf72 mutation in ALS/FTD. 5
Figure 4: Toxicity of dipeptide repeat polymers. 6
Figure 5: Simple schematic of biomolecular condensation through LLPS. 8
Figure 6: Simple schematic showing the aggregation of proteins from their condensate. 10
Figure 7: Cis and trans conformations in peptide bonds. 12
Figure 8: Cis/trans isomerization of proline by prolyl isomerases. 13
Figure 9: Splitting of nuclear energy levels in the presence of the external magnetic field. 25
Figure 10: Three stages of a 1D NMR experiment and its classical visualization. 26
Figure 11: Total Correlation Spectroscopy. 27
Figure 12: Nuclear Overhauser Effect Spectroscopy. 28
Figure 13: Simplified scheme of ROESY pulse sequence. 29
Figure 14: Simplified schematic representation of an HSQC pulse sequence. 29
Figure 15: Simple schematic showing perturbations in a protein peak upon ligand binding. 30
Figure 16: C9orf72-associated PR repeat polymers inhibit prolyl isomerase folding activity. 44
Figure 17: PR repeat polymers bind to the catalytic site of PPIA. 45
Figure 18: AP and GP repeat polymers bind weakly to PPIA. 47
Figure 19: Strength of binding of PPIA to PR repeat polymers depends on the repeat length. 49
Figure 20: Structural basis of chaperone inhibition by PR repeats. 50
Figure 21: Inhibition and sequestration of prolyl isomerases by C9orf72-ALS/FTD-associated PR repeat polymers. 54
Figure 22: PR20 binds to wild-type and mutant PPIA with different affinities. 57
Figure 23: PPIA interferes with RNA-induced LLPS of PR20. 59
Figure 24: Fluorescence recovery of TMR-labelled PR20 inside PR20/tRNA droplets. 60
Figure 25: Isomerase activity of PPIA on the dipeptide repeat protein PR20 in the dilute state in the absence of RNA. 62
Figure 26: Binding of Tau to wild-type and mutant PPIA. 64
Figure 27: Tau binds weakly to wild-type and mutant PPIA. 65
Figure 28: PPIA modulates tau LLPS. 67
Figure 29: Fluorescence recovery of Alexa488-labelled Tau inside Tau droplets. 68
Supplementary Figure 1: SDS gels of purified proteins. 91
Supplementary Figure 2: Individual refolding curves of RNaseT1. 92
Supplementary Figure 3: Comparison of the structure of the active site of PPIA bound to PR20 and other Xaa-proline dipeptides. 93
Supplementary Figure 4: Time dependent observation of PR20/tRNA droplets 94

List of tables

Table 1: Chemicals with the seller's name 16
Table 2: Equipment with seller's name. 18
Table 3: Preparation of 1 L minimal media 20
Table 4: Peptides used in the study 22
Table 5: Conditions of measurement of rate of cis/trans proline isomerization in PR20. 35
Supplementary Table 1: X-ray data collection statistics. 95
Supplementary Table 2: X-ray structure refinement statistics of the PR20/PPIA-complex. 96
Supplementary Table 3: Resonance Assignments of Wild Type PPIA 97
Supplementary Table 4: Resonance Assignments of mutant PPIA(R55A) 101

Abbreviations

ALS	Amyotrophic Lateral Sclerosis
AP	Alanine/Proline
C9orf72	Chromosome 9 Open Reading Frame 72
DPR	Dipeptide Repeat
FKBP	FK506 Binding Protein
FRAP	Fluorescence recovery after photobleaching
FTD	Frontotemporal Dementia
FUS	Fused in sarcoma
GA	Glycine/Alanine
GP	Glycine/Proline
GR	Glycine/Arginine
hnRNPA1	Heterogeneous Nuclear Ribonucleoprotein A1
HSQC	Heteronuclear Single Quantum Coherence
IDP	Intrinsically Disordered Protein
IDR	Intrinsically Disordered Region
INEPT	Insensitive Nuclei Enhanced by Polarization Transfer
ITC	Isothermal Calorimetry
LCR	Low Complexity Region
LLPS	Liquid–liquid phase separation
NMR	Nuclear Magnetic Resonance
NOE	Nuclear Overhauser Effect
NOESY	Nuclear Overhauser Effect Spectroscopy
PPIA	Peptidyl-prolyl isomerase A
PPIases	Peptidyl-prolyl isomerases
PR	Proline/Arginine
RNA	Ribonucleic acid
RNAase A	Ribonuclease A
RNase T1	Ribonuclease T_1
RNAsin	Ribonuclease inhibitor
ROESY	Rotating Frame Overhauser Enhancement Spectroscopy
SOD1	Superoxide Dismutase

TDP43	Transactive response DNA binding protein of 43 kDa
TIA1	Tia1 cytotoxic granule-associated RNA- binding protein
TOCSY	Total Correlation Spectroscopy
tRNA	Transfer RNA

1. Introduction

1.1. Neurodegenerative diseases

Neurodegenerative diseases are caused by the deterioration of nerve cells. The main symptoms of neurodegeneration include memory loss, compromised cognitive abilities, behavioral changes, disturbed mental health, and poor muscle control[1-5]. Alzheimer's disease, Parkinson's disease, Amyotrophic Lateral Sclerosis (ALS), and Huntington's disease are a few examples of commonly occurring neurodegenerative diseases[1-3,6]. Each of them affects distinct brain regions and exhibits different clinical and pathological features[7,8].

With increasing age, the likelihood of developing neurodegenerative diseases rises remarkably[9,10]. Modern medicine has significantly enhanced the life expectancy of people[11]. With an increased life span, the occurrence rate of neurodegenerative diseases has spiked in recent years[12]. Considering the devastating impact these diseases have on the quality of life, unraveling its molecular basis and finding treatment is of utmost priority.

1.2. Protein misfolding and disrupted homeostasis in neurodegeneration

1.2.1. General aspects of protein misfolding in neurodegeneration

The deposition of misfolded protein aggregates is a key characteristic of every neurodegenerative disease. For instance, misfolded deposits of Tau and amyloid-β proteins are observed in the brain regions affected by Alzheimer's disease (Fig. 1a,b)[13,14]. Inclusions of misfolded proteins called Lewis bodies, primarily composed of the protein α-synuclein, is a key feature of Parkinson's disease (Fig. 1c)[15]. In ALS, misfolded deposits of proteins like TDP43, FUS, SOD1 etc. are found in the affected motor neurons (Fig. 1d,e)[16-19]. Aggregates of misfolded glutamine-expanded Huntingtin protein is observed in the brain of Huntington's disease patients (Fig. 1f)[20]. In healthy conditions, cells utilize the protein quality control machinery to recycle or degrade the misfolded proteins accumulated during various cellular processes[21-23]. However, such machinery is insufficient in neurodegenerative diseases, especially because of the age-associated decline in its function and the high load of aggregates formed[24].

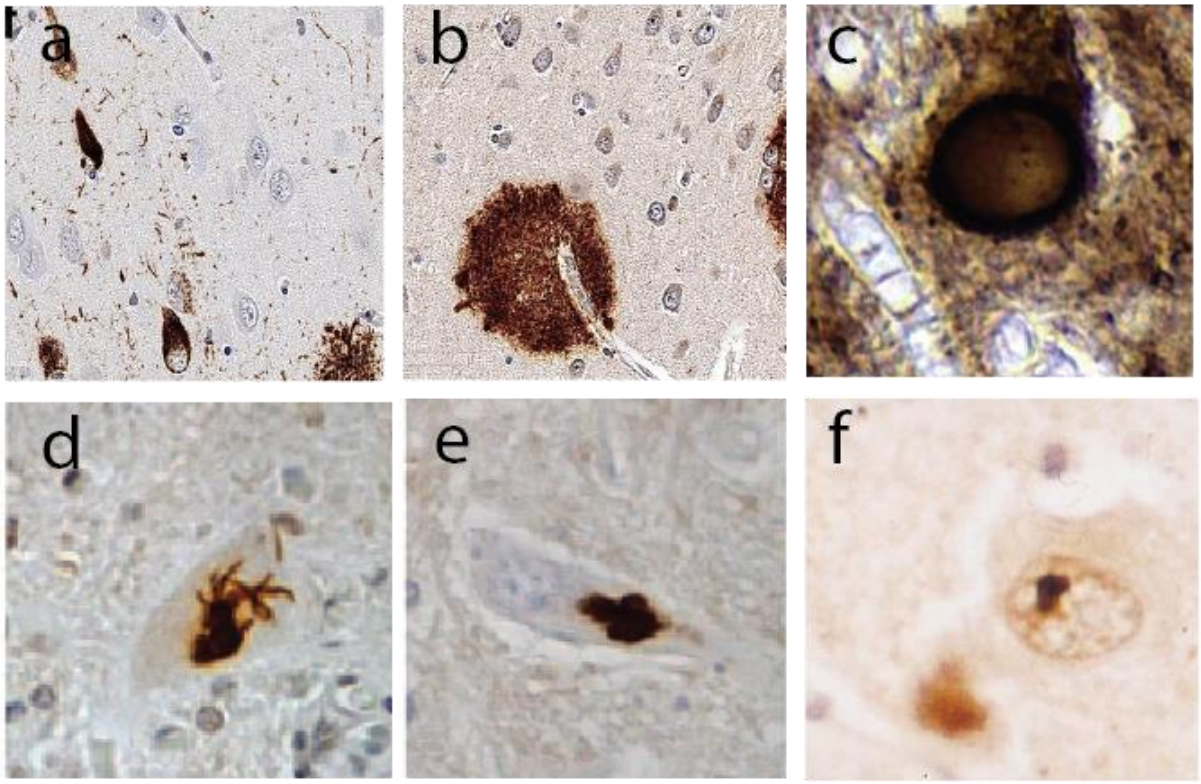

Figure 1: Deposits of misfolded proteins in neurodegenerative diseases.
(a) Tau and **(b)** Amyloid-β aggregates in Alzheimer's disease (taken from reference[25]). **(c)** α-synuclein aggregates in Parkinson's disease (taken from reference[26]). **(d)** TDP43 and **(e)** FUS deposits in ALS (taken form reference[27]). **(f)** Huntingtin protein deposits in Huntington's disease (taken from reference[28]).

Causes of protein misfolding in neurodegeneration: A number of factors can cause protein misfolding that results in neurodegeneration. Protein misfolding can arise due to mutations in its sequence[29-36]. Mutations cause aberrant interactions, that reduce the stability of a protein's functional conformation and cause its misfolding[37]. In addition, aberrant chemical modifications of proteins, such as phosphorylation, acetylation, etc. can lead to its destabilization and misfolding[38-41]. As an example, hyperphosphorylation of Tau protein destabilizes its binding to microtubules and causes its toxic aggregation in Alzheimer's disease[42-44]. Prolonged physiological stress and age-associated or mutation-induced loss of the protein quality control machinery are other factors that can lead to pathogenic misfolding of proteins[24,45].

Protein intrinsic disorder and neurodegeneration-associated misfolding: Many proteins that mediate neurotoxic misfolding are intrinsically disordered or have intrinsically disordered regions interspaced between folded domains[46-50]. Intrinsically disordered proteins (IDPs) or intrinsically disordered regions (IDRs) lack a stable structure and are flexible to exist as a

conformational ensemble[51]. Examples of neurodegeneration-associated IDPs include Tau and α-synuclein[46,47], while IDR-rich proteins include TDP43 and FUS[48-50]. Cellular functions of IDPs and IDR-rich proteins originate from their structural flexibility which allows them to interact with several binding partners as per the cellular necessities[52]. However, the downside of disordered conformation is that the exposed amino acids make them prone to abnormal interactions in response to undesirable deviations such as mutations[29-31,34-36]. Abnormal interactions that modulate the disordered conformation of IDPs or IDR-rich proteins promote their neurotoxic misfolding, resulting in aggregate formation[53]. In addition to their own misfolding, the promiscuous interactive nature of IDP or IDR-containing proteins pave way for the co-aggregation of their interacting partners with them[54,55].

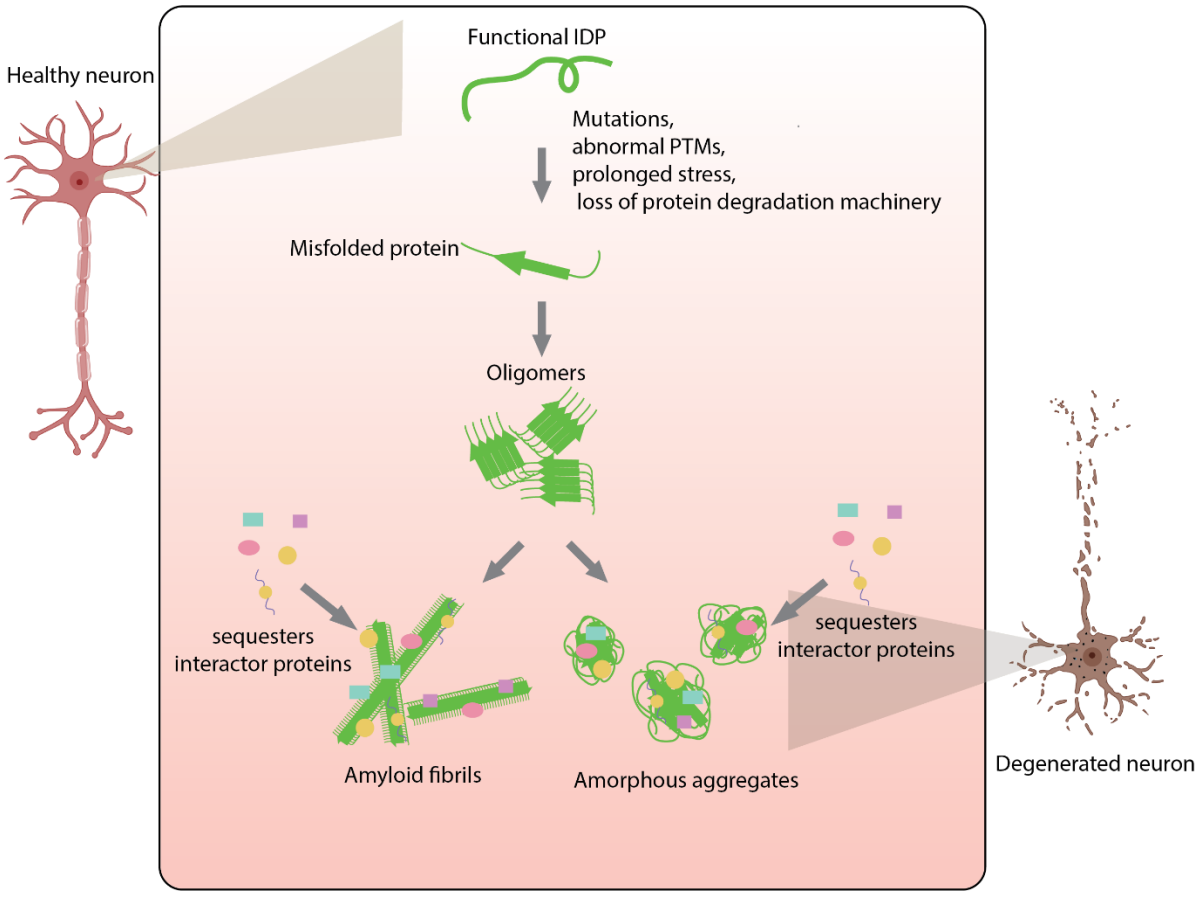

Figure 2: Schematic representation of IDP misfolding in neurodegeneration.
Variations from normal physiological conditions modulate the IDP conformation and cause IDP aggregation. Misfolded proteins associate through intermolecular interactions to form oligomers, which further interact with each other to form ordered amyloid fibrils or amorphous aggregates. These aggregates can recruit their interactor proteins in the neuron and cause their co-aggregation.

Types of protein aggregates and their toxicity: Aggregates that are formed by the misfolded proteins can be of different morphologies. A commonly observed feature regarding

neurodegeneration-associated protein aggregates is their amyloid-like fibrillar morphology[56-60]. Amyloid fibrils contain stacked beta strands that are aligned perpendicular to the fibril axis[61-63]. Their formation is generally driven by the exposure of hydrophobic surfaces in the misfolded proteins to the aqueous surrounding[64,65]. The misfolded intermediates interact among themselves to form soluble oligomers, which then assemble into highly ordered amyloid fibrils (Fig. 2)[56,61]. Some of the neurodegeneration-associated proteins that forms amyloid fibrils include Tau, amyloid beta, and α-synuclein[57-59]. However, aggregates found in neurodegenerative diseases are not always in amyloid fibrillar form; they can also be observed as amorphous aggregates of misfolded proteins that lacks an ordered structure (Fig. 2)[56,66,67]. The toxicity of misfolded and aggregated proteins arises due to various factors, including their mislocalization[68-70], loss of function[71,72], and gain of toxic functions such as recruitment of numerous essential cellular proteins and RNA into the aggregates causing their loss, etc (Fig. 2)[55,73-76]. These factors distrupt the neuronal homeostasis - the steady maintenance of the functional state of neurons - which results in neurodegeneration[7,77].

In this thesis, we are interested in two distinct cases of protein misfolding and disrupted homeostasis in neurodegeneration: protein misfolding in C9orf72-ALS/FTD and that from biomolecular condensates. An introduction to these two cases are given in the following sections.

1.2.2. Disrupted homeostasis in C9orf72-ALS/FTD

1.2.2.1. C9orf72 associated ALS and FTD

Amyotrophic Lateral Sclerosis (ALS) and Frontotemporal Dementia (FTD) are two neurodegenerative diseases that share common clinical, genetic and pathological features[6,78,79]. As a result, ALS and FTD are considered to be part of a single disease spectrum[6,78,79]. There are several protein mutations that cause ALS and/or FTD, including mutations in FUS, TDP43, SOD1, C9orf72, Tau, etc[80]. Among them, C9orf72 (Chromosome 9 open reding frame 72) gene mutation is the most common cause of familial ALS and FTD[81,82]. C9orf72 gene codes for C9orf72 protein, which is involved in autophagy regulation[83,84]. In the non-coding region of the C9orf72 gene, there is a GGGGCC (G4C2) hexanucleotide sequence which may be repeated up to an average of 23 times in a healthy individual[81,82]. In C9orf72-ALS/FTD patients, this region undergoes an expansion mutation resulting in hundreds to thousands of the G4C2 sequence repetitions (Fig. 3)[81,82].

The toxicity of the C9orf72 hexanucleotide expansion is attributed to two mechanisms. I) reduced production of C9orf72 protein leading to its loss of function[85-88] II) the gain of toxicity by the products of the mutation, i.e., repeat RNA and dipeptide repeat polymers[89-93]. Bidirectional transcription of the expanded repeat region produces G4C2 and G2C4 repeat RNA sequences that forms secondary structures (Fig. 3)[89,90]. Repeat Associated Non-AUG translation (RAN) of the two RNAs, in all three reading frames, produces dipeptide repeat polymers (DPRs) that lack a stable structure [91-93]. Five different types of dipeptide repeat polymers are formed in this way: repeats of Proline/Arginine (PR repeat polymers), Glycine/Arginine (GR repeat polymers), Glycine/Proline (GP repeat polymers), Glycine/Alanine (GA repeat polymers) and Alanine/Proline (AP repeat polymers) (Fig. 3)[91-93]. RNA and dipeptide repeat polymer toxicity is associated with their aberrant interactions with numerous other functional proteins, causing their co-aggregation[94-98]. Based on animal studies, the toxicity of dipeptide repeat polymerss, especially PR and GR repeat polymers, is a major cause of toxicity in C9orf72 mutation carriers[89,99-101].

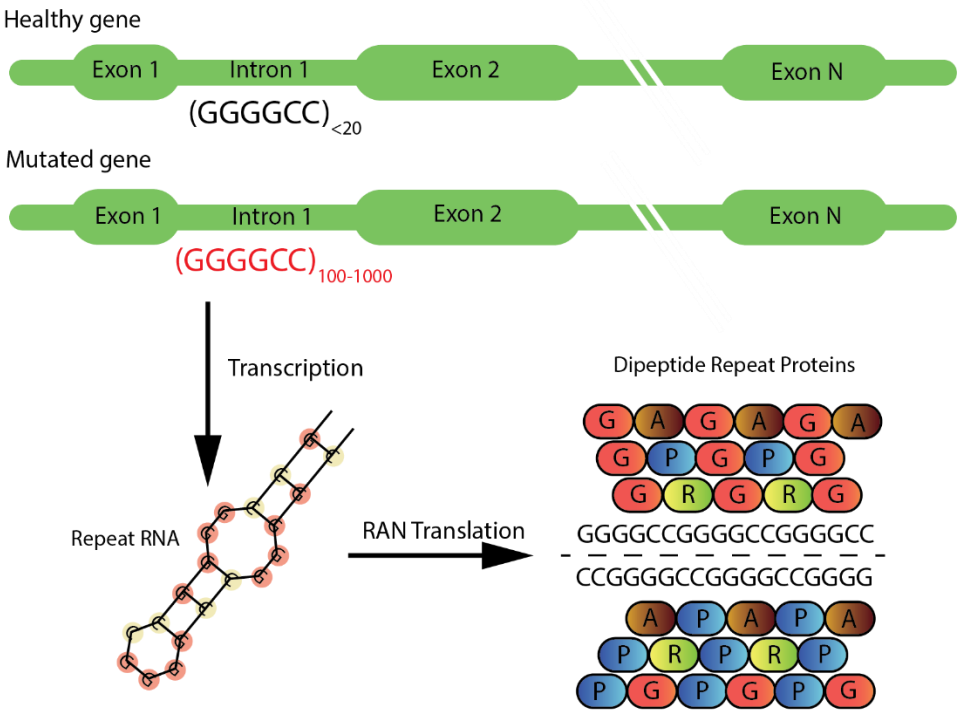

Figure 3: C9orf72 mutation in ALS/FTD.
The C9orf72 gene with repeat expansion mutation can have 100s to 1000s of G4C2 repeats in contrast to an average of 23 repetitions in a healthy individual. Transcription of the expanded region produces repeat RNA that forms secondary structures. RAN translation of sense and antisense strands of repeat RNA results in five different dipeptide repeat polymers.

1.2.2.2. Dipeptide repeat polymer mediated disruption of homeostasis in C9orf72-ALS/FTD

Protein misfolding and disrupted homeostasis, as in any other neurodegenerative disease, is a characteristic feature of C9orf72-ALS/FTD. Here, disrupted homeostasis is caused by the aberrant interactions of dipeptide repeat polymers with other biomolecules such as RNA and proteins[97,98,102]. Among the five dipeptide repeat polymers, GA repeat polymers has the highest tendency to form amyloid fibrillar aggregates because of its hydrophobic nature[103,104]. GA repeat polymer toxicity is linked to the recruitment of functional proteins, especially those associated with cellular trafficking and the proteasomal machinery (Fig. 4a)[99,103]. Even though GA repeat polymer is most prone to aggregation, the highest toxicity in model systems is possessed by the highly soluble GR and PR repeat polymers that are abundant in arginines[89,97,99,105].

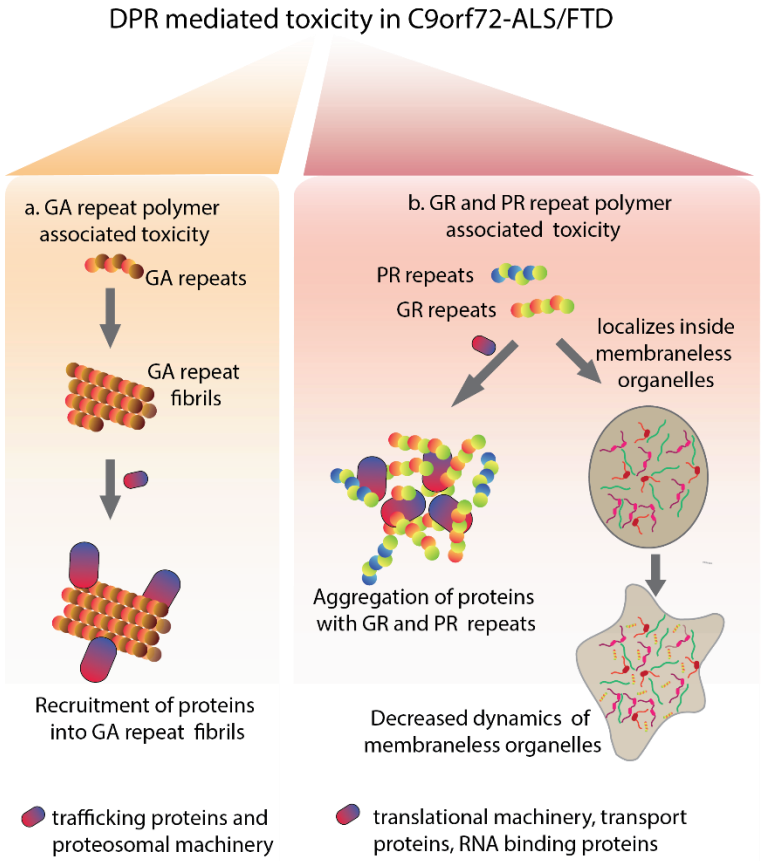

Figure 4: Toxicity of dipeptide repeat polymers.
(a) GA repeat polymers form amyloid fibrils, which sequester trafficking proteins and the proteosomal machinery. **(b)** PR and GR repeat polymers aberrantly interact with the translational machinery, nucleocytoplasmic transport proteins and LCD containing proteins, thus causing their mislocalization, aggregation and loss of function. They get recruited into membranelles organelles and perturb the functional dynamics.

GR and PR repeat toxicity has been associated with their aberrant interactions, in their soluble disordered form, with numerous other functional proteins[97,98]. Agreeing with their promiscuous nature, proteomic studies identified 196 proteins that interact with GR and PR repeat polymers, with 41% overlap[97]. To provide a comparison with other dipeptide repeat polymers, GA repeat polymers interact with only 14 proteins, while GP and AP repeat polymers did not have any significant interactors[97]. GR and PR repeat polymers, because of their solubility, do not form amyloid fibrils, but disrupt homeostasis by co-aggregating with other functional proteins (Fig. 4b)[54,97,98,106]. For example, GR and PR repeat polymers induce the mislocalization and co-aggregation of translational and nucleocytoplasmic proteins through direct interactions with them[97,106-113]. GR and PR repeat polymers are also strong interactors of RNA and RNA-binding proteins that are crucial in the formation of membraneless organelles[97,98,102]. This interaction facilitates the recruitment of PR and GR repeat polymers into membraneless organelles, which adversely affects their dynamics and cause protein co-aggregation with the repeats[54,97,105,114,115]. It is to be noted that most of these studies treat GR and PR repeat toxicity as a single entity, which is attributed to exposed and interactive arginine side chains. The contribution of the non-arginine amino acids to the toxicity of these repeat polymers is yet to be understood.

1.2.3. Biomolecular condensates- protein misfolding interface in neurodegenerative diseases

1.2.3.1. Biomolecular condensation

Biomolecular condensation occurs by the process of liquid-liquid phase separation (LLPS) of biomolecules such as proteins and nucleic acids[116-118]. In LLPS, a uniform solution of solute molecules in a solvent demixes into two distinct phases with liquid-like properties: one that is concentrated with solute molecules and the other without them (Fig. 5)[116]. LLPS occurs when the interaction of a solute with solvent molecules is energetically less favorable than the exclusive interactions between themselves.[116,119] LLPS can be of two types: simple coacervation and complex coacervation (Fig. 5)[120,121]. In simple coacervation, a single kind of solute molecules self-assemble whereas, in complex coacervation, solute molecules of different

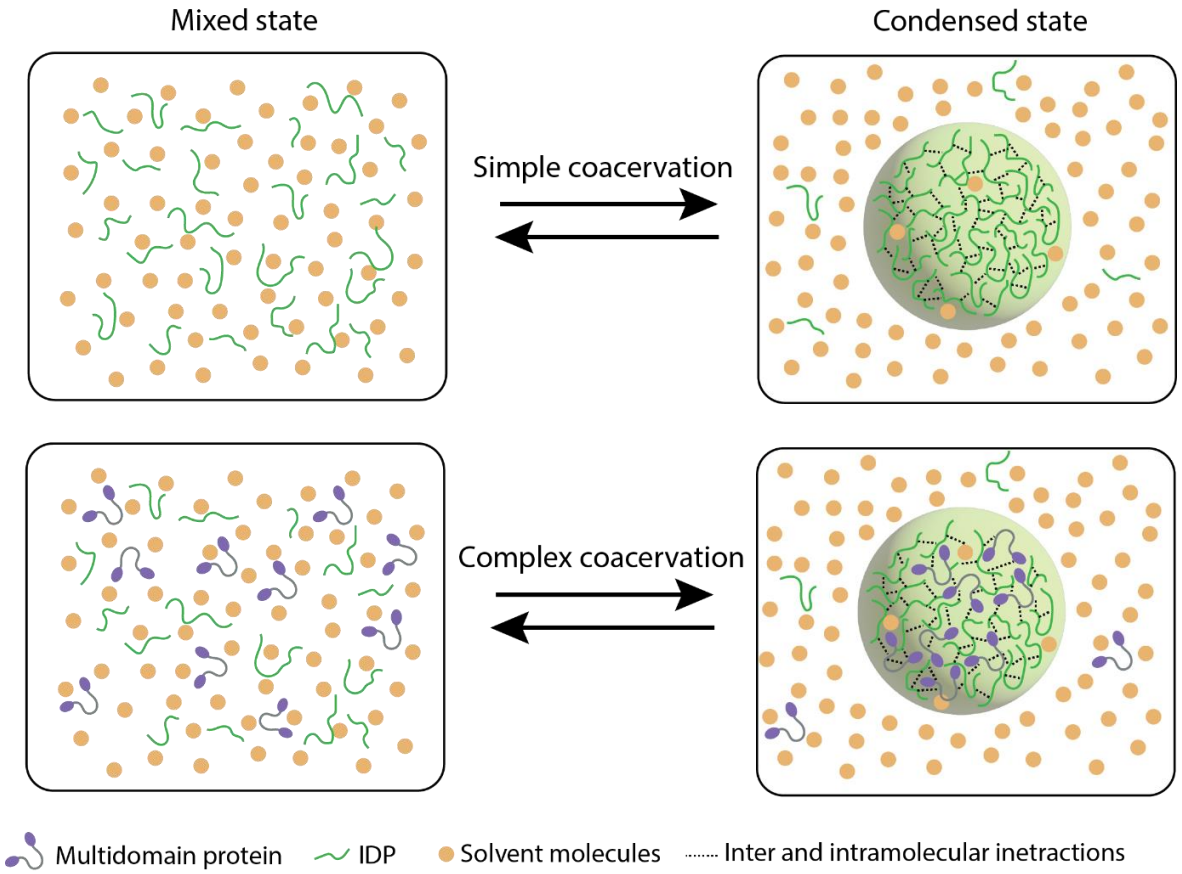

Figure 5: Simple schematic of biomolecular condensation through LLPS.
Biomolecules(solute) and the solvent molecules are uniformly distributed in the mixed state. In the condensed state, biomolecules associate through multivalent interactions. In simple coacervation, a single type of biomolecule demixes from the uniform phase. In complex coacervation, two(or more) different types of biomolecules associate through intermolecular contacts.

kinds interact with each other and assemble together[120,121]. Several factors can trigger LLPS of biomolecules including changes in physiological conditions such as pH, temperature, salt concentration, increase in the concentration of phase separating components, or post-translational modifications[122-124]. Unlike solid aggregates or fibrils of proteins, biomolecular condensates are dynamic and reversible[125]. Furthermore, some solvent molecules are preserved inside the solute phase, giving it liquid-like properties[125].

Biomolecular condensates are formed by the association of biomolecules through a network of multivalent interactions[117]. IDPs or IDR-containing proteins are the key players in biomolecular condensation[126-129]. The exposed amino acids in intrinsically disordered sequences facilitate multivalent interactions via pi-pi, cation-pi, charge-charge and hydrophobic forces[102,126,130,131]. For some IDPs or IDR-containing proteins, LLPS is specifically driven by their low complexity regions (LCRs), which are sequences that carry

repeats of a very few different amino acids[126,128]. Most often, LCRs consist of neutral and polar residues that possess high propensity to self-associate into liquid-like condesates[132-134]. In addition to the multivalent interactions of intrinsically disordered sequences, protein-protein interactions through folded domains and protein-RNA interactions can also contribute to biomolecular condensation[135-137].

Cells utilize the phenomenon of LLPS to form membranelles organelles such as nucleoli, cajal bodies, p-body, stress granules etc[138,139]. These organelles exhibit liquid-like properties: they have a spherical shape, fuse with each other, and are in dynamic equilibrium with the surrounding, etc[138,140] As LLPS selectively concentrates biomolecules from the bulk, it is capable of creating an environment that is favorable for specific biomolecular reactions[141]. In cases of cellular stress, LLPS can provide a mechanism for the protection of RNA and proteins from misfolding, by temporarily condensing them into liquid granules[142,143]. The sensitivity of LLPS to surrounding conditions enables biomolecular condensates to form and dissociate spontaneously according to cellular necessities.

1.2.3.2. Protein misfolding from biomolecular condensate and its regulation

As biomolecules phase separate, their concentration increases multiple fold when compared to the mixed state[144]. Increased concentration of biomolecules enhances the risk of aberrant interactions and misfolding inside the condensate, leading to the formation of solid aggregates (Fig. 6). Protein misfolding within condensate gets accelerated by physiological abnormalities such as protein mutations or prolonged stress[125]. Even with minor changes from normality, LLPS can go awry because of its sensitivity to its environment. Often, such variations are correlated with aging-associated diseases[125].

Several IDPs or IDR containing proteins, that are known to misfold in neurodegeneration, are participants of biomolecular condensation[128,145-149]. As a result, biomolecular condensates are considered to be hotspots for neurodegenerative protein aggregation. For instance, misfolding in ALS and FTD is associated with aberrant transitions from stress granules - the organelles that are temporarily formed by the LLPS of RNA and IDR-rich RNA-binding proteins during cellular stress [150,151]. Stress granules shield proteins and RNA from damage caused by stress and they disassemble into functional biomolecules once the stress is gone.[143] Many RNA-binding proteins like hnRNPA1, FUS, TDP43 and TIA1, that are associated with ALS and FTD, participates in stress granule formation[128,145-148,152,153] . It is thought that stress granules may serve as a platform for these proteins to aggregate in the case of abnormal variations such

as mutations or prolonged stress. In support of this hypothesis, a decrease in dynamics was observed in the condensates of disease-associated mutants of FUS, TDP43, hnRNPA1 and TIA1[128,147,148,154,155]. Another case of protein aggregation from stress

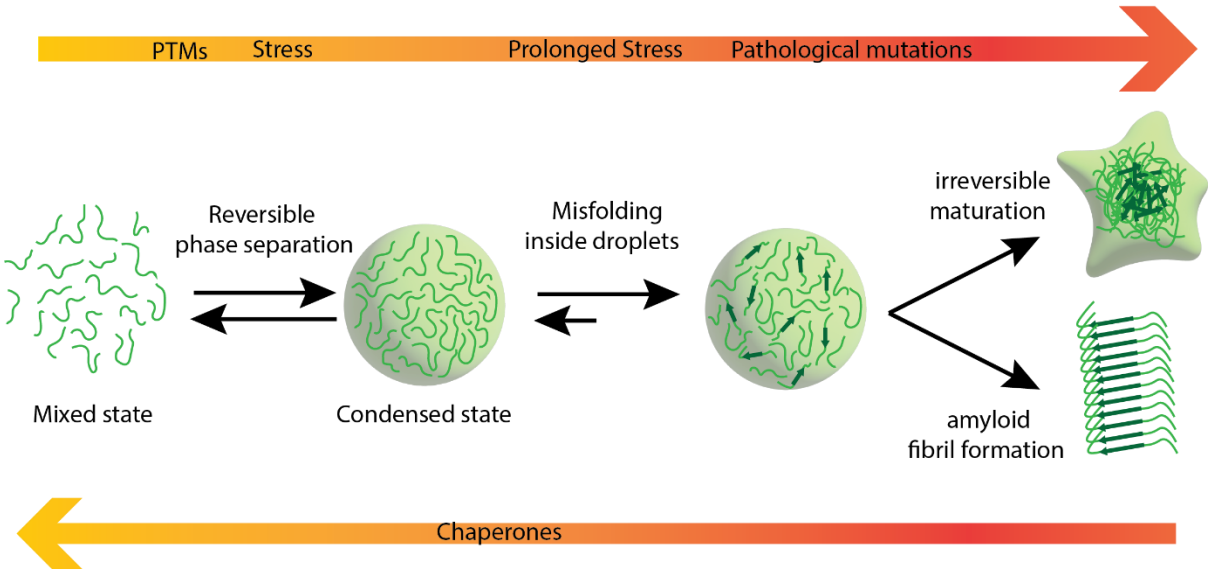

Figure 6: Simple schematic showing the aggregation of proteins from their condensate.
Factors like prolonged stress and pathological mutations can induce misfolding within the condensate. Misfolded proteins reduce the dynamics and reversibility of liquid condensates. Through their aberrant interactions, misfolded proteins cause unfavorable maturation of condensates. In addition, they can associate with each other to form ordered amyloid fibrils. Molecular chaperones decelerate the protein misfolding from condensates by constantly restructuring the misfolded interfaces. (Figure is adapted from reference[156])

granule is associated with C9orf72-ALS/FTD[97]. Here, PR and GR repeat polymers migrated into the stress granules and reduced its dynamics, thus causing their liquid to solid transition[97]. Misfolding of Tau - an Alzheimer disease-related IDP - from its condensate is another example for toxic liquid to solid transition within condenaste[157]. Tau protein is primarily involved in microtubule formation and stabilization in the neurons[158]. Phase separation of Tau plays an important role in its function: it facilitates the nucleation of microtubules[149]. However, disease-associated variations in Tau results in its transition from liquid to solid phase within the condensate[157]. Aggregation of Tau is associated with Alzheimer's disease[159].

The tendency of proteins to misfold inside the condensate calls for tight control over their dynamics. According to recent studies, molecular chaperones play an important role in modulating biomolecular condensates and thus maintaining their dynamics. For instance, heat shock proteins such as Hsp70, Hsp27 and Hsp40 could migrate into the condensate of ALS/FTD associated IDR-containing RNA-binding proteins, and prevent their aggregation[160-

[162]. Nucleocytoplasmic transport proteins had inhibitory effect on the LLPS of RNA-binding proteins[163-165]. Protein disulphide isomerases migrated into the droplets of Alzheimer related Tau protein and modulated the LLPS of Tau[166]. In general terms, these chaperones prevent aberrant interactions by dynamically interacting with the proteins and constantly remodeling the misfolding interface[161,165,167-169].

1.3. Peptidyl prolyl isomerases and protein homeostasis

1.3.1. Peptidyl prolyl isomerase: mode of action

Peptidyl-prolyl isomerases (also known as prolyl isomerases or PPIases) are proteins whose physiological function is based on their unique action on the proline residues in their substrates[170-172]. To perceive the broad biological relevance of prolyl isomerases, one must first understand the peculiar features of proline cis/trans isomerization in a peptide bond.

Proline cis/trans isomerization: Compared to other amino acids, prolines have a ring structure due to their carbon side chain from C_α attached to the nitrogen group. (Fig. 7b). Because of the unique ring structure, proline residues in peptide bonds (known as prolyl peptide bonds) can exist in trans and cis conformations, as opposed to other amino acids, which exist primarily in trans conformation[173,174]. In non-prolyl peptide bonds, the cis conformation is subject to more steric hindrance than the trans conformation (Fig. 7a). Hence, the cis conformer possesses higher energy than the trans conformer, making it less favorable [173,175,176]. However, in prolyl peptide bonds, cis and trans conformers exhibit similar steric hindrances (Fig. 7b), narrowing their energy differences and making them both favorable[173,175,177,178]. Despite the comparable energies of the two conformers in prolyl peptide bonds, their interconversion demands a high activation energy (approximately 20 kcal/mol)[179]. A high barrier to interconversion results from the partial double bond character of peptide bond and restricted rotation about it (Fig. 7)[179]. Consequently, the interconversion rates between the two isoforms are slow, taking up to minutes[179,180].

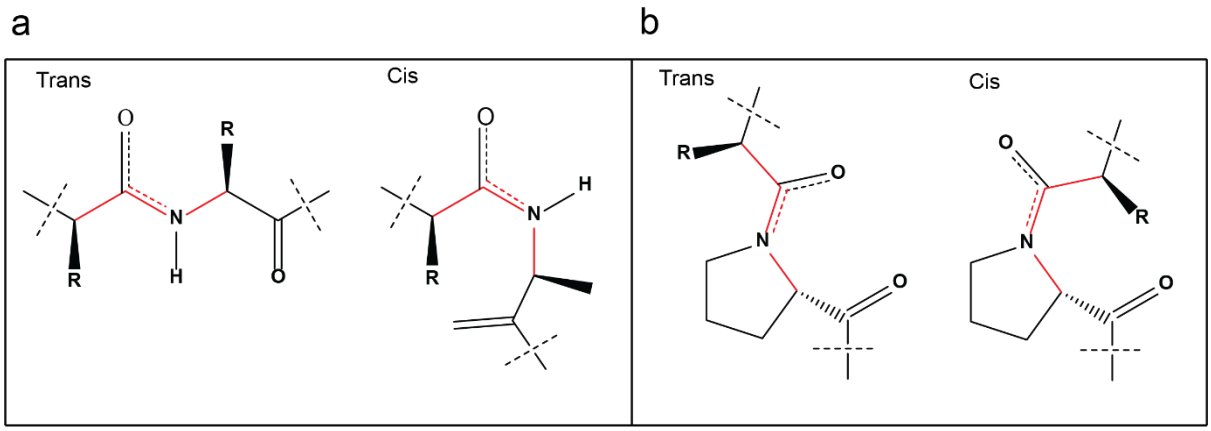

Figure 7: Cis and trans conformations in peptide bonds.
Bonds marked in red colour highlight the conformation of peptide bonds. a) Trans and cis conformations in a non-prolyl peptide bond. Cis conformation experiences higher steric hindrance than the trans conformation. b) Trans and cis conformation in a prolyl peptide bond. Because of the distinct ring structure in prolines, cis and trans conformation experience comparable steric hindrance.

Prolyl Isomerases are catalysts of proline isomerization: Prolyl isomerases are enzymes that accelerate the cis/trans interconversion rate of prolines in a peptide bond[172,181]. They achieve the enhanced cis/trans isomerization of prolyl peptide bonds by decreasing the activation energy of this process (Fig. 8a)[180]. Prolyl isomerases can enhance the rate of isomerization from minutes to milliseconds range[180,182] .

Prolyl isomerases are classified into three families based on structural similarities: cyclophilins, FK506 Binding Proteins (FKBPs), and parvulins[181]. The name cyclophilin and FKBPs come from their binding affinity for the drugs Cyclosporin-A and FK506, respectively[181]. The most extensively investigated prolyl isomerase is the prolyl isomerase A (PPIA), also known as Cyclophilin A - the most abundant of its kind[183]. The crystal structure of PPIA reveals that its binding site consists of an antiparallel barrel made up of β-strands, which is surrounded by three α-helices (Fig. 8b). According to a recent study, the enzymatic pocket of PPIA generates an electrostatic field that act on the dipole moment of carbonyl group prior to the proline residue in the substrate[182]. This force facilitates the flip of the prolyl peptide bond in the substrate[182]. Arg55 in the binding site of PPIA is crucial in creating this electrostatic atmosphere and thus plays a vital role in its isomerase activity[182,184]. For this reason, the mutation of Arg55 to Ala55 reduces the activity of PPIA[182].

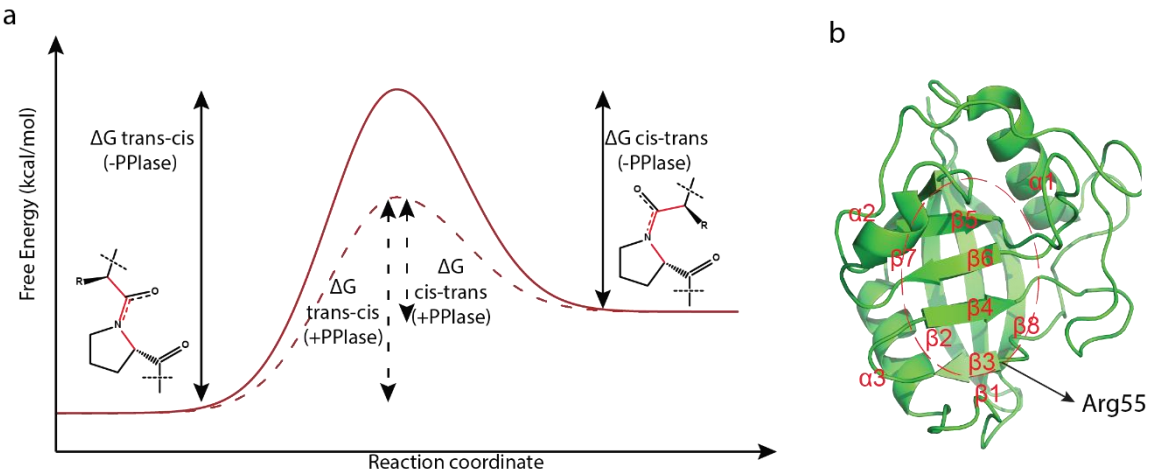

Figure 8: Cis/trans isomerization of proline by prolyl isomerases.
a) Free energy diagram of proline cis/trans isomerization in the absence (continuous red line) and presence (dotted red line) of prolyl isomerase. Prolyl isomerase enhances the cis/trans interconversion rate by decreasing its activation energy.(Figure is adapted from reference[185]) b) Structure of PPIA-the most abundant of all prolyl isomerases (PDB code: 5KUZ, *https://www.wwpdb.org/pdb?id=pdb_00005kuz*[186]). The catalytic activity site of PPIA is marked with a dotted circle. The eight β strands, three α helices and the location of Arg55 are also indicated.

1.3.3. Peptidyl prolyl isomerase in protein folding and misfolding

Prolyl isomerases, because of its isomerase activity, play an important role in de novo protein folding of globular proteins[179]. As a nascent amino acid chain folds into its native structure, prolyl peptide bonds must take on a specific conformation that is relevant for its functional structure[172]. This is in contrast to their unfolded state where prolines are free to assume cis or trans conformations[172]. The slow cis/trans isomerization of the prolyl peptide bond limits the rate at which prolines adopt their definite conformation, limiting the protein folding rate[172,187]. Prolyl isomerases enhances the rate of isomerization, thus enhancing the rate of folding of structured proteins[172,179,187]. The longer the process of folding, the longer the protein chain is exposed to the crowded cellular milieu, increasing the chances of aberrant intermolecular interactions[188,189]. Prolyl isomerases reduce the exposure time for aberrant interactions, thus contributing to the maintenance of cellular homeostasis. The ability of PPIA to catalyze protein folding has been demonstrated on several proteins including RNase A, and RNase T1[172,187].

IDPs or IDR-containing proteins are abundant in proline residues, making them substrates of prolyl isomerases[174,190]. In fact, the proline abundance in intrinsically disordered sequences is approximately 1.5 times more than that in structured proteins[174]. However, our knowledge of the biological significance of the interaction of prolyl isomerases with IDPs or IDR-containing

proteins is limited. Recent studies suggest that the activity of prolyl isomerases toward intrinsically disordered sequences impacts its misfolding. They demonstrated that prolyl isomerases can alter the pathogenic aggregation of proline-rich IDPs such as Tau and alpha-synuclein, through a combination of binding and isomerase activity on proline residues[191-195]. For example, Cyclophilin 40 dissolved the preformed Tau fibrils at stoichiometric Tau: Cyclophilin 40 concentration[191]. The binding of Cyclophilin 40 to the proline-rich region of Tau in amyloid fibril is considered responsible for the dissolution of Tau fibrils. Consistent with that, overexpression of Cyclophilin 40 reduced Tau deposits in Alzheimer's disease mouse models[191]. Likewise, Cyclophilin D, by acting on the proline residues of α-synuclein in the C-terminal domain, blocked α-synuclein aggregation and caused the disintegration of their fibrils [193]. In another study, enhancement of cis/trans proline isomerization by PPIA in the proline-rich C-terminal of α-synuclein increased its rate of aggregation[192]. FKBP12 also enhanced the aggregation of α-synuclein fibrils through its isomerase activity[194]. These studies suggest a broader biological significance of prolyl isomerases in pathogenic IDP misfolding that is based on its action on proline residues.

1.4. Aims of the work

Prolyl isomerases have different functional roles towards globular proteins and IDPs. While prolyl isomerases assist in the de novo folding of the structured protein, they are involved in the regulation of misfolding of IDPs or IDR-containing proteins. Thus, they play a significant role in maintaining cellular homeostasis. Although an initial understanding of the role of prolyl isomerases in neurodegeneration-associated protein misfolding is available, the broader significance of prolyl isomerases in multiple pathways of neurodegenerative protein misfolding is lacking. In this thesis, we investigated the involvement of PPIA - the most abundant kind of prolyl isomerases, in two different neurodegeneration-associated protein misfolding pathways: protein misfolding in C9orf72-ALS/FTD and that from biomolecular condensates.

In C9orf72-ALS/FTD, the toxicity mainly arises from the aberrant interactions of PR and GR repeat polymers with proteins and RNA that eventually disrupts cellular homeostasis. Because of the abundance of prolines in PR repeat polymers, we predicted the interaction of PPIA with PR repeat polymers. Supporting our hypothesis, a proteomic study by Lee et al. identified prolyl isomerases as specific interactors of PR repeat polymers in vivo[97]. Here, we explored the consequences of the interaction of PPIA with PR repeat polymers on its protein folding activity, which is essential for maintaining cellular homeostasis. Using NMR spectroscopy and

X-ray crystallography, we aimed to gain insight into the structural basis of PPIA/PR repeat polymer interaction and the significance of the proline-arginine composition in its binding.

The second part of this thesis presents our studies to understand the regulatory role of PPIA on biomolecular condensates - the hotspot of protein misfolding. A number of chaperones proteins are implicated in the regulation of biomolecular condensate dynamics. Despite the abundance of prolines in the intrinsically disordered sequences that drive LLPS, the impact of prolyl isomerases on the LLPS was unknown. Emphasizing the potential role of PPIA in regulating biomolecular condensation, a recent study reported that a significant fraction of PPIA interactome are proline-rich proteins involved in LLPS[190]. In our study, we focused on exploring the regulatory role of PPIA on LLPS by utilizing two different in vitro condensates of IDPs: the complex coacervate of PR repeat polymers with RNA[102,196] and the self-assembled condensate of Tau protein[131]. These condensates were chosen for their significance in neurodegenerative diseases and their abundance of proline residues. We investigated the modulatory effect of PPIA on these condensates. We also sought to understand the mechanism behind the effect induced by PPIA on these condensates.

2. Materials and Methods

This section contains excerpts directly taken from the following publications. They are indicated in italic font.

Babu, Maria, et al. Nature communications 12.1, 3396 (2021); DOI: https://doi.org/10.1038/s41467-021-23691-y

Babu, Maria, et al. Journal of the American Chemical Society 144.35, 16157-16163 (2022) ; DOI: https://doi.org/10.1021/jacs.2c07149

2.1 Materials

2.1.1. Chemicals

Table 1: Chemicals with the seller's name

Chemical	*Seller*
^{15}N labelled ammonium chloride ($^{15}NH_4Cl$)	Cambridge Isotope Laboratories
4-(2-hydroxyethyl)-1-piperazineethanesulfonic acid (HEPES)	Sigma-Aldrich
Alexa 488 micro labelling labelling Kit	Thermo Fischer
Ampicillin sodium salt	Sigma-Aldrich
Bactotrypton	Bacto Difco
BCA Kit	Sigma-Aldrich
BenchMark™ protein ladder	Thermo Fisher
Biotin	Sigma -Aldrich
Boric acid (H_3BO_3)	Thermo Fischer
Cobalt(II) chloride hexahydrate ($CoCl_2 \cdot 6H_2O$)	Sigma-Aldrich
cOmplete™ Protease Inhibitor Cocktail EDTA-free Tablets	Sigma-Aldrich
Copper(II) chloride dihydrate ($CuCl_2 \cdot 2H_2O$)	Sigma-Aldrich
Deuterium Oxide (D_2O)	Sigma-Aldrich
Sodium phosphate dibasic(Na_2HPO_4)	Carl Roth
Dithiothreitol (DTT)	Sigma-Aldrich
Ethylene glycol-bis(β-aminoethyl ether)-N,N,N′,N′-tetraacetic acid (EGTA)	Sigma-Aldrich

Ethylenediaminetetraacetic acid (EDTA)	Sigma-Aldrich
Glucose	CIL
Imidazole	Sigma-Aldrich
Isopropyl β-D-1-thiogalactopyranoside (IPTG)	Carl Roth
Iron(III) chloride hexahydrate ($FeCl_3 \cdot 6H_2O$)	Merck
Kanamycin sulphate	Sigma-Aldrich
Lysozyme	Sigma-Aldrich
Magnesium sulphate ($MgSO_4$)	Sigma-Aldrich
Ni-NTA Agarose	Qiagen
Phenylmethyl sulfonyl fluoride (PMSF)	Carl Roth
Piperazine-N,N′-bis(2-ethanesulfonic acid) (PIPES)	Sigma-Aldrich
Potassium phosphate dibasic (K_2HPO_4)	Sigma-Aldrich
Potassium phosphate monobasic (KH_2PO_4)	Sigma-Aldrich
RNase T1	Thermo Fischer
RNAsin	Promega
Sodium chloride (NaCl)	Sigma-Aldrich
Sodium phosphate monobasic monohydrate ($NaH_2PO_4.H_2O$)	Merck
Streptomycin sulphate	Sigma-Aldrich
Syto 17 RNA dye	Thermo Fischer
TEV	Received from our lab technician C.S. Maria Omori
Thiamine hydrochloride	Sigma-Aldrich
TMR labelled PR20	GeneScript
Tris HCl	Thermo Fischer
Tris(2-carboxyethyl)phosphine hydrochloride (TCEP)	Sigma Aldrich
Urea	Serva
Yeast extract	Sigma-Aldrich
Yeast tRNA	Thermo Fischer
Zinc chloride ($ZnCl_2$)	Honeywell Fluka

2.1.2. Equipment

Table 2: Equipment with seller's name.

Equipment	*Seller*
45 Ti fixed angle rotor	Beckman Coulter
5810R benchtop centrifuge	Eppendorf
Agarose gel electrophoresis chambers	Bio-Rad Laboratories
ÄKTAprime plus	GE Healthcare
Analytical balance	Sartorious
Avanti JXN26	Beckman Coulter
Cary Eclipse Fluorecence Spectrometer	Agilent
Gel Doc™ XR+	Bio-Rad Laboratories
Heratherm™ compact incubator	Thermo Scientific
JA 25.50 fixed angle rotor	Beckman Coulter
JLA 8.1000 fixed angle rotor	Beckman Coulter
KS 4000 i control incubation shaker	IKA
Leica DM6B	Leica Microsystems
Leica TCS SP8	Leica Microsystems
MicroCal PEAQ-ITC	Malvern Panalytical
MonoS S10/ 100 GS	GE Healthcare
Multitron Pro incubation shaker	INFORS HT
NanoDrop™ 2000/2000c spectrophotometer	Thermo Scientific
NMR spectrometers	Bruker
Optima XPN80 ultracentrifuge	Beckman Coulter
pH meter	Mettler Toledo
Sonopuls	Bandelin
Superdex 75 16/600	GE Healthcare
Superdex 75 26/600	GE Healthcare
ThermoMixer comfort	Eppendorf
Zeiss LSM 880	Zeiss Microscopy

2.1.3. Software

Adobe Illustrator Artwork, CCPN2.4.2, Endnote, Expasy Protparam, Graphpad Prism, ImageJ, MicroCal PEAQ-ITC, Microsoft Office 365, Pymol, Topspin 3.6.2

2.2. Protein and peptide synthesis

2.2.1. Expression and purification of PPIA

Wildtype human PPIA and its mutant PPIA(R55A), cloned into the pET28a vector were received from our previous group member Dr. Filippo Favretto. BL21(DE3) competent cells were bought from Novagen.

The PPIA (or PPIA(R55A)) plasmid was transformed in Escherichia coli BL21(DE3) cells. For unlabelled protein, cells were cultured in LB medium with kanamycin (30 mg/ml) at 37 °C. When the OD (at 600 nm) value reached 0.6, protein overexpression was induced with 0.4 mM IPTG. After 15 h of incubation at 16 °C, cells were centrifuged down at 7000 rpm using JLA-8.1.000 rotor. *The cell pellet from 1-liter culture was then resuspended in 40 ml of resuspension buffer (20 mM sodium phosphate, 300 mM NaCl, 2 mm DTT, 5 mM imidazole, 0.01% NaN3, pH 7.2) additionally supplemented with 100 mM PMSF, 100 mg/ml lysozyme* and *at pH 7.2. The cells in this buffer were sonicated in* ice cold conditions, *centrifuged* at 22000 rpm at 4º C using a JA 25.50 rotor, *and the supernatant was loaded onto a Ni-NTA Agarose column. The column was washed with resuspension buffer containing 10 and 25 mM imidazole; protein was eluted with the resuspension buffer supplemented with 300 mM imidazole. The His-tag was cleaved by incubating the protein with TEV protease in a dialysis bag (MWKO 3.5 kD) at room temperature overnight while dialysing it to His-tag cleavage buffer (20 mM sodium phosphate, 150 mM NaCl, 2 mM DTT, 0.1 mM EDTA at pH 7.7). Next, the protein solution was again loaded onto the 5 ml Ni-NTA Agarose column. The His-tag-cleaved PPIA* (or PPIA(R55A)) *came out in the flow through. It was concentrated using a concentrator of pore size 5 kDa ,loaded onto a gel filtration column (Superdex 75 16/600, GE Healthcare Life Sciences) and eluted with 50 mM HEPES, 150 mM NaCl, 3 mM DTT, 0.02% NaN3, pH 7.4.* The purity of PPIA (or PPIA(R55A*)* was checked on an SDS gel (SI Fig. 1a,b). For long term use, purified PPIA (or PPI(R55A) was aliquoted and stored at -80º C. *They were thawed and dialyzed (membrane size:3.5 kD) into the respective buffers for the experiments described in the later sections*. Protein concentrations were determined by measuring absorption at 280 nm on a nanodrop.

^{15}N-labeled PPIA (or PPIA(R55A)) was produced by culturing and inducing the cells in M9 minimal media supplemented with $^{15}NH_4Cl$. The protocol for minimal media preparation is shown in Table 3. The remaining steps in the production of labeled PPIA (or PPIA(R55A)) is similar to the one described for unlabeled protein.

Table 3: Preparation of 1 L minimal media

Component	*Amount*
10X M9 salts	100 ml
Glucose	4 g
1000X Trace elements	1 ml
1 M $MgSO_4$	1 ml
1 mg/ml biotin	1 ml
10 mg/ml Thiamin	0.1 ml
1 M CaCl2	300 ul
$^{15}NH_4Cl$	0.5 g
1000X antibiotic	1 ml

10X M9 recipe for 1 L: 30 g KH_2PO_4, 68 g Na_2HPO_4, 5 g NaCl

Adjust pH to 7.4 at room temperature.

1000X Trace elements recipe for 1 L: 50 g EDTA, 8.33 g $FeCl_3.6H_2O$, 840 mg of $ZnCl_2$, 100 mg $CoCl_2$.6H2O, 130 mg of $CuCl_2$. $2H_2O$, 100 mg H_3BO_3

Adjust pH to 7.5 after dissolving EDTA in100 ml of water and later add the rest of the components to avoid precipitation.

2.2.2. Expression and purification of Tau

Tau protein was produced by C.S Maria Omori in the Zweckstetter lab. The purification protocol of Tau is given below.

The plasmid of full length human Tau cloned into pNG2 vector was received from Mandelkow lab at DZNE, Bonn. Tau plasmid was transformed into Escherichia coli BL21(DE3) cells. To produce unlabeled protein, transformed cells were grown at 37 °C in an LB medium. As the OD (at 600 nm) reached 0.8, protein expression was induced by adding 0.5 mM IPTG. Cells were incubated at 37º after the induction for 3 hours and then pelleted down using JLA-8.1.000

rotor at 7000 rpm. The cell pellet was resuspended in 20 mM MES buffer, pH 6.8 which additionally contained 2 mM DTT, 1 mM EGTA, 200 µM $MgCl_2$, 1 mM PMSF, 0.01 mg/ml DNaseI, 1 mg/ml lysozyme, and cOmplete™ EDTA-free Protease Inhibitor Cocktail. Bacterial cells were then broken using a French press. 500 mM of NaCl was added to the lysed cells and was heated up to 98º for 20 minutes. This step caused the precipitation of contaminant proteins. htau40, because of its intrinsically disordered nature, retained its functional conformation in the solution. Precipitated contaminants were separated by employing ultracentrifugation (45Ti rotor) at 127000 g at a temperature of 4º for 40 minutes. The supernatant, which contains Tau protein, was collected and streptomycin was added to this solution at a concentration of 20 mg/ml to induce nucleic acid precipitation. After incubating this sample at 4º for 10 minutes with mild shaking, it was centrifuged at 15000 g for 30 minutes at 4º C using FA-45-6-30 rotor. In the next step, 0.361 g/ml of ammonium sulphate ($(NH_4)_2SO_4$) was added to the supernatant from the previous step in order to pellet down the Tau protein. After 10 minutes of incubation at 4º, the solution was centrifuged at 15000g at 4º for 30 minutes using FA-45-6-30 rotor. Tau pellet was then dissolved in 20 mM MES at pH 6.8, 50 mM NaCl, 2 mM DTT, 1mM EDTA and 0.1 M PMSF (buffer A) and then dialyzed overnight into the same buffer with a 3.5 kDa membrane so as to remove ammonium sulphate. Protein solution was then subjected to ion exchange chromatography (Mono S 10/100 GL, GE Healthcare), where it was eluted with 20 mM MES at pH 6.8 containing 2 mM DTT, 1 mM EDTA and 1 M NaCl(buffer B) at a gradient of 60 percent in combination with buffer A. It was then concentrated using a concentrator of 5kDa pore size and loaded to a gel filtration (Superdex 75 26/600, GE Healthcare) column. It was washed down with PBS buffer containing 500 mM NaCl, 1 mM DTT, and 0.1 mM PMSF. Purity of the protein was further confirmed with an SDS gel (SI Fig. 1c). Purified Tau was concentrated using a 5 kD concentrator and dialyzed to 25 mM HEPES at pH 7.4, 1mM TCEP.

In order to produce labelled Tau, Escherichia Coli BL21 DE3 cells transformed with Tau plasmid was first grown in LB till the OD of the culture reached 0.8. It was then centrifuged down at 5000 g for 30 minutes at 4º C using a JLA-8.1.000 rotor. Then pelleted cells were resuspended in 1X M9 salts and centrifuged again under the previous condition. It was then transferred to M9 media (Table 3), grown for 1 hours at 37º C and then induced with 0.5 mM IPTG. The procedure after IPTG induction is similar to that described for unlabeled Tau.

2.2.3. Synthesis of dipeptide repeat polymers

Peptides were produced by K. Overkamp, technician at the NMR2 department of MPINAT, Göttingen. Peptides used in this study are listed below.

Table 4: Peptides used in the study

Peptide	*Sequence*
AP20	APAPAPAPAPAPAPAPAPAPAPAPAPAPAPAPAPAP
GP20	GPGPGPGPGPGPGPGPGPGPGPGPGPGPGPGPGPGP
GR20	GRGRGRGRGRGRGRGRGRGRGRGRGRGRGRGRGRGR
PR2	PRPR
PR5	PRPRPRPRPR
PR10	PRPRPRPRPRPRPRPRPRPR
PR20	PRPRPRPRPRPRPRPRPRPRPRPRPRPRPRPRPRPR

PR20, GR20, GP20, AP20, PR10, PR5, and PR2 peptides were synthesized by solid-phase peptide synthesis. All peptides were acetylated and amidated at the N- and C-termini, respectively. Peptide stocks were prepared by weighing and dissolving the required amount of powder in the buffers as per the experimental requirements.

2.3. RNase T1 protein refolding assay

2.3.1. Principle

RNase T1 is a globular protein with two each prolyl peptide bonds in its native structure. The slow cis/trans isomerization of prolyl bonds limits the folding rates of RNase T1. PPIA is known to enhance its folding kinetics by increasing the prolyl bond interconversion rate[187,197].

The folding process of RNase T1 can be studied by following its intrinsic tryptophan fluorescence[187,197]. Tryptophan residue in folded RNase T1 is buried inside its hydrophobic core. As the protein folds, tryptophan goes from a polar to a non-polar environment. This change in its chemical atmosphere results in progressively increasing fluorescence intensity. The completion of the folding process is marked by the saturation of fluorescence intensity.

2.3.2. Experimental condition

RNaseT1 was unfolded by incubating in 6.9 M urea at 10 °C for 2 h in 100 mM Tris-HCl buffer at pH 8. Refolding of RNaseT1 was initiated by diluting it 35 times with the same buffer such that the final concentration of RNaseT1 was 2.27 µM and urea 0.197 M. Tryptophan fluorescence emission was measured at 320 nm (excitation wavelength = 280 nm) during refolding for 1 h on a Cary Eclipse Fluorescence Spectrophotometer at 10 °C. RNase T1 refolding experiments were then conducted in the presence of PPIA alone or PPIA along with PR20 repeat polymer. A control experiment was also performed where RNAseT1 was folded in the presence of PR20 alone. *In experiments with PPIA, PR20 or both, they were added to the dilution buffer and incubated at 10 °C for 2 h prior to mixing. Data were normalized and averaged for graphical representation. The exponential constants, k, for the increasing fluorescence intensities were obtained from fitting a mono-exponential function to the experimental data in Graph Pad Prism*

2.4. X- Ray crystallography

X-Ray crystallography is a useful technique to get insights into the atomic structure of biomolecules. When X-rays are irradiated on a protein crystal, they are diffracted into specific patterns. The pattern of diffraction can be used to obtain atomic-level information about the protein's structure.

X-Ray crystallographic studies of the PPIA-PR20 complex were performed by Dr. Stefan Becker at MPI-NAT, Gottingen. The protocol for the same is described below.

For crystallization, the PR20 peptide was added in fivefold molar excess to PPIA. The total protein concentration was adjusted in 25 mM HEPES, 2 mM DTT, 0.01 % NaN_3 at pH 7.4 to 20 mg/ml. Crystals were obtained at 20 °C by sitting drop vapor diffusion using 0.1 M HEPES, pH 7.5, 25% PEG1000 as reservoir solution. For data collection, crystals were cryoprotected in reservoir solution supplemented with 10% glycerol. Data collection was performed at 100 K at SLS Villigen, Switzerland (beamline PXII, Eiger2 16M detector, Dectris). Data were processed with XDS[198]. Space group determination and statistical analysis were performed with XPREP (Bruker AXS, Madison, Wisconsin, USA). The structure was solved by molecular replacement with PHASER[199] using the crystal structure of PPIA (PDB code: 5KUL[186]) as search model. Refinement was performed with Refmac[200] alternating with manual model building in Coot[201].

2.5. NMR spectroscopy

2.5.1. Introduction to NMR

2.5.1.1. Energy splitting

Nuclear magnetic resonance spectroscopy (NMR) is widely utilized to characterize the properties of biomolecules, such as their structure, dynamics, etc. It exploits the local magnetic fields associated with the atomic nucleus, which is caused by the spin property of protons and neutrons[202,203]. A nucleus with even numbers of both protons and neutrons has zero spins, whereas those with at least one of these species in an odd number have a non-zero spin. In order to have a magnetic moment, a nucleus must have a non-zero spin value. The magnetic moment associated with a nucleus is given by the equation[204],

$$\mu=\gamma I$$

where γ is the gyromagnetic ratio, a nuclei-specific constant value that is the ratio of the magnetic moment and angular momentum, and I is the spin quantum number. The common nuclei observed by NMR include ^{1}H, ^{13}C ,^{15}N and ^{31}P.

Every nucleus with a magnetic moment act as a tiny bar magnet. Unless an external magnetic field is applied, each magnetic moment in an ensemble of nuclei is randomly oriented, resulting in net zero magnetization (Fig 9). When the sample is placed in an external magnetic field, as in an NMR spectrometer, the magnetic moments associated with the nuclei orient along or against the external field, creating lower and higher energy states respectively (Fig 9)[205]. The splitting of energy in the presence of a magnetic field can also be explained in terms of spin quantum number. The external field forces energy levels to split to 2I+1 values, where I is the spin quantum number[204,205]. For example, ^{1}H nuclei, with an I value of ½ splits into two levels. The gap between the energy levels is dependent on the strength of the applied magnetic field. The probability of finding nuclei in the ground state is more than in the higher energy states, resulting in a higher population at the ground level[204]. When a radio frequency pulse is applied, a fraction of spins gets transferred from the ground state to the excited state. As the excited nuclei return to their ground state, energy is released, which is detected in NMR[205].

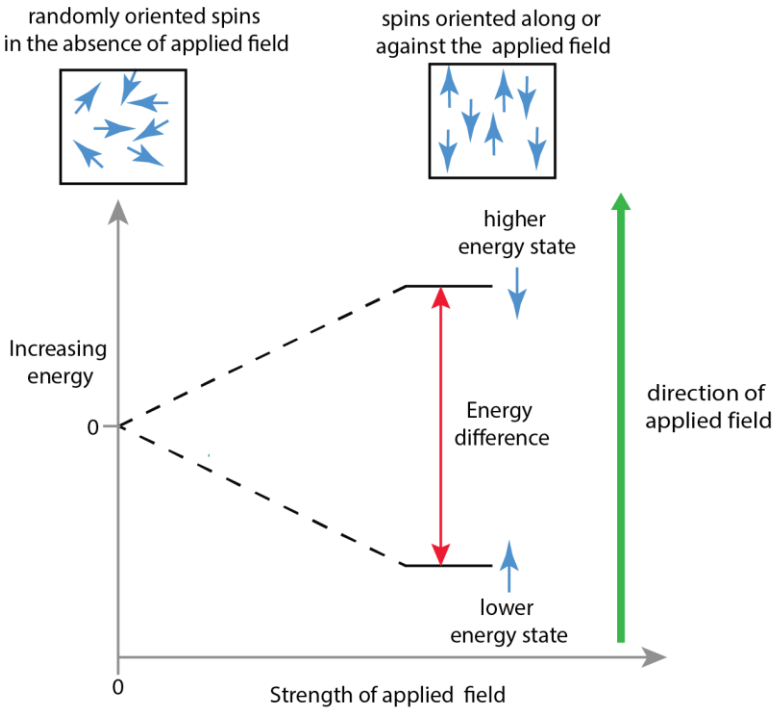

Figure 9: Splitting of nuclear energy levels in the presence of the external magnetic field.
Spins are randomly oriented in absence of magnetic field. In the presence of an external field, they align parallel to the magnetic field. The difference between the energy levels is directly associated with the strength of external magnetic field.

2.5.1.2. Chemical shift

The motion of negatively charged electrons creates a magnetic field around the nucleus, which is aligned in the opposite direction of the applied magnetic field in an NMR spectrometer. As a result, the field experienced by the nucleus is reduced from the applied field by a value that is proportional to the electron cloud density around it. Each kind of nuclei with a distinct electronic atmosphere will experience different effective fields, resulting in different energy gaps between the ground and excited state[202]. Therefore, different frequencies must be used to excite them (within the radiofrequency range), creating a distinct NMR peak for each kind of nuclei.

2.5.1.3. 1D NMR

A one-dimensional (1D) NMR observes a single type of nuclei. ^{1}H is the most commonly observed nuclei. A 1D NMR experiment is generally composed of three stages (Fig 10)[205]. First is the preparation period, when the magnetic moment associated with nuclei comes to an equilibrium with the external magnetic field (Fig. 10a). It is followed by an excitation period where an RF pulse is applied to excite the nuclei. According to classical mechanics, excitation can be defined as the tipping of net magnetization away from the direction of the external field

(commonly taken as z-axis). Usually, 90º pulses are used for excitation, which brings the net magnetization from the z-axis to the x-y plane (Fig. 10b). In the final detection period, the excited nuclei will return to the ground state, i.e., the net magnetization will rotate back at its specific frequencies to the z-axis again (Fig. 10c). The nuclei relax during this period through spin-spin and spin-lattice interactions. Spin-spin relaxation causes a decrease in the magnetic moment in the x-y plane, whereas spin-lattice relaxation causes its build-up along the z-axis. The precession frequency of the nuclei, which is translated into NMR signals, is detected during this period.

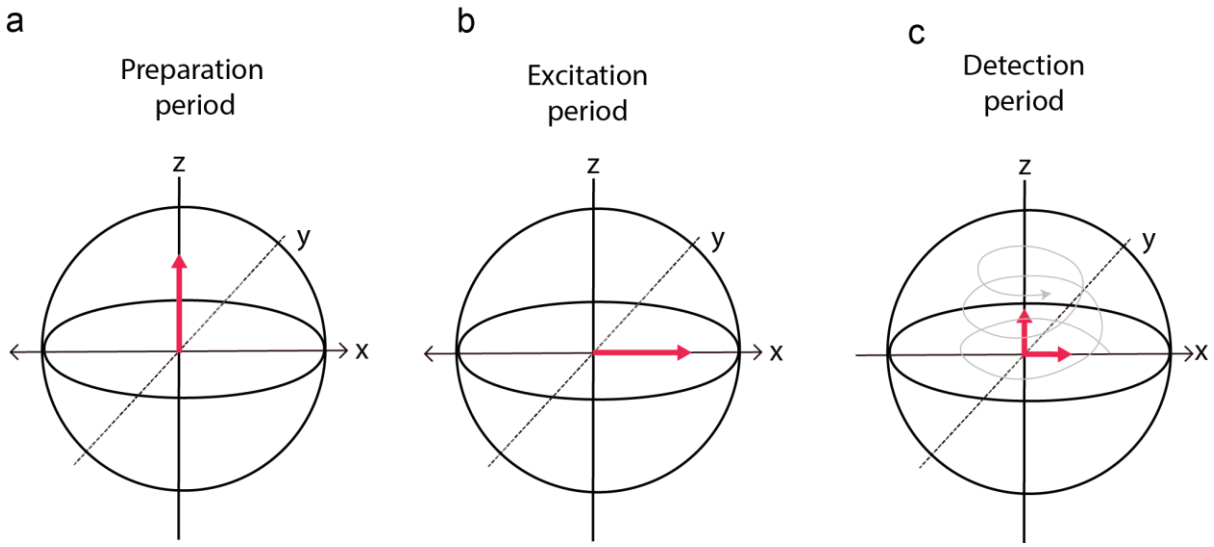

Figure 10: Three stages of a 1D NMR experiment and its classical visualization.
The pink arrows represent the direction of the net magnetization in the three panels. The external magnetic field is applied along z-axis. **(a)** Preparation period when the net magnetization gets aligned along the external magnetic field, i.e., the z-axis. **(b)** Excitation period where the magnetization is tipped off from the z-axis to the x-axis upon application of a 90º pulse along y-axis. **(c)** Detection period when the magnetization precesses and returns back to the z-axis.

2.5.1.4. 2D NMR

1D NMR cannot provide complex information about a molecule. This is especially true in case of large biomolecules, for which considerable overlap of peaks is observed in a 1D spectrum. In addition, it does not establish correlations between different nuclei, that are coupled. In such cases, it is beneficial to disperse the NMR peaks in a second dimension.

Similar to a 1D NMR, a 2D NMR experiment consists of a preparation period followed by an excitation period. The evolution period thereafter labels the nucleus with its corresponding chemical shift as they precess. It is followed by a mixing period where magnetization transfer occurs from the excited nuclei to those coupled with them, via through-bond or through-space

interactions[205]. In the next stage, data points are collected, which contain information about the coupled chemical shifts. The different 2D NMR experiments use different combinations of pulses and delays in order to extract specific information about a molecule. Some of these experiments, relevant to this thesis, are discussed below.

^{1}H-^{1}H TOCSY: Total Correlation Spectroscopy, or TOCSY is extensively used to identify protons that belong to the same spin system[204]. It has ^{1}H frequencies on both dimensions. All the protons in the observed molecule give a diagonal peak in the TOCSY spectrum. However, cross peaks are obtained only between those protons that belong to the same spin system. TOCSY allows the observation of an entire spin system, which extends over 5-6 bonds, by employing a long spin lock pulse (Fig. 11a). During the spin lock pulse, through-bond magnetization transfer takes place successively over the whole spin system (Fig. 11b)[205].

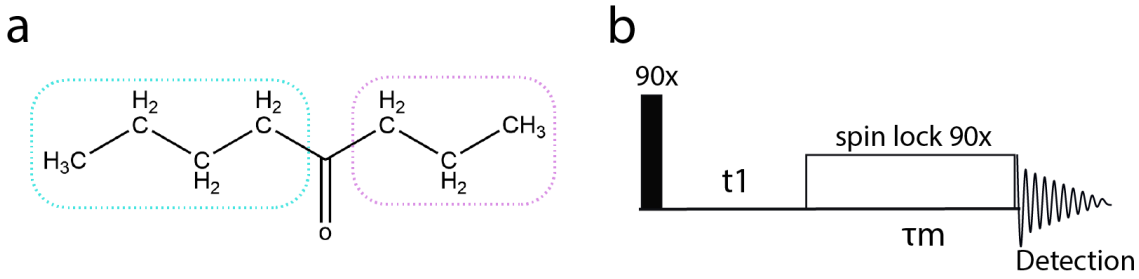

Figure 11: Total Correlation Spectroscopy.
(a) The two spin systems in a given molecule are shown within blue and pink boxes. In a the TOCSY spectrum, cross peaks can be observed between every proton belonging to the same spin system. **(b)** Simplified scheme of a TOCSY pulse sequence. A 90^{o} pulse excites protons non-selectively. Chemical shift evolves during the evolution time marked t1. During the mixing time (τ_m), a spin lock pulse that is applied for 80 ms facilitates successive through-bond coupling within the spin system[205]. Both pulses in the sequence is applied along the x-axis.

^{1}H-^{1}H NOESY: Nuclear Overhauser Effect Spectroscopy or ^{1}H-^{1}H NOESY is a useful NMR experiment to identify protons that are close positioned[204,205]. A NOESY spectrum has ^{1}H frequencies on both dimensions. Cross peaks are observed between two atoms if they are nearby in space, despite the number of bonds separating them (Fig. 12a). Such protons are correlated via through-space coupling. The intensity of NOE cross peaks is directly related to $1/r^6$, r being the distance between two atoms[206]. Thus, the NOESY experiments provides distance information, which is useful in the structure determination of molecules.

The NOESY experiment can be also used to characterize exchange processes between two states[207]. Consider a molecule that can exist in two states, say A and B, and has distinct proton chemical shifts in the two states. If the exchange between states A and B takes place within the NOESY mixing time, the chemical shift of state A will be correlated to that of state B, giving rise to a cross peak. The dependence of the intensity of such a cross peak on the mixing time can be utilized to study the exchange rates[207,208].

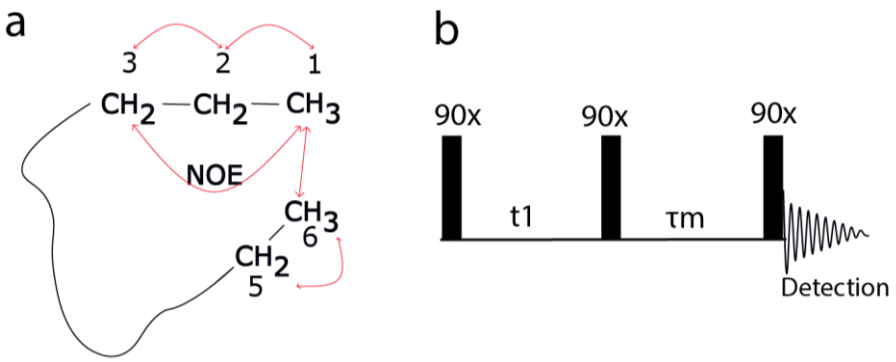

Figure 12: Nuclear Overhauser Effect Spectroscopy.
(a) Correlations observed in a NOESY spectrum depicted on a long chain of a molecule. NOE cross peaks are observed between protons indicated with a double-sided arrow. Although the CH_3 groups marked 6 is located several bonds away from 1, a cross peak is observed between them due to their closeness in space. **(b)** Simplified scheme of a NOESY pulse sequence. After the first 90º pulse and evolution time t1, a second 90º pulse is applied that brings the magnetization to the z-axis. During the mixing time (τ_m), magnetization transfer occurs via through-space coupling[205]. A third 90º pulse is applied then, followed by the detection of signals. Pulses in the NOESY sequence are applied along the x-axis.

^{1}H-^{1}H ROESY: Rotating frame Overhauser Enhancement Spectroscopy or ROESY provides the same information as NOESY. However, the ROESY pulse sequence allows for differentiation between through-space coupling-induced cross peaks and exchange-induced cross peaks[208]. The former has the opposite sign to diagonal peaks, while the latter has the same sign as that of diagonal peaks.

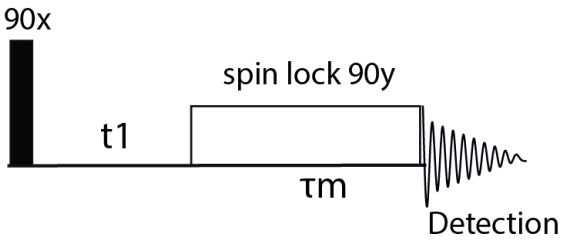

Figure 13: Simplified scheme of ROESY pulse sequence.
A spin lock pulse is applied on the protons after the evolution time (t1). This pulse enables the mixing of magnetization via through-space coupling. However, the pulse length and power should be optimized to get rid of through-bond coupling. The direction of the two pulses is indicated in the figure.

^{1}H-^{15}N HSQC NMR: A ^{1}H-^{15}N HSQC spectrum displays single bond correlations between protons and nitrogen, i.e., it detects N-H entities in the sample[205,209]. It has ^{1}H frequency along the first dimension and ^{15}N frequency along the second dimension. Since ^{15}N is not a naturally abundant isotope, molecules of interest should be labeled with ^{15}N prior to the experiment.

An HSQC pulse sequence initially excites all the protons in the molecule. In the next step, an INEPT element facilitates the transfer of magnetization from ^{1}H to ^{15}N via through-bond coupling. During the evolution time, chemical shift evolves on ^{15}N. Later, magnetization on ^{15}N is transferred to ^{1}H using a reverse INEPT sequence (Fig. 14)[209]. Signals are detected on ^{1}H protons, which already contains the information about the coupled ^{15}N frequencies.

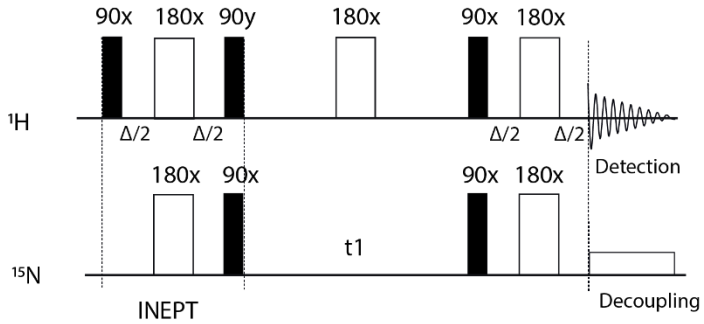

Figure 14: Simplified schematic representation of an HSQC pulse sequence.
Black bars represent 90º pulses whereas white bars represent 180º degree pulses. The initial 90º pulse on ^{1}H excites the protons non-selectively. An INEPT sequence then transfers the magnetization from ^{1}H to ^{15}N[205,209]. To achieve efficient transfer of magnetization, the delay of INEPT must be set in such a way that $\Delta \sim 1/2J(N\text{-}H)$, where J is the strength of N-H bond coupling. While ^{15}N chemical shifts evolve during the evolution time, a 180º pulse is applied on ^{1}H to refocus their chemical shifts. Magnetization is then transferred back to ^{1}H by employing a reverse INEPT sequence. The data points are then collected on ^{1}H. The direction of each pulse is indicated in the figure.

2.5.2. Binding studies using NMR titration

2.5.2.1. Principle of NMR titration

NMR-based titrations are extensively used to characterize biomolecular interactions[210-212]. Consider a protein binding to a ligand to form the protein/ligand complex. In an NMR titration, where protein is observed, a spectrum of protein alone and that of the protein in the presence of increasing concentrations of the ligand are collected. HSQC NMR experiments are often utilized to observe the protein[210]. Upon the formation of the protein/ligand complex, the chemical environment around the protein changes, causing changes in the HSQC spectrum when compared to the reference[210,212]. The spectrum of the protein collected in the presence of the highest concentration of ligand exhibits maximum changes. Mapping the perturbed residues on the structure of the protein facilitates the identification of the binding site[212]. Similarly, ligand-observed titrations can be utilized to identify the region of ligand involved in binding.

The changes observed in an NMR spectrum upon protein/ligand complex formation depend on the strength of the binding. When the lifetime of the complex exceeds the difference in the chemical shift values of the free and complex form of the observed binding partner, the binding is said to be in a slow exchange regime. In such cases, both the free and bound forms of the observed binding partner will appear in the NMR spectrum (Fig. 15)[210]. On the other hand, if

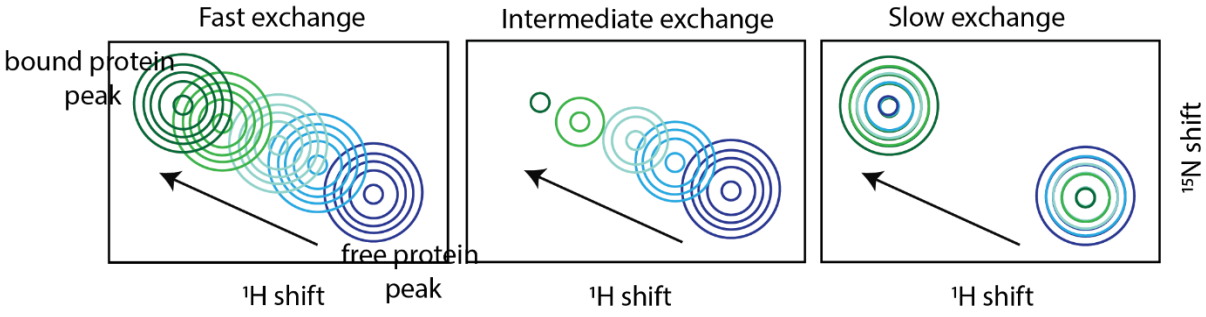

Figure 15: Simple schematic showing perturbations in a protein peak upon ligand binding.
Perturbations observed in the HSQC peak of protein during titration with ligand are shown for fast, intermediate and slow exchange regimes in NMR timescale. Arrows represent the direction in which the peak shifts, as the concentration of ligand is increased. In fast exchange (left), the NMR signal of the free protein (violet) shifts towards the protein/ligand complex peak (dark green) gradually, with increasing ligand concentration. In slow exchange (right), the peak intensity of free protein decreases and that of protein/ligand complex increases, as the concentration of ligand increases. In intermediate exchange regime (middle), characteristics of both slow and fast exchange regime are observed.

the lifetime of the complex is shorter, the binding is said to be in fast exchange. Here, the peaks of the free and bound form of the observed binding partner average into a single peak, based on their populations (Fig. 15)[210]. Most often, strong interactions fall under a slow exchange regime while weak interactions are in fast exchange regimes. Many binding processes are also in intermediate exchange regimes, i.e., shows characteristic of both slow and fast exchange[213]. Here, the intensity of the free protein peak will decrease while it also shifts towards the population-averaged chemical shift of free and bound form (Fig. 15).

The binding affinity of interactions can be quantified from NMR titrations. Protein (P) binding with ligand (L) under equilibrium conditions can be represented by the following chemical equation

$$P_f + L_f \rightleftharpoons PL \qquad 1$$

where P_f is the free protein, L_f is the free ligand, and PL is the protein/ligand complex

P_f and L_f can be expressed in the following ways

$$P_f = P_t - PL \qquad 2$$

$$L_f = L_t - PL \qquad 3$$

where P_t and L_t are the total amounts of protein and ligand respectively.

In a fast exchange regime interaction of the protein with ligand, the chemical shift is the population average of the chemical shift of the bound and free forms of the observed binding partner, which is taken to be the protein for the following calculations[210]. Observed chemical shift δ is given by the equation

$$\delta = \frac{P_f}{P_t} * \delta_f + \frac{PL}{P_t} * \delta_b \qquad 4$$

where δ_f is the chemical shift of the free protein and δ_b is the same for its bound form.

Chemical shift perturbation(CSP) due to complex formation can be represented as follows

$$CSP = \delta - \delta_f \quad (5)$$

Substituting δ from equation 4 to 5 and replacing PL with P_t-P_f from equation 2 gives the following.

$$CSP = (\delta_b - \delta_f) * \left(1 - \frac{P_f}{P_t}\right) \quad (6)$$

From here on, δ_b-δ_f will be referred to as $\Delta\delta_{max}$.

The affinity of this complex formation can be expressed in terms of the dissociation constant K_d that is given by the following equation.

$$K_d = \frac{P_f * L_f}{PL} \quad (7)$$

Substituting equation 2 and 3 to equation 7, and solving for P_f gives the following

$$P_f = \frac{\sqrt{(K_d + L_t + P_t)^2 - 4 * P_t * L_t} - L_t + P_t + K_d}{2} \quad (8)$$

Substituting equation 8 to 6 gives the following equation for CSP

$$CSP = \delta_{max}\left[\frac{(K_d + P_t + L_t) - \sqrt{(K_d + P_t + L_t)^2 - 4 * P_t * L_t)}}{2P_t}\right] \quad (9)$$

In slow exchange regime interactions, K_d value is estimated from the change in intensity. Here, the decrease in intensity of protein peaks upon binding to the ligand is directly correlated to the amount of protein that is engaged in the protein/ligand complex formation. The equation used for K_d estimation is shown below.

$$1 - \frac{I}{I_0} = I_{max}\left[\frac{(K_d + P_t + L_t) - \sqrt{(K_d + P_t + L_t)^2 - 4 * P_t * L_t)}}{2P_t}\right] \quad (10)$$

where I is the intensity of protein peaks in the presence of ligand concentrations, I_0 is the intensity of protein peaks in the absence of ligand, and I_{max} is the maximum intensity of free protein.

2.5.2.2. Titration of PPIA with dipeptide repeat polymers

Titration of ^{15}N-labeled PPIA with dipeptide repeat polymers (PR20, GR20, GP20, AP20, PR10, PR5, and PR2) were carried out in 25 mM HEPES buffer with 100 mM NaCl, 2 mM DTT, 0.01% NaN_3, and 10% D2O at pH 7.4. For 40 μM protein, the ligand concentrations were increased from 0 to 320 μM in five steps. For the PPIA/GP20 and PPIA/AP20 titrations, the concentration of the repeat polymer was further increased up to 3200 μM. Two-dimensional ^{15}N-^{1}H HSQC spectra were acquired at 298 K for each PPIA/repeat polymer ratio. Titration of mutant PPIA(R55A) with PR20 was performed under the same conditions as that of wildtype PPIA/PR20 titration. *The PPIA/GP20 and PPIA/PR2 titrations were performed on a 700 MHz spectrometer (Bruker), whereas all others were performed on a 800 MHz spectrometer (Bruker), both equipped with cryoprobes. The spectra were processed with Topspin 3.6.2 (Bruker) and analyzed with CCPNmr 2.4.2*[214].

K_d calculations for the interactions of PPIA with PR repeats (PR5, PR10, and PR20) were made from the dipeptide repeat polymer-induced variations in PPIA cross-peak intensities, using the equation 10 for slow exchange regime interactions. Here, P_t is the total concentration of PPIA, L_t is the total concentration of ligand, I is the HSQC peak intensity of PPIA in the presence of ligand and I_0 is the HSQC peak intensity of PPIA alone. I_{max} is taken to be a free fit parameter.

The error in $1-(I/I_0)$ is taken to be the error in the experimental quantity of I/I_0 and has been calculated from the noise in HSQC spectra according to

$$\sigma_{(I/I_0)} = \left(\frac{I}{I_0}\right)\sqrt{\left(\frac{\sigma_{(I_0)}}{I_0}\right)^2 + \left(\frac{\sigma_{(I)}}{I}\right)^2} \qquad 11$$

where $\sigma(I/I_o)$ is the error in I/I_0, $\sigma_{(Io)}$ and $\sigma_{(I)}$ are the noise (RMS value of background noise from various regions) in the HSQC spectrum of PPIA alone and that of PPIA in the presence of ligand, respectively. The error value in the K_d is the standard error of fitting.

In case of the PPIA/GP20- and PPIA/AP20 interactions, the K_d value was calculated from the equation 9 for fast exchange interactions using chemical shift perturbations. CSP values are calculated according to the following equation.

$$CSP = \sqrt{(\delta_H)^2 + (\frac{\delta_N}{6.5})^2}. \qquad 12$$

where δ_H and δ_N are the change in chemical shift in the HSQC peaks of PPIA in the presence and absence of ligand in the proton and the nitrogen dimension, respectively. δ_{max} was taken as a free fit parameter. *The error value in the K_d is the standard error of fitting.*

2.5.2.3. Titration of Tau with PPIA

^{15}N-labelled Tau was titrated with wild-type PPIA or mutant PPIA(R55A) in 50 mM sodium phosphate buffer, 1 mM TCEP and 10 % D20 at pH 6.8. Titrations were performed at 278 K on a 800 MHz NMR spectrometer (Bruker) equipped with a cryoprobe. ^{1}H-^{15}N HSQC spectra of 20 Tau µM were recorded in the absence and presence of 200 µM PPIA/PPIA(R55A). The spectra were processed with Topspin 3.6.2 (Bruker) and analysed with CCPN 2.4.2[214].

2.5.2.4. Titration of PPIA with Tau

^{15}N-labelled wild type PPIA was titrated with Tau in 25 mM HEPES buffer, 100 mM NaCl, 1 mM TCEP and 10 % D20 at pH 7.4. . Titrations were performed at 298K on a 800 MHz NMR spectrometer (Bruker) equipped with a cryoprobe. The concentration of the protein was fixed at 18.4 µM. ^{1}H-^{15}N HSQC spectra of the protein were recorded in the absence of Tau and with Tau at 1.95, 4, 7.82, 16.3 and 32 fold excess concentrations with respect to PPIA. Similarly, HSQC spectrum of ^{15}N-labelled mutant PPIA(R55A) was recorded at the PPIA(R55A) concentration of 12 µM, in the absence and in the presence of Tau at PPIA: Tau ratio of 1:4, 1:6, 1:12 and 1:3.8. The spectra were processed with Topspin 3.6.2 (Bruker) and analysed with CCPN 2.4.2[214]*. The K_d value for PPIA-Tau intercation was estimated from the chemical shift perturbations according to the equation 9 and 12, where P_t is the concentration of PPIA and L_t is the concentration of Tau.* Change in chemical shift in the HSQC spectrum of PPIA in the presence and absence of Tau gives δ_H (in the proton dimension) and δ_N (in the nitrogen dimension). *The error value in K_d is the standard error of fitting.*

2.5.3. Quantification of PPIA-enhanced isomerization in PR20

2.5.3.1. Visualization of proline exchange in PR20

In order to visualize proline cis/trans isomerization in PR20, we utilized two-dimensional NOESY and ROESY experiments.

A two-dimensional NOESY spectrum of 100 µM PR20 was recorded on a 800 MHz NMR spectrometer (Bruker) at 298 K in 100 mM K_2HPO_4/KH_2PO_4 buffer, 10% D_2O, pH 7 using a NOE mixing time of 300 ms. The spectrum was assigned with the help of a two-dimensional TOCSY spectrum (mixing time of 80 ms) recorded for the same sample.

The two-dimensional ROESY spectrum of PR20/PPIA was recorded with 400 µM PR20 and a PR20:PPIA molar ratio of 8:1 on a 800 MHz NMR spectrometer (Bruker) using the same buffer and temperature conditions as used for the NOESY experiments. The mixing time for the ROESY experiment was 220 ms.

2.5.3.2. Estimation of the rate of exchange of proline in PR20

To estimate the rate of cis/trans exchange of prolines in PR20 in the presence of PPIA, NOESY spectra were recorded for mixing times ranging from 50 ms to 400 ms for the following PPIA:PR20 molar ratios:

Table 5: Conditions of measurement of rate of cis/trans proline isomerization in PR20.

PPIA:PR20	*PR20 conc.(µM)*	*Spectrometer*
1:30	*300*	*900 MHz*
1:8	*100*	*800 MHz*
1:4	*100*	*800 MHz*
1:1.5	*100*	*800 MHz*

The buffer and temperature conditions were identical to the reference condition. The spectra were processed with Topspin 3.6.2 (Bruker) and analysed with CCPN 2.4.2[214]

k_{ex} values, defined as sum of back and forward rates of a two-state model, were obtained according to[207,208]

$$\frac{I_{ex}}{I_{trans}} = \frac{1 - e^{(-k_{ex})*MT}}{e^{-k_{ex}*MT} + \frac{1 - X_{cis}}{X_{cis}}} \qquad 13$$

where I_{ex} is the intensity of the exchange peak between the cis and trans isoforms of H^{δ} of prolines, I_{trans} is the intensity of the of H^{δ} of the trans conformation, MT is the mixing time and X_{cis} is the fraction of the cis population. H^{δ} of prolines were chosen for analysis due to the well separated cis and trans peaks of these protons. The T_1 relaxation is considered to be similar for cis and trans proline peptides. Experimental data were fitted against the given equation, keeping k_{ex} and X_{cis} as free fit parameters, using least square fitting. The k_{ex} values were determined from both the exchange peaks on either side of the diagonal, and the k_{ex} reported

is the average of the two k_{ex} values derived per condition. The error in k_{ex} is the standard deviation from the average value.

Additionally, a similar analysis was done with the intensity ratio of the exchange peak (I_{ex}) to the cis diagonal peak (I_{cis}). In this case, the equation 13 was modified as follows

$$\frac{I_{ex}}{I_{cis}} = \frac{1 - e^{(-k_{ex})*MT}}{e^{-k_{ex}*MT} + \frac{1 - X_{trans}}{X_{trans}}} \qquad 14$$

where I_{ex} is the intensity of the exchange peak between the cis and trans isoforms of H^{δ} of prolines, I_{cis} is the intensity of the of H^{δ} of the cis conformation, MT is the mixing time and X_{trans} is the fraction of the trans population. X_{trans} was kept as free fit parameter during fitting. The k_{ex} were determined from both the exchange peaks on either side of the diagonal, and the k_{ex} reported is the average of the two k_{ex} values derived per condition. The error in k_{ex} is the standard deviation from the average value.

For determination of k_{ex} for PR20 in the presence of PPIA(R55A), the experiments were performed as described above in 100 mM K_2HPO_4/KH_2PO_4 buffer, 10% D_2O at pH 7.4 on a 700 MHz NMR spectrometer equipped with a cryoprobe.

The error in (I_{ex}/I_{trans}) was calculated from the noise in the NOESY spectra according to:

$$\sigma_{(I_{ex}/I_{trans})} = \left(\frac{I_{ex}}{I_{trans}}\right)\sqrt{\left(\frac{\sigma_{(I_{ex})}}{I_{ex}}\right)^2 + \left(\frac{\sigma_{(I_{trans})}}{I_{trans}}\right)^2} \qquad 15$$

where $\sigma_{(Iex/Itrans)}$ is the error in I_{ex}/I_{trans}, $\sigma_{(Iex)}$ and $\sigma_{(Itrans)}$ are the noise (RMS value of background noise) in the NOESY spectrum.

2.6. Isothermal titration calorimetry

2.6.1. Principle

Isothermal titration calorimetry or ITC is a useful method to characterize the thermodynamic aspects of protein/ligand interactions[215]. ITC measures the heat absorbed or released during molecular interactions[215,216]. The ITC instrument contains an adiabatic chamber that encloses a reaction cell, reference cell and a syringe. The reaction cell contains one of the interacting partners, usually the protein. The syringe holds the other interacting partner that is usually the

small ligand. The reference cell contains water. ITC detects the changes in heat as the ligand in the syringe is injected in steps to the interacting partner in the reaction cell. Heat changes are detected in comparison to the stable reference cell. The change in heat is plotted against the change in ligand concentration and is fitted against the binding model that is derived below.

Consider protein P in the cell titrated with ligand L. The heat change upon each injection can then be represented in terms of the change in concentration of PL complex (dPL), molar binding enthalpy(ΔH^0) and the volume in cell after each injection (V^0).

$$dQ = dPL.\Delta H^0.V_0 \qquad 16$$

Substituting P_f and L_f from equation 2 and 3 into equation 7 solves PL as shown below.

$$PL = \frac{P_t + L_t + K_d - \sqrt{(P_t + L_t + K_d)^2 + 4 * P_t L_t}}{2} \qquad 17$$

Taking the derivative of equation 17 gives the following

$$\frac{dPL}{dL_t} = \frac{1}{2} + \frac{1 - \left(1 + \frac{L_t}{P_t} + \frac{K_d}{P_t}\right) * \frac{1}{2}}{\sqrt{(1 + \frac{L_t}{P_t} + \frac{K_d}{P_t})^2 - 4 * \frac{L_t}{P_t}}} \qquad 18$$

Substituting equation 18 to equation 16 gives the following.

$$\frac{dQ}{dL_t} = \left(\frac{1}{2} + \frac{1 - \left(1 + \frac{L_t}{P_t} + \frac{K_d}{P_t}\right) * \frac{1}{2}}{\sqrt{\left(1 + \frac{L_t}{P_t} + \frac{K_d}{P_t}\right)^2 - 4 * \frac{L_t}{P_t}}} \right) * \Delta H^0 * V_0 \qquad 19$$

Equation 19 is the model used for fitting ITC data.

2.6.2. Experimental protocol and analysis

PPIA and PR20 stocks were prepared in 25 mM HEPES, 100 mM NaCl, 1 mM TCEP at pH 7.4. Forty-four micromolar PPIA in the cell was titrated with 650 µM PR20 in the syringe. The titration was performed at 10 °C employing 13 steps of injection. PPIA/buffer, buffer/PR20, and buffer/buffer titrations were also performed and assigned as controls for the analysis of the binding curve. Experiments were performed with a Malvern Microcal PEAQ-ITC instrument. During fitting the number of binding sites was fixed to one.

2.7. LLPS assays

2.7.1. PR20/tRNA LLPS

2.7.1.2. LLPS condition

RNA-induced PR20 LLPS was performed according to[102]. To this end, PR20 in 25 mM HEPES buffer, containing 0.01% NaN_3, at pH 7.4, was mixed with yeast tRNA reaching final concentrations of PR20 and tRNA of 100 µM and 0.2 mg/ml, respectively. The assay was prepared in nuclease-free water and additionally contained 0.4 units/µl of RNAsin to prevent nuclease activity.

To visualize enrichment of PR20 inside droplets, the primary amine at the amidated C-terminus of PR20 was labelled with Alexa 488 following the micro-labelling kit instructions from ThermoFisher Scientific, Invitrogen. Excess dye after labelling was removed by dialysis. 2 µM of Alexa 488-labelled PR20 was then added to non-fluorescent PR20 solution. To demonstrate enrichment of RNA inside the droplets, Syto 17 RNA dye was added to the assay just before tRNA such that its final concentration was 100 µM. Micrographs were acquired at 63X magnification using the L5(green) and Y5(red) filters on Leica DM6B fluorescent microscope. Contrast was enhanced using Image J in Fig. 23a for visualization purpose.

2.7.1.2. Recruitment experiment

To characterize the recruitment of PPIA to PR20/tRNA droplets, droplets of PR20 with tRNA were prepared at 25°C such that their final concentrations, including the volume of added PPIA, was 100 µM and 0.2 mg/ml, respectively. To prevent dimerization of PPIA, 1 mM DTT was present. To the preformed droplets, PPIA was added at PR20: PPIA molar ratios of 1:0.05, 1:0.2 and 1:0.4. To each sample, 5 µM Alexa 488-labelled PPIA mixed with its unlabelled kind to make up the required concentration, was also added. The same experiments were performed with the mutant PPIA(R55A) protein under identical conditions. To minimize the dilution effect on the droplets upon addition of PPIA or PPIA(R55A), their stocks in 25 mM HEPES buffer, 50 mM NaCl, 0.01 % NaN3, 0.5 mM DTT (pH 7.4) were concentrated and readjusted such that the added volume was only 4 % of the total assay volume in all cases. The samples were then observed under the microscope through the green fluorescence channel after 15 minutes of incubation at 25 °C. For calculation of recruitment ratios, raw green fluorescence images were used. The average intensity inside the droplet area was divided by the average intensity of a region of interest (ROI) just outside the droplet. Approximately 30 droplets of similar size were

analysed for each condition. To compute the statistical significance of the difference between the PPIA and PPIA(R55A) data set for a specific molar ratio, an unpaired t-test was performed using Graph-Pad Prism. For visualization purpose, the brightness and contrast are enhanced uniformly in Fig. 23b.

2.7.1.3. Dissolution experiment

To test the effect of higher concentrations of PPIA on PR20/tRNA droplets, droplets of PR20 with tRNA were prepared at 25 °C such that their final concentrations in the assay after the addition of PPIA were 100 µM and 0.2 mg/ml, respectively. Alexa 488-labelled PR20 and DTT were present at final concentrations of 2 µM and 1 mM, respectively. Wild-type PPIA or PPIA(R55A) were added to the preformed droplets at PR20: PPIA molar ratios of 1:05, 1:1, 1:3, 1:5. Prior to its addition to PR20/tRNA droplets, PPIA or PPIA(R55A) (in 25 mM HEPES, 50 mM NaCl, 0.5 mM DTT and 0.01 % NaN_3, pH 7.4) were concentrated and readjusted such that the added volume constituted only 17 % of the total assay volume. To ensure that the dilution effect did not affect the droplets, an additional control experiment was performed, where just buffer without PPIA, corresponding to 17 % of total assay volume, was added to the preformed droplets. All samples were incubated for 15 minutes at 25°C prior to imaging with the microscope. For visualization purposes, images in Fig. 23d were normalized to the same average background intensity before adjusting their contrast uniformly.

Granular areas were determined using ImageJ. To this end, the threshold value of intensity was set manually to pick up the area occupied by the fluorescently active droplets. The circularity value was set to 1. 'Analyse→Measure' (after selecting 'Area' in the 'Set Measurement' option) gave the area occupied by the droplets in the image. For all conditions, three to four images from different regions of the phase-separated sample were quantified.

2.7.2. Tau LLPS

2.7.2.1. LLPS condition

Tau phase separation was achieved at 20 µM concentration of Tau in 25 mM HEPES buffer containing 1 mM TCEP at pH 7,4, 25 °C. To visualize the enrichment of Tau inside the droplets, the phase separation assay was spiked with 0.5 µM of Alexa-488 labelled Tau. Alexa 488 labelling of Tau was carried out according to the micro-labelling kit instructions from Thermofischer Scientific. Micrographs were acquired at 63X magnification using the L5(green) on Leica DM6B fluorescent microscope.

2.7.2.2. Recruitment experiment

To estimate the recruitment of PPIA into Tau droplets, the Tau LLPS assay was prepared as described above, but without labelled Tau. To the preformed droplets, PPIA or PPIA(R55A) was added at Tau: PPIA/PPIA(R55A) molar ratios of 1:0.1 and 1:0.25. To each sample, 2.5 μM Alexa 488-labelled PPIA mixed with its unlabelled kind to make up the required concentration, was added. The volume of PPIA added at the end is limited to 13 % of the total volume so as avoid any dilution effect. The samples were then observed under the microscope after five minutes of incubation at 25 °C. The recruitment ratio was calculated as described for PR20. Approximately 20 droplets of similar size from two independent experiments were analysed for each condition. To compute the statistical significance of the difference between the PPIA and PPIA(R55A) data set for a specific molar ratio, an unpaired t-test was performed using Graph-Pad Prism.

2.7.2.3. Dissolution experiment

The impact of PPIA or PPIA(R55A) on Tau droplets at higher concentrations was tested for Tau:PPIA/PPIA(R55A) molar ratios of 1:1, 1:2.5 and 1:5. Tau droplets were prepared as described above and spiked with 0.5 μM Alexa 488 labelled Tau. To the preformed droplets of Tau, PPIA or PPIA(R55A) was added. The volume of the PPIA added at the end was limited to 20 % of the total assay volume. A control experiment was also performed were buffer was added instead of PPIA to the preformed Tau droplets. Samples were observed under the microscope after five minutes of incubation. The granular area from the microscopic images was determined using ImageJ as described for PR20/tRNA LLPS experiments. Approximately eight images were quantified from each independent experiments and three independent experiments were performed per condition.

2.7.2.4. Estimation of bound fraction of PPIA inside Tau droplets

In order to calculate the fraction of PPIA-bound Tau inside the droplets, we used the fluorescence micrographs recorded for Tau droplets formed by 20 μM Tau in 25 mM HEPES buffer, 1 mM TCEP at pH 7.4, spiked with Alexa 488-labeled Tau. Because the fluorescence intensity outside the droplets was very low (e.g. Fig. 28a), we made the simplifying assumption that Tau has been fully recruited into the droplet. Next, the average percentage area occupied by the droplet in the micrograph was estimated. This percentage area was extrapolated to the volume fraction occupied by the condensate assuming that the third dimension in the slice of the microscope focus is negligible. On the basis of these simplifications, we estimated the volume occupied by Tau droplets to be 1.5 % of the total volume. The concentration of Tau

inside the droplets was then estimated based on the effective increase of the 20 μM Tau concentrated into 1.5 % sample volume, which results in a concentration of 1333 μM Tau inside the droplets. The concentration of PPIA (or PPIA(R55A)) inside the Tau droplets was estimated from an average recruitment ratio of 5.0 observed for the Tau:PPIA (or PPIA(R55A)) molar ratio of 1:0.25 (Fig. 28c) *and from 1.5 % volume occupied by the droplets. A similar recruitment ratio was assumed for Tau:PPIA ratio of 1:0.5 and concentration of PPIA inside the Tau droplets were estimated for that condition as well. On the basis of these estimated concentrations of Tau and PPIA inside the droplets, equation 7 for a one-site binding model was used to estimate the fraction of PPIA-bound Tau inside the droplets.* P_f *is the concentration of free Tau,* L_f *is concentration of free PPIA and PL is the concentration of the Tau/PPIA complex inside the droplets.* K_d *is the binding affinity derived from the global fit analysis of the interaction of Tau with* ^{15}*N-labeled PPIA (or PPIA(R55A)).*

2.8. FRAP

2.8.1. Principle

Fluorescence recovery after photobleaching or FRAP is a useful technique to study the dynamics of molecules inside liquid condensate. FRAP requires the molecule of interest to be labelled with a fluorescent dye. The condensate sample, spiked with the labelled molecule is bleached in a given region with a laser beam. Then, the fluorescence recovery kinetics is measured which is an indicative of the diffusion rate of the labeled molecule in the condensate.

2.8.2. FRAP of PR20/tRNA droplets

FRAP experiments for PR20/tRNA droplets were performed on a Leica TCS SP8 confocal microscope with 63x oil immersion objective and a 561 DPSS laser line. For performing FRAP experiments, droplets of PR20/tRNA were spiked with 2 μM of TMR-labelled PR20. The region of interest (ROI) inside the droplet was bleached with fifteen iterations at 40 % laser power. The recovery was recorded over 500 frames, each corresponding to 523 ms. Experiments were performed on PR20/tRNA droplets between 15-35 minutes after its preparation, either only for PR20/tRNA droplets or for droplets in the presence of wild-type PPIA or PPIA(R55A) mutant protein. The PR20:PPIA/ PPIA(R55A) molar ratio was 1:0.4.

2.8.3. FRAP of Tau droplets

FRAP experiments for Tau protein droplets were performed on Zeiss LSM 880. Tau phase separation was achieved at 50 μM concentration of Tau in 100 mM PIPES buffer containing 1 mM MgSO4, 1 mM EGTA and 1mM DTT at pH 6,9 at 25 °C in the presence of 10 percent

dextran. Droplets were spiked with Alexa 488 labelled Tau. The region of interest inside the droplet was bleached with sixty iterations at 90 % laser power. The recovery was recorded over 424 cycles, each corresponding to 500 ms. Experiments were performed on Tau droplets soon after its preparation, either only for Tau droplets or for droplets in the presence of wild-type PPIA protein. The Tau:PPIAmolar ratio was 1:0.5.

2.8.4. Analysis

Images were analyzed using ImageJ. Fluorescence recovery was calculated for each time frame according to:

$$FRAP = \frac{I_{bleached} - I_{background}}{I_{av.prebleached}} \quad 20$$

where $I_{bleached}$ is the intensity of the bleached region, $I_{background}$ is the intensity of the background and $I_{av.preblaeched}$ is the average intensity of the ROI over a few frames before bleaching it.

The recovery curve obtained according to the above equation was then multiplied with an acquisition bleaching correction factor (ABCF) calculated as

$$ABCF = \frac{I_{reference} - I_{background}}{I_{av.reference}} \quad 21$$

where $I_{av.\ reference}$ is the average intensity of an ROI that is not bleached within the droplet. The fluorescence recovery curve thus obtained was then normalized for representation.

For PR20/tRNA droplets, fluorescence recovery of seven droplets of comparable size from two different samples were averaged for each condition. In the case of Tau droplets, three different droplets were averaged.

3. Results: Part 1

This section contains excerpts directly taken from the following publication. They are written in italic font. Figures reprinted from the publication are indicated in their corresponding legend.

Babu, Maria, et al. Nature communications 12.1, 3396 (2021); DOI: https://doi.org/10.1038/s41467-021-23691-y

3.1. PR repeat polymers interact with prolyl isomerases in vivo

According to proteomic studies, C9orf72 repeat polymers made up of PR and GR dipeptide repeat polmers interact with a large number of proteins in the cell[54,97,98,102,111,112,115,217,218]. Comparison of the corresponding interactomes identified by Lee et al 2016, *demonstrated that 65 proteins interact with PR but not GR repeat polymers[97]. Gene ontology analysis further showed that a class of PR-specific interactors are prolyl isomerases* (Fig. 16a). *The identified prolyl isomerases include PPIA, PPIB, and PPIF[97]. PPIA was independently identified as an interactor of PR repeat polymers in two other interactome studies[98,102,].*

3.2. PR repeat polymers inhibit protein folding activity

To gain insight into the consequences of the aberrant interaction of PR repeat polymers with prolyl isomerases, we performed RNase T1 *protein refolding assays.* The refolding rates of RNase T1 is limited by slow proline isomerization (section 2.3.1)[187,197]. *We unfolded the native structure of RNaseT1 in urea and later diluted* urea with buffer in order *to trigger refolding[187,197]. Upon dilution, RNaseT1 refolding started immediately and was completed within ~30 min* (Fig. 16b and SI Fig. 2)[197]. *We then refolded RNaseT1 in the presence of a large excess of a PR repeat polymer with 20 repeats (PR20). The refolding kinetics of RNaseT1 were unchanged in the presence of PR20* (Fig. 1b and SI Fig. 2).

Next, we performed refolding assays in the presence of the prolyl isomerase PPIA. In agreement with the ability of PPIA to catalyze the cis/trans isomerization of prolyl bonds[171,197], addition of PPIA strongly accelerated the folding of RNaseT1 (Fig. 16b and SI Fig. 2). *However, increasing concentrations of PR20 inhibited the catalyzing effect of PPIA in a dose-dependent manner* (Fig. 16b,c and SI Fig. 2). *The concentrations of PR20 to achieve inhibition are larger than those at which the immunosuppressant drug cylcosporin A inhibits the PPIA-catalyzed refolding of RNaseT1[171,197] , which is in agreement with the involved affinities: cyclosporin A binds three orders of magnitude stronger to the enzyme (13 ± 4 nM[219]) when*

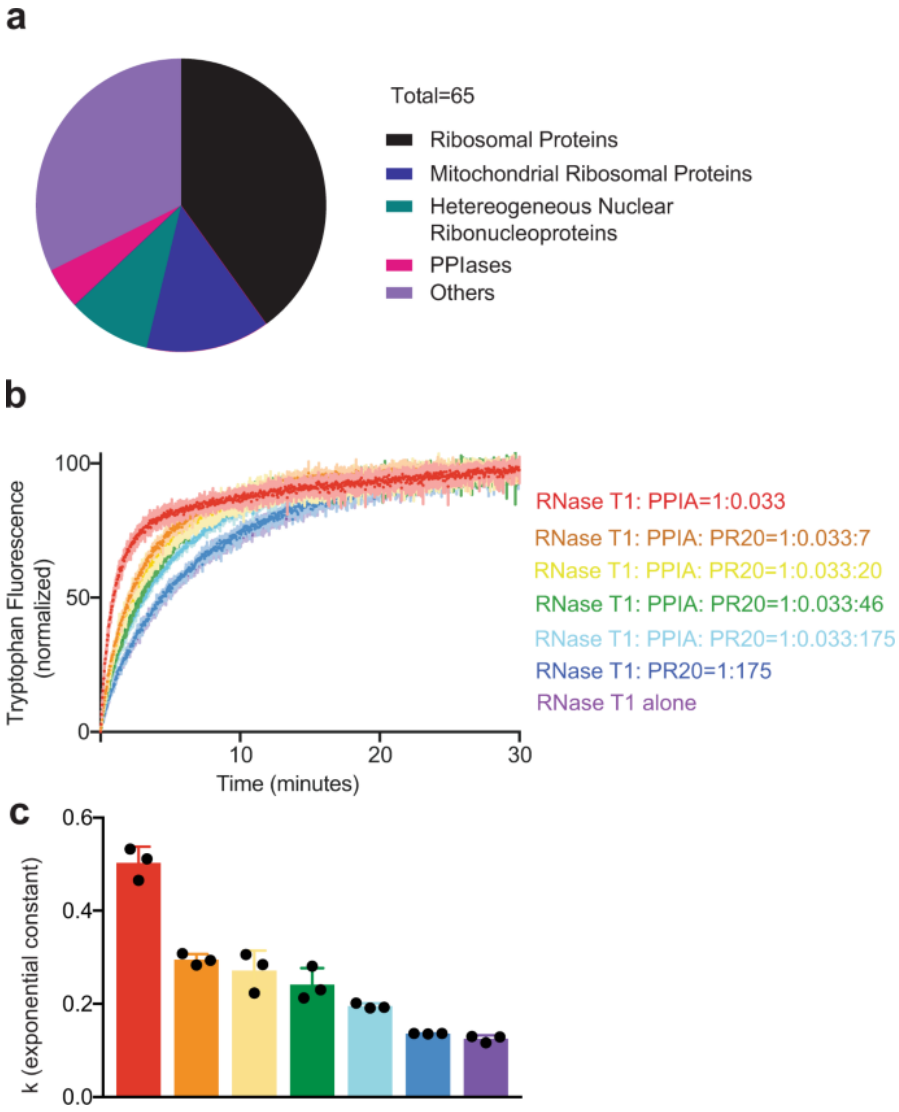

***Figure 16**: C9orf72-associated PR repeat polymers inhibit prolyl isomerase folding activity.*
***(a)**Classification of 65 PR repeat-specific interacting protein. The data for the analysis were taken from the list of dipeptide repeat polymer interactors identified by Lee et. al.(Table S1 in reference [97]) Only those interactions with a saint score[220] more than 0.9 were included. **(b)** Inhibition by the 20-dipeptide polymer PR20 of the catalytic effect of PPIA on protein folding of RNaseT1. The increase in fluorescence at 320 nm is shown as a function of the time of refolding in the absence of PPIA and PR20 (violet, "RNaseT1 alone"), and in the presence of a fixed concentration of PPIA and increasing concentrations of PR20 (red, orange, yellow, green, and light blue represent 0, 7, 20, 46, and 175 times excess of PR20 with respect to RNaseT1, respectively). The control experiment showing the refolding of RNaseT1 when PPIA is not present but PR20 has been added is also displayed (dark blue). **(c)** Histogram shows the mean value of the exponential folding rate constants k of RNaseT1 in the absence and presence of PPIA and increasing PR20 concentrations. Color coding as in b. n = 3 independent experiments were performed. Error bars represent standard deviation from mean value. k values of each independent experiment are shown in black dots for every condition.*
(Figure is reprinted from **Babu, Maria, et al.** Nature communications 12.1, 3396 (2021), with permission from Springer Nature.)

compared to the PR repeat polymer (~10–80 μM). The combined data show that C9orf72-associated PR repeat polymers do not affect the self-folding process of proteins, but selectively inhibit the folding catalyst activity of PPIA.

3.3. PR repeat polymers bind to the active site of PPIA

To gain molecular insight into the PR-mediated inhibition of enzyme-catalyzed folding, we analyzed the binding of PR repeat polymers to PPIA using NMR titration. *Upon addition of*

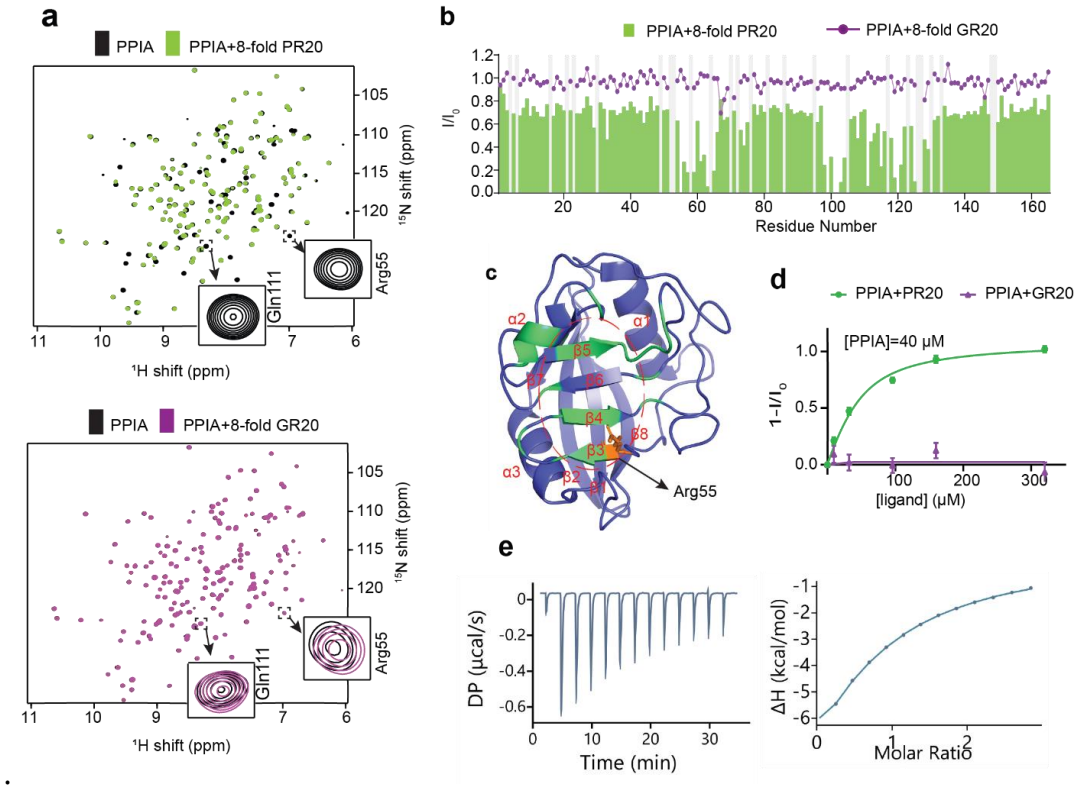

***Figure 17**: PR repeat polymers bind to the catalytic site of PPIA.*
***(a)** $^{1}H–^{15}N$ HSQC spectra of PPIA alone (black) and in the presence of an eightfold excess of PR20 (green), GR20 (magenta). Cross-peaks of residues, which are located in the substrate-binding pocket of PPIA, are highlighted. **(b)** Changes in the intensities of HSQC peaks of PPIA upon addition of an eightfold excess of PR20 (bars). I and I_0 are the intensities of the PPIA cross-peaks in the presence and absence of PR20. No broadening was observed upon addition of an eightfold excess of GR20 (line). **(c)** PPIA residues with strong PR20-induced signal attenuation are highlighted in the 3D structure of PPIA (PDB code: 5KUZ, https://www.wwpdb.org/pdb?id=pdb_00005kuz[186]). Arg55 is highlighted in orange. PPIA residues with I/I_0 values less than 0.394 (mean value of I/I_0 for all residues minus its standard deviation) upon addition of eightfold molar excess of PR20 are shown in green. The active site of PPIA is circled (dashed line).**(d)** Intensity changes of the cross peak of Arg55 in PPIA as a function of increasing concentration of PR20 and GR20. The lines represent least-square fitting of experimental data from which K_d values were derived. Error bars represent the error in $1-(I/I_0)$ calculated according to equation 11. (e). Isothermal titration calorimetry thermogram of PR20 binding to PPIA.*
(Figure is reprinted from **Babu, Maria, et al.** Nature communications 12.1, 3396 (2021), with permission from Springer Nature.)

increasing concentrations of the 20-repeat PR polymer PR20, the HSQC NMR signals of ^{15}N labelled PPIA broadened in a dose-dependent manner (Fig. 17a,b). *Because no new cross-peaks appeared in the NMR spectrum of PPIA upon addition of PR20, the exchange between the unbound and PR20-bound state of PPIA is in an intermediate to slow exchange regime.*

To identify the binding site of PR20 in PPIA, we analyzed the PR20-induced signal broadening for the individual residues of PPIA. The analysis located the strongest intensity decreases within or next to the enzyme's active site (Fig. 17b,c). Residue specific intensity analysis identified maximum peak broadening for the residues 55Arg-59Gln (sheet β3) , 61Met-63Gln (sheet β4), 98Leu-104Gly (sheet β5, loop β5- β6), 111Gln (loop β5- β6), 115Cys (sheet β6), 119Thr-121Trp (loop β6- α2, helix α2), 125Lys (loop α2-β7) which are centred around the hydrophobic binding pocket of PPIA (Fig. 17c). The strongly *perturbed PPIA residues include Arg55, Gln111, Asn102, and Glu120. Arg55 has been identified in previous X-ray studies of PPIA in complex with Xaa-proline dipeptides where this residue is shown to make hydrogen bonds to the proline carbonyl*[221]*. Gln111, on the other hand, is not making direct contacts with the PR20 chain, but is affected by mutation of Arg55 and is part of a dynamic network of residues in the binding pocket*[222]

Fitting the NMR broadening data of the catalytic residue Arg55 for increasing PR20 concentrations resulted in the dissociation constant 23 ± 7 μM for PPIA/PR20 interaction (Fig. 17d). *In addition, we quantified the affinity using isothermal titration calorimetry* (Fig. 17e). *The calorimetry-derived K_d value is ~50 μM. Notably, variations in K_d values were previously observed for PPIA interactions when different methods were used*[223,224]*. The NMR/calorimetry-derived micromolar affinity of the PR repeat polymer to PPIA is comparable to that of other PPIA/protein interactions*[223,224,]*.*

3.4. PPIA does not interact with other proline or arginine containing dipeptide repeat polymers

In order to confirm that the interaction of PPIA is specific for PR repeat polymer, we titrated PPIA with GR, AP, and GP dipeptide repeat polymers, formed in C9orf72-ALS/FTD (Fig. 17a, Fig. 18a). *No or very little broadening or shifts of the NMR signals of PPIA were observed*

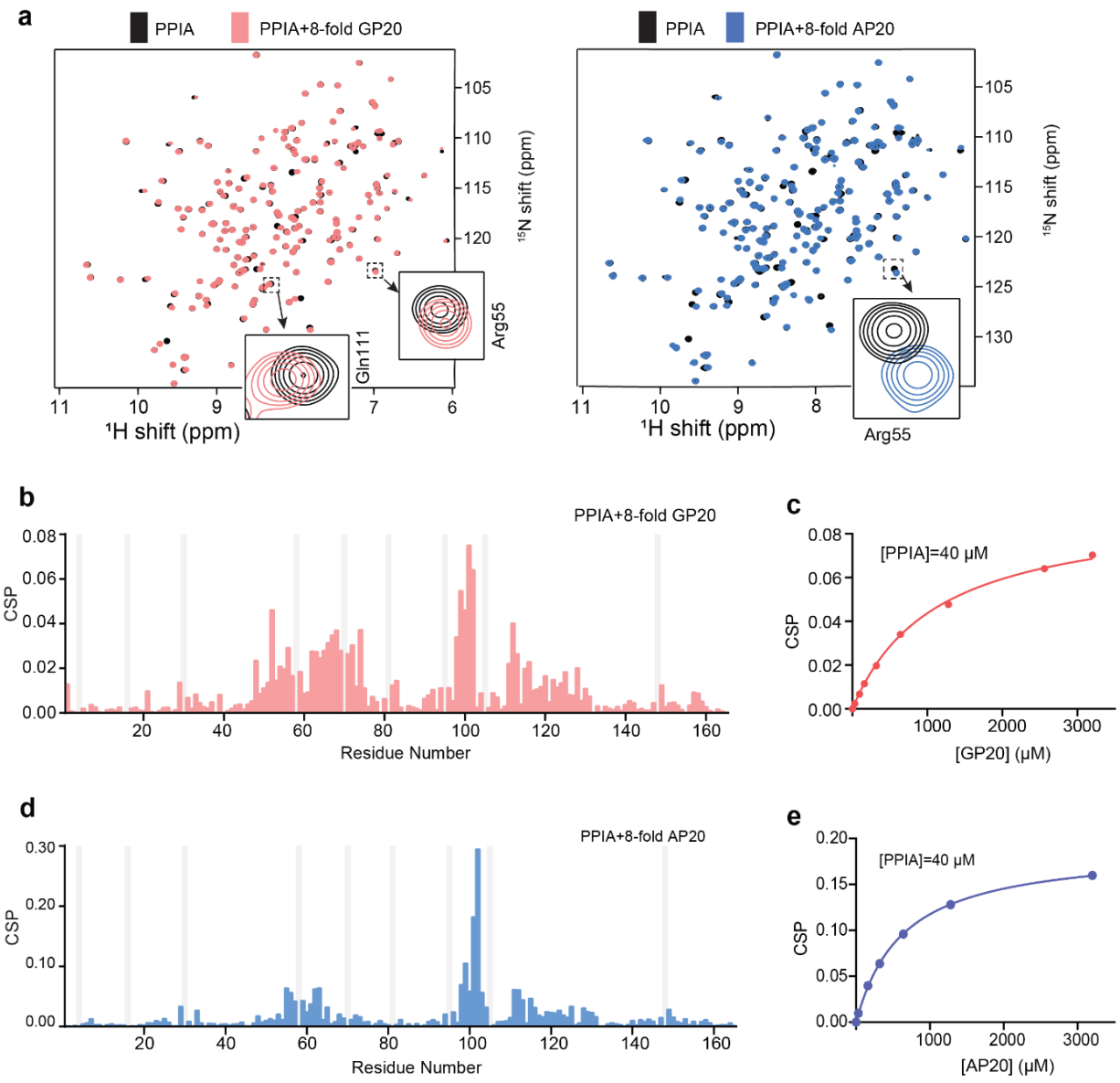

***Figure 18**: AP and GP repeat polymers bind weakly to PPIA.*
***(a)** $^{1}H–^{15}N$ HSQC spectra of PPIA alone (black) and in the presence of an eightfold excess of GP20 (red), and AP20 (blue). **(b)** Averaged ^{1}H-^{15}N chemical shift perturbations (CSPs) of HSQC peaks of PPIA upon addition of 8-fold excess GP20. **(c)** Averaged ^{1}H-^{15}N CSPs of Arg55 of PPIA for increasing GP20 concentrations. The lines represent least-square fitting of experimental data against equation 9 from which K_d values were derived. **(d)** Averaged ^{1}H-^{15}N chemical shift perturbations (CSPs) of HSQC peaks of PPIA upon addition of 8-fold excess of AP20. **(e)** Averaged ^{1}H-^{15}N CSPs of Arg55 of PPIA as a function of increasing AP20 concentration. The lines represent least-square fitting of experimental data against equation 9 from which K_d values were derived.*
(Figure is reprinted from **Babu, Maria**, **et al.** Nature communications 12.1, 3396 (2021), with permission from Springer Nature.)

when an eightfold excess of the 20-dipeptide polymer GR20 was added to PPIA (Fig. 17b). *The glycine/arginine repeat polymer thus does not bind to PPIA.* Titration of PPIA with 20 times repeat of either alanine/proline (AP) or glycine/proline (GP) dipeptides caused perturbations to the NMR signals of PPIA residues corresponding to its binding site (Fig. 18b,d). *However, AP20 and GP20 dipeptides displayed less signal broadening and more chemical shift changes in contrast to PR20* (Fig. 17a,b, Fig. 18a,b,d). *The binding processes are in the intermediate/fast for AP20, and in the fast exchange regime for GP20. The PPIA affinities of the dipeptide repeat polymers AP20 ($K_d = 597 \pm 12\,\mu M$) and GP20 ($K_d = 1188 \pm 64\,\mu M$) are more than one order of magnitude weaker than that of PR20* (Fig. 17d, Fig. 18c,e). Because GP20 and AP20 have the same number of proline residues as PR20, the analysis demonstrates that both proline and arginine residues are important for efficient binding of C9orf72-repeat polymers to prolyl isomerases.

3.5. Interaction of PPIA with PR repeat polymer depends on the repeat length

To gain insight into the critical length of PR repeat polymers for binding to prolyl isomerases, PPIA was titrated with PR polymers of decreasing repeat number. Repeat polymers with ten (PR10) and five (PR5) PR dipeptides efficiently bound to PPIA (Fig. 19a). The residues of PPIA that displayed perturbations upon binding to PR10 and PR5 were similar to that in the case of PPIA/PR20 binding. *For PR10 we determined the dissociation constant $27 \pm 5\,\mu M$), i.e. slightly lower than the PR20 affinity* (Fig. 19b). *In the case of PR5, the K_d value further decreased to $49 \pm 16\,\mu M$* (Fig. 19b). *Additional shortening of the peptide chain to two PR dipeptides abrogated the binding to PPIA: even an eightfold excess of PR2 did not influence the enzyme's NMR signals* (Fig. 19a).

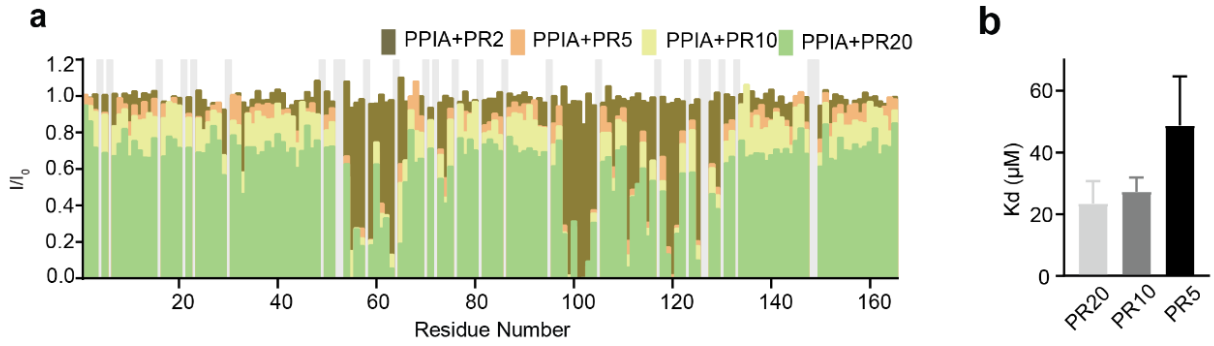

***Figure 19**: Strength of binding of PPIA to PR repeat polymers depends on the repeat length.*
***(a)** Residue-specific changes in the intensities of ^{1}H-^{15}N HSQC peaks of PPIA upon addition of 8- fold excess of PR20 (green), PR10 (yellow), PR5 (orange) and PR2 (brown). I and I_0 are the intensities of the PPIA HSQC cross peaks in the presence and absence of the PR repeats, respectively. **(b)** K_d values for the interaction of PPIA with PR20, PR10, and PR5 derived from the attenuation of the HSQC cross-peak of Arg55 of PPIA. Error bars represent the standard deviation in K_d generated from least-square fitting of experimental data to equation 9.*
(Figure is reprinted from **Babu, Maria**, **et al.** Nature communications 12.1, 3396 (2021), with permission from Springer Nature.)

3.6. Structure of PR repeat polymer in complex with PPIA

To reveal the structural basis of derailed protein homeostasis by PR repeat polymers, we determined the crystal structure of a PR repeat polymer in complex with the prolyl isomerase PPIA. The structure of the PR20/PPIA complex was resolved at 1.3 Å resolution (SI Tables 1 and 2). *In the heterodimeric complex, four PR repeats are in direct contact with the catalytic pocket of the enzyme* (Fig. 20a). *The functionally important PPIA-residue Arg55 forms hydrogen bonds with the carbonyl group of a proline–arginine peptide bond* (Fig. 20b and SI Fig. 3). *The proline residue in this specific peptide bond has a cis conformation, suggesting isomerase activity of PPIA on the PR repeat polymer. In addition, several other intermolecular contacts are present in the structure of the complex: Trp121 forms a hydrogen bond with the carbonyl group of the adjacent arginine–proline peptide bond; Asn102 and Glu120 of PPIA form hydrogen bonds with the arginine side chains of the PR repeat polymer* (Fig. 20b).

The crystal structure of the PR repeat polymer bound to the prolyl isomerase is unique when compared to known protein/ protein complex structures (Fig. 20c–e). *The chaperone-bound PR polymer chain displays a continuous electron density without interruption throughout the crystal lattice* (Fig. 20c–e). *However, the electron density of a single asymmetric crystal unit*

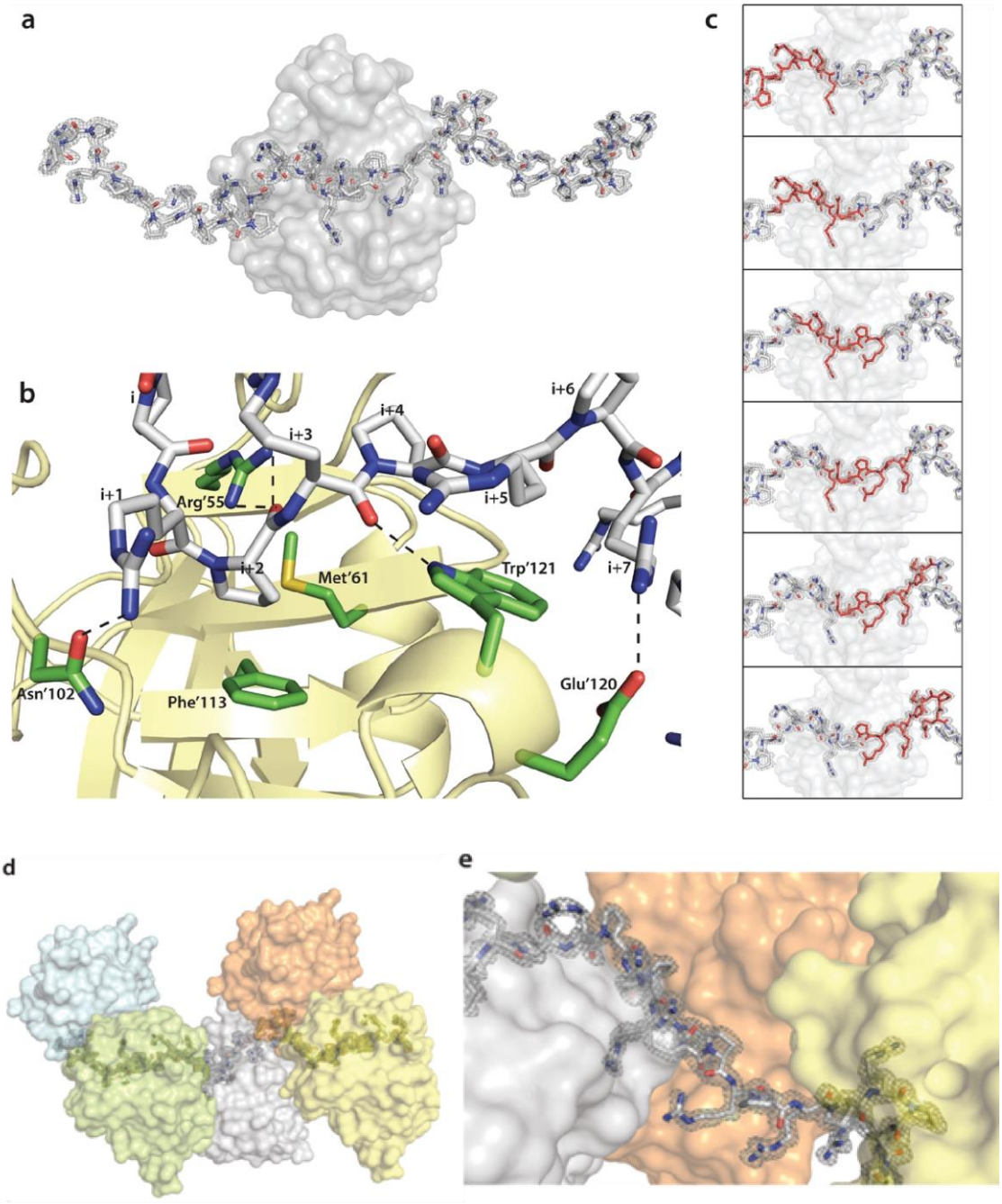

Figure 20*: Structural basis of chaperone inhibition by PR repeats.*
(a) *PR repeat polymer in complex with the ALS/FTD-associated prolyl isomerase PPIA. Only eight residues of the PR polymer could be built into the asymmetric unit; the displayed polymer chain was assembled from symmetry mates (2 mFo–DFc electron density map of PR20 contoured at 1.4σ level, depicted in gray).* ***(b)*** *Close-up view of the interface between the PR repeat polymer (gray) and PPIA (yellow/green). Hydrogen bonds are depicted by dashed black lines.* ***(c)*** *The continuous electron density for the PR polymer throughout the crystal lattice allowed a slider-like positioning of its N terminus.* ***(d),(e)*** *Selected regions from the crystal lattice displaying continuous electron density of the PR polymer chain (gray stick model with semi-transparent electron density). PPIA molecules are shown in surface representation.*
(Figure is reprinted from **Babu, Maria**, **et al.** Nature communications 12.1, 3396 (2021), with permission from Springer Nature.)

can only accommodate four PR dipeptides. Always four PR dipeptides from the polymer bind in an identical manner (residues I to I + 7 in Fig. 20b*) to the respective PPIA molecule in each asymmetric unit* (Fig. 20d, e). *Due to the continuous electron density of the PR chain in the crystal lattice, the PR repeats are randomly positioned, i.e. no unique start of the polymer chain is present* (Fig. 20c). *This suggests that the chaperone can bind to any of the PR dipeptides in the repeat polymer and the electron density is a result of this averaging process. The continuous electron density thus provides an atomic-resolution view of a large number of chaperone molecules bound to a long PR repeat polymer* (Fig. 20d).

4. Discussion: Part 1

This section contains excerpts directly taken from the following publication. They are written in italic font. Figures reprinted from the publication is indicated in their corresponding legend.

Babu, Maria, et al. Nature communications 12.1, 3396 (2021); DOI: https://doi.org/10.1038/s41467-021-23691-y

The link between C9orf72 hexanucleotide repeat expansion and ALS/FTD has been firmly established. Diverse molecular protein misfolding mechanisms including perturbation of membrane-less organelles and nucleocytoplasmic transport, amyloid formation of GA repeat polymers, as well as translation repression have been suggested to drive neuronal dysfunction[54,97-99,102,111,112,115,217,218,225]*. Dipeptide repeat polymer-associated toxicity is mediated by aberrant protein/protein and protein/RNA interactions, in particular of the arginine side chains of PR and GR repeat polymers to drive neuronal dysfunction*[54,97,98,102,111,112,115,217,218]*. However, PR repeat polymers were found to be more toxic than GR repeat polymers in cell and animal models of C9orf72-ALS/ FTD*[97,105,114]*. This indicates that the toxic mechanism of PR repeat polymers cannot be fully attributed to arginine residues, but depends on the unique combination of arginine with proline in PR repeat polymers.*

In this study, we uncovered a toxic mechanism specific to PR repeat polymers in C9orf72-ALS/FTD, which is based on the inhibition of isomerase activity of prolyl isomerase A. Our studies provide an instance for the enhanced toxicity of PR repeat polymers compared to other dipeptide repeats and emphasizes the importance of the specific combination of proline and arginine residue in driving the toxicity of hexanucleotide repeat expansion in C9orf72-ALS/FTD.

4.1. PR repeat polymers disrupt protein homeostasis in C9orf72-ALS/FTD by inhibiting PPIA

PPIA is a major cellular chaperone that catalyzes cis/trans isomerization of prolyl peptide bonds and thus helps proteins to fold when they exit from the ribosome (Fig. 21a)[171]. Using RNase T1 in vitro folding assay, we investigated the impact of the interaction of PR repeat polymers with PPIA on its catalytic activity. PPIA significantly accelerated the folding rate of RNase T1 through enhanced cis/trans proline isomerization. However, inclusion of PR20 along

with PPIA in RNAse T1 refolding assay diminished the chaperoning effect of PPIA in a PR repeat dose dependent manner (Fig 16b,c). *It tells that PR repeat polymers inhibit the folding catalyst activity of PPIA, thereby contributing to the disruption of protein homeostasis* (Fig. 21a)[80].

Our NMR and crystallographic studies revealed that PR repeat polymers achieve the inhibition of PPIA activity by competitively binding to its isomerase activity site (Fig. 17b,c Fig. 20a,b **).** Arg55, which is known to be critical for isomerization of proline in the substrate, was engaged in making contacts with prolines in PR repeat polymers (Fig. 17a-d, Fig. 20b). *When we then compare the PPIA/PR complex structure with the structure of PPIA in complex with the natural immunosuppressant cyclosporin A[226], we find a similar inhibition mechanism:in both complexes the side chain of Arg55, which is critical for catalysis of PPIA-mediated cis/trans isomerization[227], forms strong contacts with the molecule that inhibits PPIA's folding catalyst activity* (Fig. 21b).

Binding studies with GR, PA and GP repeat polymers provided insights into the structural basis of the specific binding of the PR repeat polymer to PPIA. GR20 did not bind to PPIA at all, thereby emphasizing the need for proline residues in the dipeptide repeat polymers to bind to the isomerase activity site of PPIA (Fig. 17.b,d). Although AP20 and GP20 bind to PPIA, their affinities are low when compared to that of PR20 with PPIA (Fig. 18b-e). The reduced binding of GP20 and AP20, that contains the same number of prolines as in PR20, reveals that arginines in the PR repeat polymers are also crucial for the strong interaction of PR repeat polymer with PPIA. This is further visible in the crystal structure of PPIA/PR repeat polymer complex, where proline residues in PR repeat polymer bind to the Arg55 residue in the enzymatic site of PPIA, while arginines provide intactness to the binding by making contacts with other enzymatic site residues of PPIA (Fig. 20b). Our results are in agreement with with the findings of previous in vivo proteomic analysis studies which recognized prolyl isomerases as exclusive binding partners of PR repeat polymers (Fig. 16a)[97].

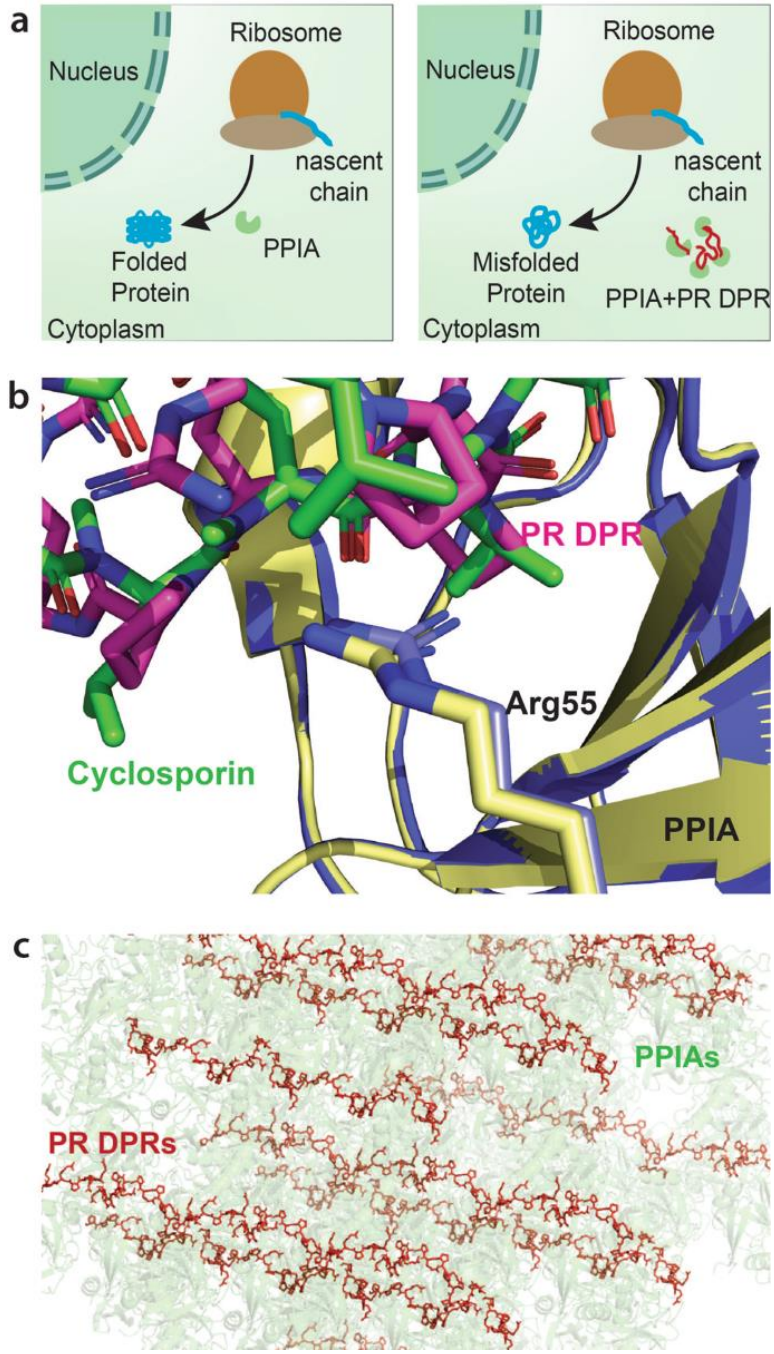

Figure 21*: Inhibition and sequestration of prolyl isomerases by C9orf72-ALS/FTD-associated PR repeat polymers.*
(a) *In normal conditions not associated with disease, prolyl isomerases such as PPIA catalyze the cis/trans isomerization of prolyl peptide bonds and thus help proteins to fold when they exit from the ribosome. PR dipeptide repeat polymers (DPR; red chains) translated from hexanucleotide repeat expansion in the non-coding region of the C9orf72 gene, bind to the active site of prolyl isomerases and thus block their ability to catalyze protein folding.* ***(b)*** *Comparison of the active site of the prolyl isomerase PPIA (blue/yellow) in complex with the immunosuppressant drug cyclosporin A (green; PDB code: 1CWA, https://www.wwpdb.org/pdb?id=pdb_00001cwa[226]) and a PR repeat polymer (pink).* ***(c)*** *Crystal lattice of the PPIA/PR20 complex illustrating the dense packing of PPIases (green) that is possible on long PR dipeptide repeat polymers (DPR, red).*
(Figure is reprinted from **Babu, Maria**, **et al.** Nature communications 12.1, 3396 (2021), with permission from Springer Nature.)

4.2. Toxicity of PPIA/PR repeat polymer interaction will enhance with increase in the length of repeats

We found that short PR repeat proteins bind with micromolar affinity to the prolyl isomerase PPIA. This affinity is comparable to values reported for other protein substrates[223,224]*, but lower than the nanomolar affinity of the drug cyclosporin*[219]*. However, long PR polymers can potentially bind many chaperones simultaneously: based on the crystal structure of the PPIA/PR20 complex a single PR polymer with a repeat size of 400 can sequester up to 100 prolyl isomerase molecules. In addition, the molecular mechanism changes from a simple one-site binding process to the binding to a one-dimensional lattice with a huge number of potential binding sites* (Fig. 21c)[228]*. Aberrant interactions of C9orf72-repeat polymers might thus be mechanistically similar to the binding of transcription factors to DNA in which transcription factors bind to the one-dimensional lattice of binding sites in the DNA*[228]*. When PPIA molecules bind to proximal sites in the effectively one-dimensional lattice of the PR repeat chain, direct interactions between PPIA molecules might further contribute to avidity in the inhibition of PPIA by PR dipeptide repeat polymers. Taken* together *our study provides a molecular mechanism for the derailment of protein homeostasis by PR repeat polymers in C9orf72-associated neurodegenerative diseases. In addition, it warrants further studies to investigate the interaction of PR repeat polymers with PPIA in neurons including their subcellular localization.*

5. Results: Part 2

This section contains excerpts directly taken from the following publication. They are written in italic font. Figures reprinted from the publication are indicated in their corresponding legend.

Babu, Maria, et al. Journal of the American Chemical Society 144.35, 16157–16163 (2022) ; DOI: https://doi.org/10.1021/jacs.2c07149

5.1. PPIA and its activity site mutant bind with different affinities to PR repeat polymers

To understand the effect of PPIA on the phase separation of proline rich IDPs, we used the complex coacervate of a PR repeat polymer with RNA[102]. PR20, comprising 20 repeats of the - PR dipeptide - was utilized for our studies. Prior to checking the effect of PPIA on PR20 condensate formed with RNA, we compared the binding affinities of PPIA and an active site mutant of PPIA towards PR20.

The dipeptide repeat polymer PR20 interacts with PPIA in cells[97]. Section 3.3 and 3.6 describes the invitro interaction of PPIA with PR20. Here, *we repeated the* NMR titration experiments *with the mutant protein PPIA(R55A), in which Arg55 is mutated to alanine*[184]. *This mutation was previously shown to attenuate its binding to substrates and to decrease its cis/trans isomerization activity. In contrast to wild-type PPIA, only little signal broadening was observed in the* ^{1}H-^{15}N *correlation spectrum of PPIA(R55A) upon addition of PR20* (Fig. 22a-c). *Only a few residues in the active site experienced residual chemical shift perturbations, in particular Asn102* (Fig. 22b), *which is in contact with an arginine side chain of PR20 in the PPIA/PR20 complex* (Fig. 20b). *Comparison of the intensity perturbations of Arg55 and its mutant Ala55 at increasing PR20 concentrations, highlights the strong difference in affinity of PR20 to wild-type PPIA and the mutant PPIA(R55A)* (Fig. 22d).

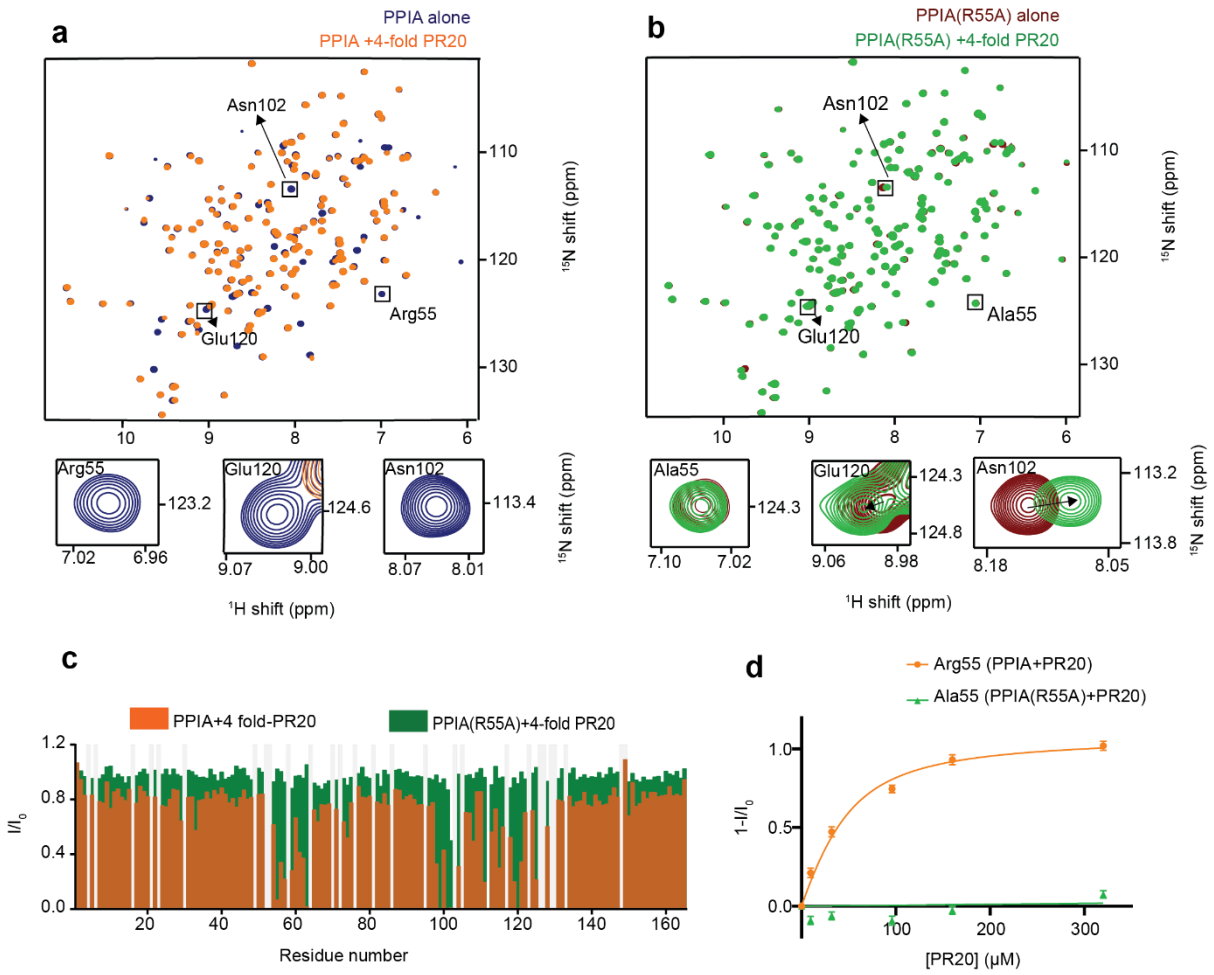

.

***Figure 22**: PR20 binds to wild-type and mutant PPIA with different affinities.*
***(a)** Two-dimensional ^{1}H-^{15}N HSQC spectra of PPIA alone (blue) and in presence of a 4-fold excess of PR20 (orange). Highlighted are the cross peaks of Arg55, Glu120 and Asn102, which are predominantly in the slow exchange interaction regime. These residues are in direct contact with PR20 in the PPIA/PR20 complex. **(b)** ^{1}H-^{15}N HSQC spectra of PPIA(R55A) alone (maroon) and in the presence of a 4-fold excess of PR20 (green). The cross peak of Ala55 is unaffected by the addition of PR20, Glu120 shows very small chemical shift changes while Asn102 is in fast-to-intermediate exchange. **(c)** Single-residue analysis of the interaction of PR20 with wild-type and mutant PPIA. Changes in the intensities of ^{1}H–^{15}N HSQC peaks of PPIA (orange) and PPIA(R55A) (green) upon addition of a 4-fold excess of PR20. I and I_0 are the intensities of the PPIA HSQC peaks in the presence and absence of PR20, respectively. Light gray bars represent residues that are excluded from the analysis.**(d)** Intensity changes of the cross peak of Arg55 in PPIA and Ala55 in PPIA(R55A), as a function of increasing concentration of PR20. The lines represent least-square fitting of the experimental data of Arg55 from which the K_d value was derived. The K_d value for the PPIA/PR20 interaction derived from the Arg55 cross peak is 23± 7.28 μM. The same could not be estimated for the PPIA(R55A)/PR20 interaction because of minimal perturbations. Error bars represent error in 1-I/I_0 calculated from the noise in the NMR spectra according to equation 11.*

5.2. PPIA modulates PR20/RNA condensate

Next, we investigated the effect of PPIA on the complex coacervation of PR20 with RNA. Previous studies showed that PR20 efficiently forms liquid-like droplets upon addition of tRNA[102,196]*. Consistent with these studies, we observed LLPS of 100 μM PR20 when mixing it with 0.2 mg/mL tRNA* (Fig. 23a). *Using fluorescence microscopy, PR20/tRNA droplets were observable for ~1–1.5 h after mixing the two components* (SI Fig. 4). *A similar time-dependent instability of peptide–RNA coacervates was previously reported*[131]*. The effect of PPIA on PR20/tRNA droplets was therefore studied during this time window.*

We then quantified the degree of PPIA recruitment into PR20/tRNA droplets. This was achieved by calculating the ratio of fluorescence intensity of PPIA inside and outside of similar-sized droplets. For different PR20:PPIA molar ratios (1:0.05, 1:0.2, 1:0.4, i.e., a large excess of PR20 over PPIA), PPIA concentrated inside the PR20/tRNA droplets (Fig. 23b,c). *We also repeated the experiments with the mutant PPIA(R55A). Fluorescence microscopy showed that PPIA(R55A) concentrates inside of PR20/tRNA droplets* (Fig. 23b,c). *Its recruitment was slightly attenuated when compared to wild-type PPIA, likely due to the lower affinity to PR20* (Fig. 22d).

We then investigated the effect of higher concentrations of PPIA and PPIA(R55A) on PR20/tRNA droplets. PPIA (PPIA(R55A)) was added to the droplets at PR20:PPIA molar ratios of 1:0.5, 1:1, 1:3, and 1:5 (Fig. 23d). *The mutant PPIA did not dissolve the PR20/tRNA droplets at the tested concentrations* (Fig. 23d,e, SI Fig. 4). *At 5-fold excess of PPIA(R55A) over PR20, the amount of droplets was slightly decreased* (Fig. 23d,e, SI Fig. 4), *potentially due to residual binding* (Fig. 22b,c). *In contrast, we observed immediate complete dissolution of the PR20/tRNA droplets upon addition of a 3- or 5-fold molar excess of wild-type PPIA. At equimolar concentrations of wild-type PPIA and PR20, PR20-LLPS was partially diminished* (Fig. 23d,e, SI Fig. 4). *We attribute the finding that at equimolar concentration the droplets are not fully dissolved to a combination of factors, including the incomplete recruitment of PPIA to the droplets* (Fig. 23c) *and the competition between PPIA and RNA for binding to PR20.*

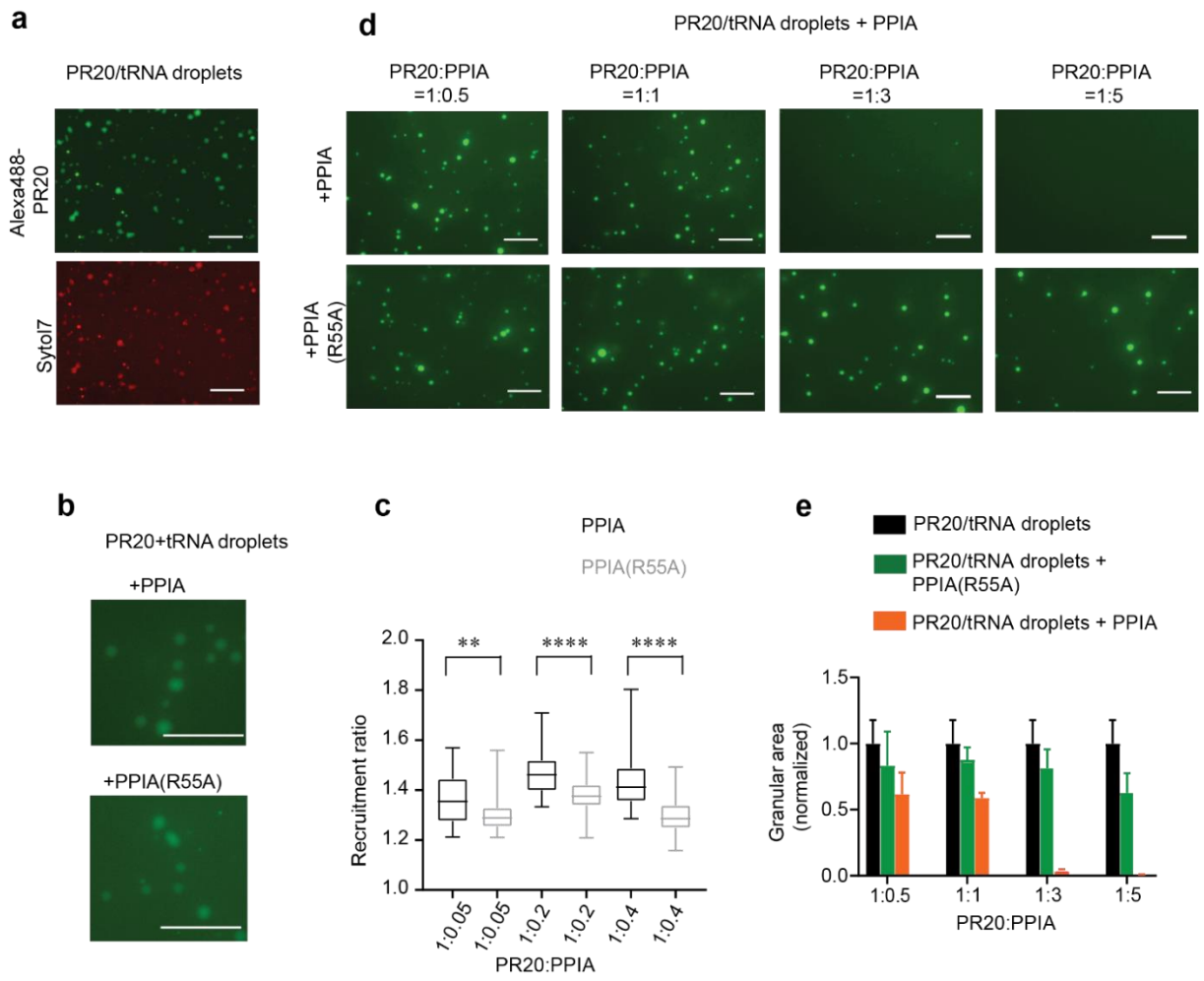

Figure 23*: PPIA interferes with RNA-induced LLPS of PR20.*
(a) *LLPS of PR20 into PR20/tRNA droplets. Droplets were visualized by addition of Alexa488-labeled PR20 (green) and Syto 17 RNA dye (red). Images were obtained after 15 min of incubation. Scale bar, 20 μm.* ***(b)*** *Micrographs showing the recruitment of PPIA (top) and PPIA(R55A) (bottom) into PR20/tRNA droplets. Recruitment of PPIA variants into the preformed droplets are shown for the PR20:PPIA and PR20:PPIA(R55A) molar ratio of 1:0.2. Localization of PPIA variants inside the PR20/tRNA droplets were visualized by labelling them with Alexa-488 green fluorescent dye. Images were obtained after 15 minutes of incubation. Scale bar, 20 μm.* ***(c)*** *Concentration of PPIA inside PR20/tRNA droplets. Recruitment ratios calculated on the basis of ~30 droplets for each PR20:PPIA (black) and PR20:PPIA(R55A) (gray) molar ratio. In the box and whisker plot, the middle line is the median, ends of boxes represent the upper and lower quartiles, while whiskers extend until the highest and lowest observations. The difference within a PR20:PPIA ratio was analyzed by an unpaired t test: **p < 0.0017, ****p < 0.0001. For p < 0.05, the two data sets are considered to be significantly different.* ***(d)*** *PPIA-induced dissolution of PR20/tRNA droplets. Fluorescence images of Alexa488-labelled PR20/tRNA droplets at increasing PPIA (top) and PPIA(R55A) (bottom) concentrations are shown from left to right. Images are obtained after 15 minutes of incubation. Scale bar, 20 μm.* ***(e)*** *Granular areas occupied by PR20/tRNA droplets 15 min after addition of wild-type PPIA (orange) or mutant PPIA(R55A) (green) for PR20:PPIA (or PPIA(R55A) ratios of 1:0.5, 1:1, 1:3, and 1:5. Granular areas in a control sample without PPIA are displayed in black. Granular area is taken as the average of area occupied by droplets in four micrographs. Error bars represent standard deviation from average.*

Next, we probed the effect of PPIA on the dynamics of PR20 inside the PR20/tRNA droplets. PPIA (or PPIA(R55A)) was added to PR20/tRNA droplets at a substoichiometric PR20:PPIA (1:0.4) molar ratio. We photobleached fluorescently labeled PR20 inside the droplets and recorded the recovery rate (Fig. 24a). *The rate of fluorescence recovery was similar in the presence of either PPIA or PPIA(R55A)* (Fig. 24b). *In addition, the recovery rate was comparable to that in a reference sample where neither variant was present. This showed that PPIA did not affect the dynamics inside PR20/tRNA droplets at this low PPIA concentration.*

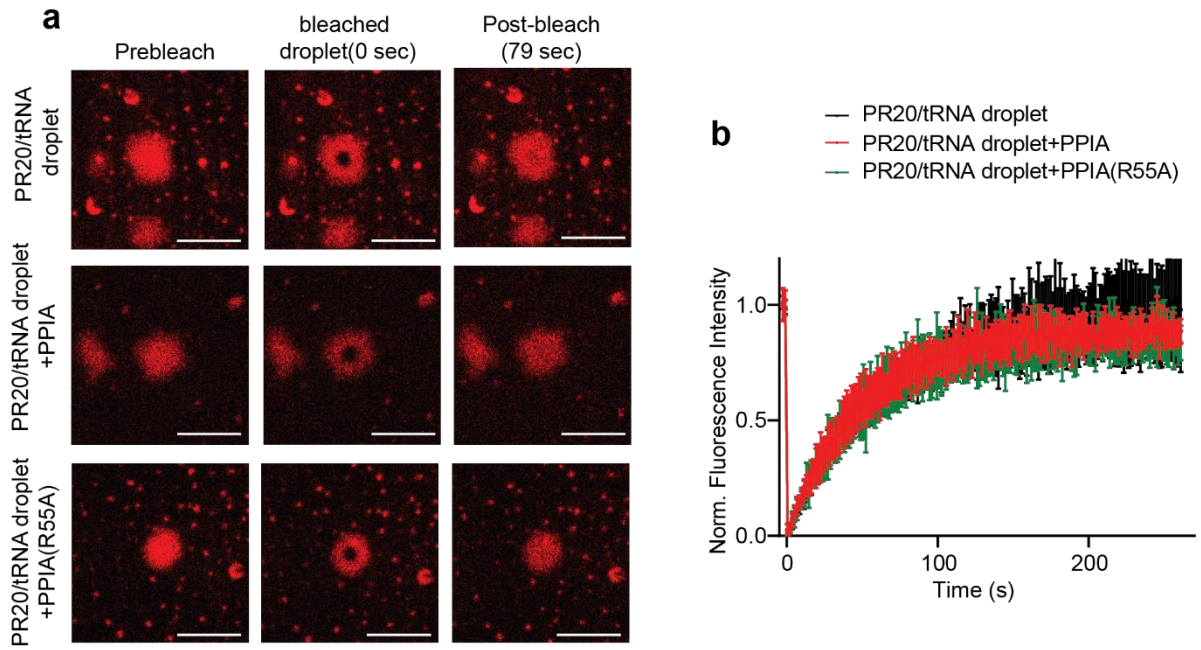

***Figure 24**: Fluorescence recovery of TMR-labelled PR20 inside PR20/tRNA droplets.*
***(a)** Micrographs showing PR20/tRNA droplets (top row), PR20/tRNA droplets in the presence of PPIA (middle row) and in presence of PPIA(R55A) (bottom row) before bleaching, soon after bleaching (0 sec) and 79 seconds after bleaching. PPIA variants are added to preformed droplets of PR20/tRNA at PR20:PPIA variant ratio of 1:0.4. Scale bar, 5 μm. **(b)** Averaged fluorescence recovery curve after photobleaching of PR20/tRNA droplets alone (black), and in the presence of PPIA (red) and PPIA(R55A) (green). Error bars represent standard deviation from average recovery curve calculated from seven droplets per condition.*

5.3. PPIA enhances the isomerization of prolines in PR20

To investigate the ability of PPIA to catalyze the cis/trans isomerization of the proline residues of PR20, we utilized NOESY and ROESY NMR spectroscopy. NOESY and ROESY experiments are powerful methods to probe two-state exchange processes within the range of the NOE/ROE mixing time (10^{-3} s) including proline isomerization[207]. In the two-dimensional NOESY spectrum of PR20 in the dilute state in the absence of RNA, all prolines and all the arginine

residues have overlapping chemical shifts because of the repeat nature of the peptide. The NOESY spectrum of PR20 recorded in the presence of PPIA, when compared to the same for PR20 alone, displayed an additional exchange cross peak between the cis and trans isoforms of H^{δ} of proline (Fig. 25a). *This exchange peak suggests that the cis/trans exchange of arginine–proline peptide bonds in PR20 shifted in the presence of PPIA to a faster time scale, which is detectable within the NOESY observation time. To verify that the additional cross peak is an exchange peak, a ROESY spectrum was recorded. In the ROESY spectrum, the same sign of the additional peak with respect to the diagonal peak confirmed an exchange process as the source of this cross peak* (Fig. 25a).

To quantify the enhancement in isomerization rate in PR20 in the presence of PPIA, the cis/trans interconversion rate (k_{ex} value) was determined for PPIA:PR20 molar ratios of 1:30, 1:8, 1:4, and 1:1.5. Experimental data, i.e., the ratio of intensity of the exchange peak to that of the trans diagonal peak (or the cis diagonal peak), derived from NOESY spectra with mixing times ranging from 50 to 400 ms were fitted according to the two-state exchange model for proline isomerization (Fig. 25b,d). *The cis/trans interconversion rates for proline in a peptide are on the order of 10^{-3} s^{-1} in the absence of isomerases*[176]. *The k_{ex} value estimated for prolines of PR20 in the presence of PPIA was higher than this value by about 3 orders of magnitude. The average k_{ex} values derived from the intensity ratio of the exchange peak to the trans diagonal peak are 1.33 ± 0.01 s^{-1}, 6.05 ± 0.11 s^{-1}, 9.64 ± 0.46 s^{-1}, and 17.13 ± 0.77 s^{-1} for PPIA:PR20 molar ratios of 1:30, 1:8, 1:4, and 1:1.5, respectively* (Fig. 25b,c). *When derived from the intensity ratios of the exchange peak to the cis diagonal peak, we obtained 2.99 ± 0.20 s^{-1}, 8.45 ± 0.08 s^{-1}, 14.86 ± 1.03 s^{-1}, and 20.80 ± 7.36 s^{-1}, respectively* (Fig. 25d,e). *The later k_{ex} values are less accurate, because of the low signal intensity of the cis diagonal peak* (Fig. 25a). *We attribute the differences in the k_{ex} values derived from the two ways of analysis to the inaccuracies in the later "cis" analysis. Notably, the interconversion rate gradually increases with increasing PPIA concentration and the dependence of k_{ex} on PPIA concentration starts to saturate at higher PPIA concentrations (PPIA:PR20 of 1:1.5)* (Fig. 25c,e).

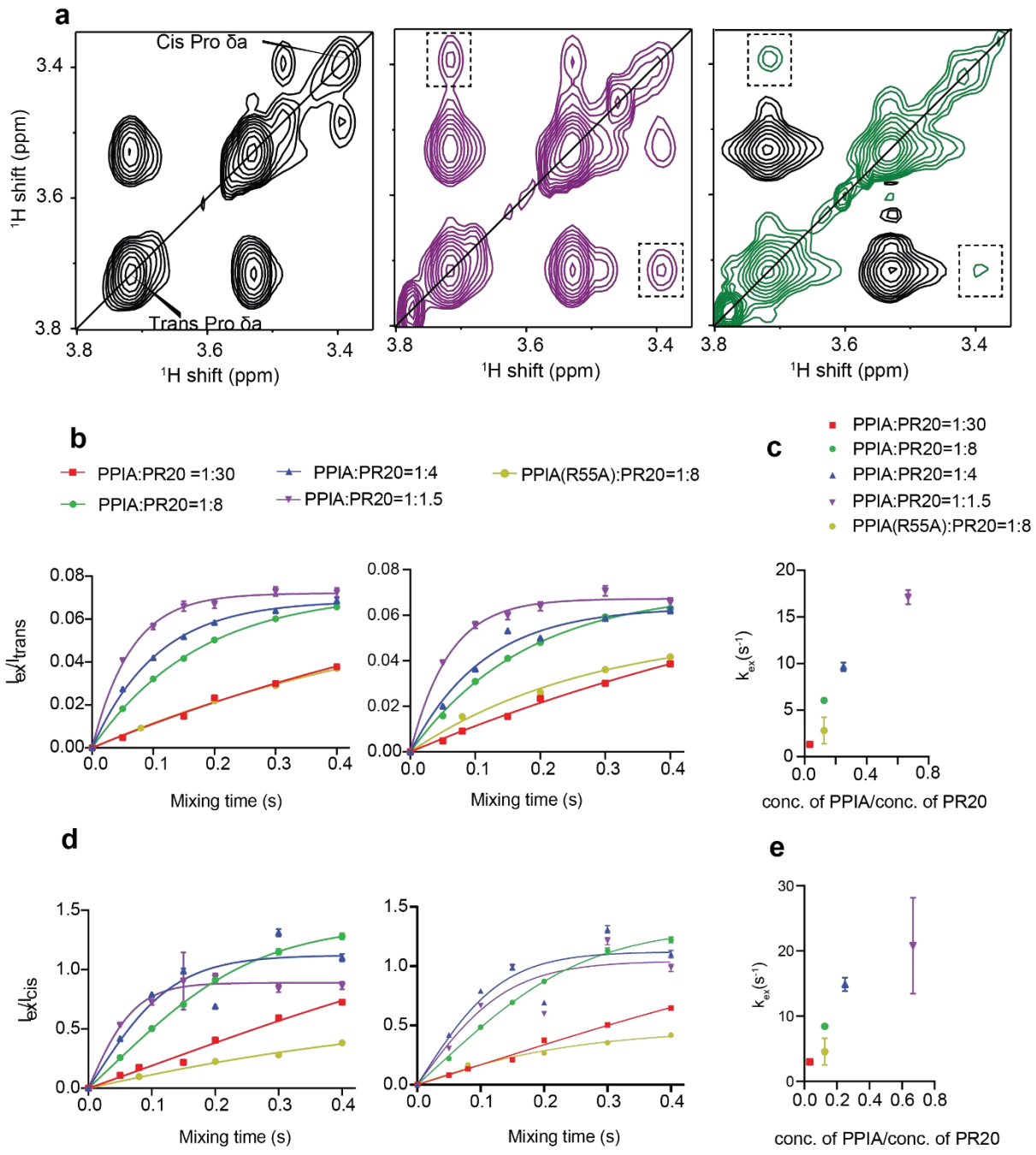

***Figure 25**: Isomerase activity of PPIA on the dipeptide repeat protein PR20 in the dilute state in the absence of RNA.*
***(a)** NOESY spectrum of PR20 alone (left) and in the presence of PPIA (middle; PPIA:PR20 molar ratio of 1:8) in the region of H_δ of prolines. The exchange peak between the cis and trans isoforms of H_δ proline is marked by a rectangle. For comparison, the ROESY spectrum of the same PPIA/PR20 sample is shown on the right. The mixing time for the NOESY experiments is 300 ms; for the ROESY it is 220 ms. **(b)** Ratios between the intensity of the cis/trans exchange peak of proline H_δ , I(ex), and the intensity of its trans diagonal peak, I(trans), as a function of mixing time of the NOESY experiment for PPIA:PR20 molar ratios of 1:30 (red, square), 1:8 (green, circle),1:4 (blue, triangle), and 1:1.5 (magenta, inverted triangle) and for a PPIA(R55A):PR20 ratio of 1:8 (yellow, circle). Lines represent least-squares fittings of the data against equation 13 to obtain the exchange rate k_{ex}. Error bars represent the error in I_{ex}/I_{trans} calculated from the noise in the NMR spectra. The graphs on the left and*

right represent the same analysis, but the I_{ex} value in the two cases is taken from the two exchange peaks on either side of the diagonal, which are marked by rectangular boxes in panel a (middle). ***(c)*** *Rates of cis/trans interconversion, k_{ex}, in PR20 for different PPIA:PR20 ratios derived from fitting the I_{ex}/I_{trans} value corresponding to various mixing times against equation 13. k_{ex} values here are the average of the two k_{ex} values, derived per condition, from the two different fitting analysis shown in panel b.Error bars represent standard deviations from the average k_{ex} value.* ***(d)*** *Ratios between the intensity of the cis/trans exchange peak of proline H_{δ} , I(ex), and the intensity of its cis diagonal peak, I(cis), as a function of mixing time of the NOESY experiments. Color coded as in panel d. Lines represents least-square fittings of the data against equation 14 to obtain the exchange rate k_{ex}. Error bars represent error in I_{ex}/I_{cis} calculated from the noise in the NMR spectra. The graphs on left and right represent the same analysis but the I_{ex} value in the two cases are taken from the two exchange peaks on either side of diagonal, which are marked by rectangular boxes in panel a (middle).* ***(e)*** *Rates of cis/trans interconversion, k_{ex}, in PR20 for different PPIA:PR20 ratios derived from fitting the I_{ex}/ I_{cis} value corresponding to various mixing times against equation 14. k_{ex} values here are the average of the two k_{ex} values, derived per condition, from the two different fitting analysis shown in panel d. Error bars represent standard deviations from the average k_{ex} value.*

Following the same strategy, we then determined the k_{ex} value of proline isomerization in PR20 in the presence of the mutant PPIA(R55A) (Fig. 25b-e). *At an 8-fold excess of PR20 over PPIA(R55A), the k_{ex} value obtained from the intensity ratio of the exchange peak to the trans diagonal peak was 2.82 ± 1.42 s^{-1}, and that from the intensity ratio of the exchange peak to the cis diagonal peak 4.56 ± 2.03. The k_{ex} values in the presence of the mutant PPIA(R55A) are thus approximately a factor 2 lower than with the wild-type PPIA* (Fig. 25c,e). *This demonstrates the residual activity of PPIA(R55A). A complete inhibition of the enzymatic activity would require a full blockage of the binding, underlining the difficulty of disentangling the effect of binding and isomerization on droplet dissolution.*

5.4. PPIA and its activity site mutant have weak affinities towards Tau

Next, we investigated if PPIA is able to reverse LLPS of a proline-rich IDP, which does not require nucleic acids for LLPS. We selected the 441 residue protein Tau (Fig. 26a), *because it has – in addition to its importance for disease – several useful properties: (i) more diverse amino acid sequence when compared to PR20, (ii) a high content of proline residues in the so-called proline-rich region* (Fig. 26a), *which is important for Tau LLPS*[229], *and (iii) robust self-coacervation at room temperature*[131]. *First, we characterized the binding of PPIA to tau using NMR* (Fig. 26b,d). *Residue-specific analysis showed that PPIA decreases the signal intensity of many tau cross peaks in the 2D ^{1}H–^{15}N HSQC. The strongest signal attenuation was detected at the N-terminus of tau, in and close to the two N-terminal inserts N1/N2, the proline-rich domain, repeats R1 and R3, and the C-terminal region* (Fig. 26d). *Much less signal broadening was induced in the tau cross peaks when the mutant PPIA(R55A) was added* (Fig. 26c,d).

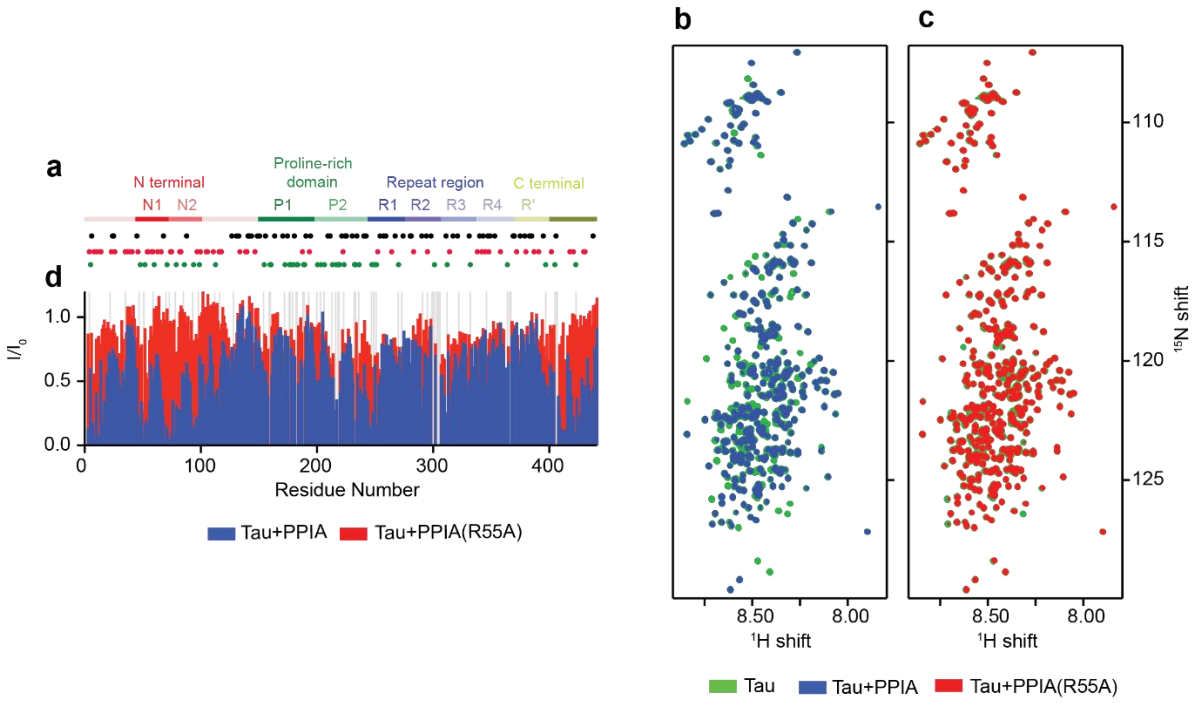

***Figure 26**: Binding of Tau to wild-type and mutant PPIA.*
***(a)** Domain organization of tau comprising the N-terminal domain, the proline-rich domain (P1 and P2), the repeats R1, R2, R3, R4, and R', and the C-terminal domain. The locations of prolines are marked by green dots. Black and red dots represent positively and negatively charged residues, respectively.**(b)** Superposition of two-dimensional ^{1}H-^{15}N HSQC spectra of Tau alone (green) and in the presence of a 10-fold excess of PPIA (blue). **(c)** Superposition of the ^{1}H-^{15}N HSQC spectra of Tau alone (green) and in the presence of a 10-fold excess of PPIA(R55A) (red). **(d)** Changes in the intensities of $^{1}H-^{15}N$ HSQC peaks of tau upon addition of a 10-fold excess of PPIA (blue) and PPIA(R55A) (red). I and I_0 are the intensities of the tau HSQC peaks in the presence and absence of PPIA (or PPIA(R55A)), respectively. Gray bars represent residues that are excluded from the analysis.*

In order to gain further insights into the PPIA/tau interaction, we titrated ^{15}N-labeled PPIA with unlabeled tau (Fig. 27a,c)*. Only at very high molar excess of tau over PPIA did we detect changes in the position and intensity of the PPIA cross peaks. This is in strong contrast to the NMR data for the PPIA/PR20 titration, in which strong signal broadening already occurred at 4-fold excess of PR20 over PPIA* (Fig. 22c)*. We then performed a residue-specific analysis of the tau-induced chemical shift perturbations in PPIA* (Fig. 27c)*. The analysis showed that the tau-induced changes were located in PPIA's enzymatic pocket* (Fig. 27d)*. Fitting the concentration-dependent chemical shift perturbation (CSP) of Arg55 to a one-site binding model results in a K_d value of 353 ± 30 μM* (Fig. 27e) *. We then performed a global fit of the CSPs of several strongly perturbed residues (Arg55, Met61, Ser99, Phe113, Thr119, Leu122) and obtained a K_d value of 194 ± 39 μM. The affinity of the PPIA/tau interaction is thus*

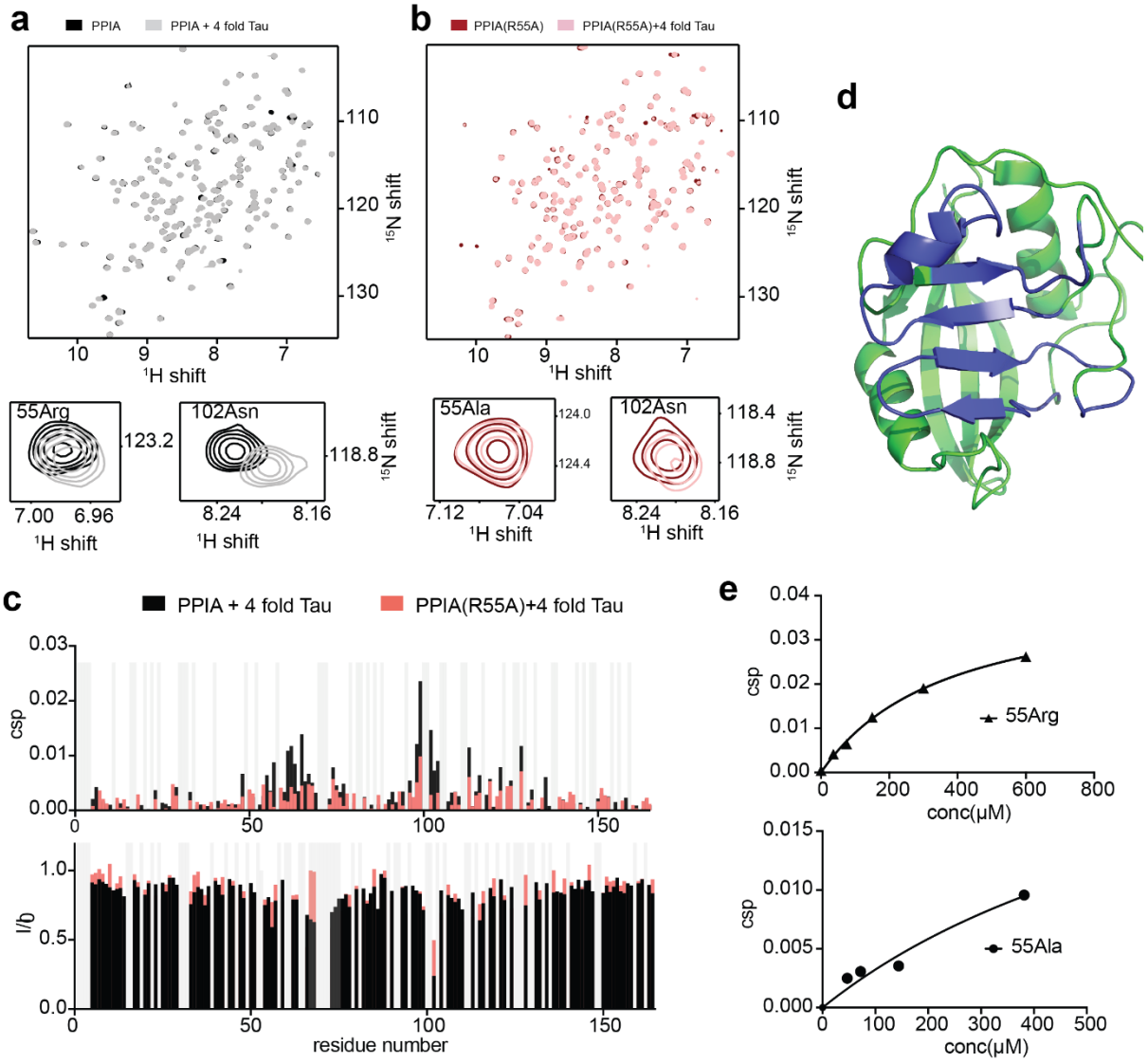

***Figure 27**: Tau binds weakly to wild-type and mutant PPIA.*
***(a)** Two-dimensional ^{1}H-^{15}N HSQC spectra of PPIA alone (black) and in presence of a 4-fold excess of Tau (gray). Highlighted are the cross peaks of Arg55 and Asn102 that are present in the binding site of PPIA. **(b)** ^{1}H-^{15}N HSQC spectra of PPIA(R55A) alone (maroon) and in the presence of a 4-fold excess of Tau (light pink). Highlighted are the cross peaks of Ala55 and Asn102. **(c)** Single-residue analysis of the interaction of Tau with wild-type and mutant PPIA. Chemical shift perturbations and intensity perturbations of ^{1}H-^{15}N HSQC peaks of PPIA (black) and PPIA(R55A) (pink) upon addition of 4-fold excess of Tau are shown above and below, respectively. Gray bars represent residues that were excluded from the analysis. **(d)** Residues of PPIA that shows significant chemical shift perturbations due to interaction with Tau are mapped onto the crystal structure of PPIA (PDB code: 5kuz, https://www.wwpdb.org/pdb?id=pdb_00005kuz[186]) in blue colour. **(e)** Chemical shift perturbations of the cross peaks of Arg55 of PPIA (left), and of Ala55 of PPIA(R55A) (right), as a function of increasing concentration of Tau. The line represent least square fitting of the experimental data against equation 9. The K_d value for the PPIA/Tau interaction derived from the Arg55 cross peak is 353 ± 30 μM μM. The same for PPIA(R55A)/Tau interaction derived from Ala55 is 817 ± 74 μM.*

approximately a magnitude weaker than the PPIA/PR20 interaction. On the basis of the calculated K_d values, we estimate that at the conditions of the NMR experiment shown in Fig. 26d, *~49% (global fit; 35% for the R55-fit) of tau molecules are bound to PPIA. Because the degree of PPIA-induced signal broadening largely exceeds those values in several tau regions* (Fig. 26d), *we conclude that a sizeable fraction of the signal broadening induced in tau upon PPIA addition likely arises from PPIA-catalyzed cis/trans isomerization of tau's proline residues.*

We also titrated ^{15}N-labeled mutant PPIA(R55A) with tau. We observed chemical shift perturbations that were weaker than those of the wild-type PPIA/tau interaction (Fig. 27b,c), *while the signal broadening was comparable* (Fig. 27c). *Estimation of the K_d on the basis of the chemical shift perturbation returned values of 817 ± 74 μM (for Arg55;* Fig. 27e) *and 562 ± 83 μM (for global fit). Thus, the PPIA-bound fraction of tau molecules in the NMR experiment of* Fig. 26d *is 19% (on the basis of the Arg55 K_d) and 26% (for the global fit K_d).*

5.5. PPIA modulates the droplets of Tau

Next, we studied the impact of both wild-type and mutant PPIA on tau LLPS. Tau undergoes LLPS at 20 μM concentration in a buffer of low ionic strength (Fig. 28a)[131]. *When PPIA is added, it is enriched 4–6-fold inside the tau droplets* (Fig. 28b,c). *A similar enrichment was observed for the mutant PPIA(R55A)* (Fig. 28b,c). *The more pronounced enrichment of PPIA inside tau droplets (4–6-fold) when compared to PR20/tRNA droplets (~1.4) suggests that in the case of PR20/tRNA the competitive binding between PPIA and tRNA to PR20 decreases the enrichment of PPIA inside the PR20/tRNA droplets.*

In subsequent experiments, we added PPIA to preformed tau droplets at 1:1, 1:2.5, and 1:5 molar ratios (Fig. 28d). *This caused a strong decrease in tau droplet numbers already at equimolar concentration* (Fig. 28d,e). *In the case of the mutant PPIA(R55A), less dissolution was detected* (Fig. 28d,e). *We further note that lower concentrations of PPIA are required to dissolve tau droplets than PR20/tRNA droplets, despite the reduced affinity of PPIA to tau.*

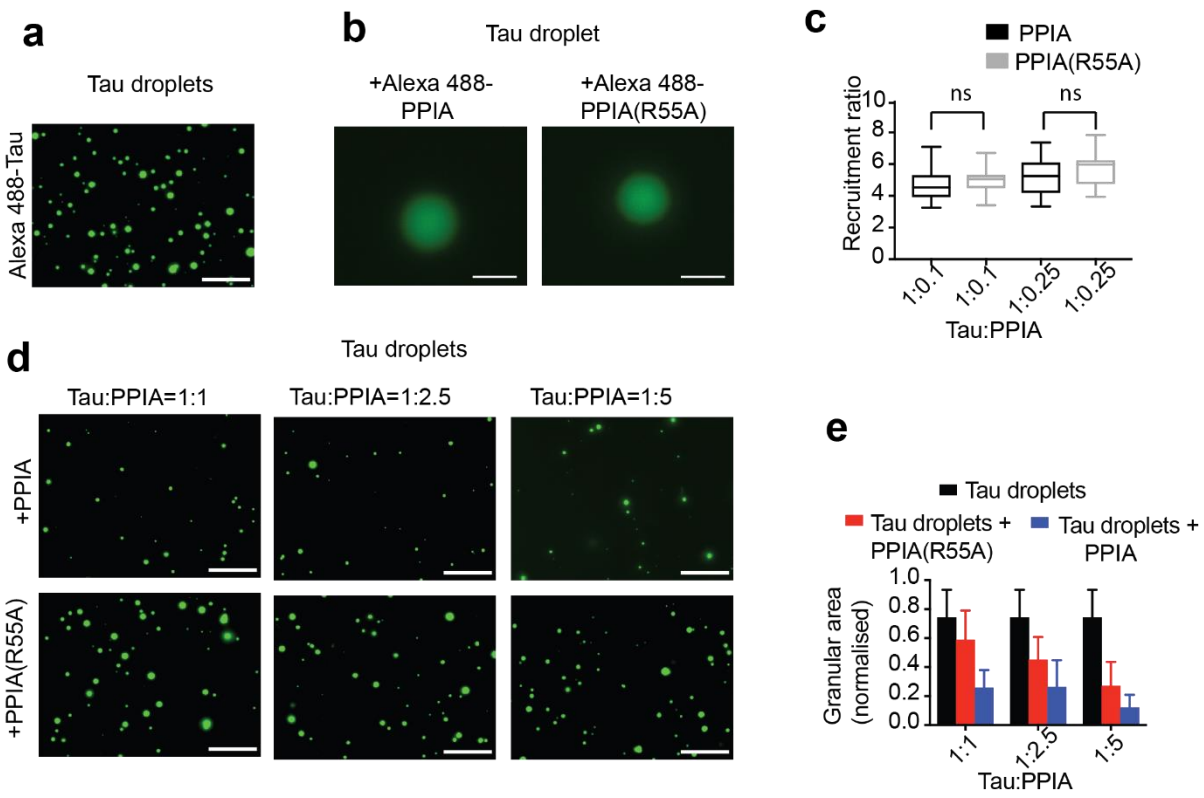

***Figure 28**: PPIA modulates tau LLPS.*
***(a)** LLPS of tau. Droplets were visualized by addition of Alexa488-labeled tau (green). Image was recorded after 5 min of incubation. Scale bar, 30 μm **(b)** Recruitment of PPIA (left) and PPIA(R55A) (right) to a Tau droplet. The Tau to PPIA or PPIA(R55A) molar ratio was 1:0.1. The PPIA variants were labelled green with the fluorescent dye Alexa-488 . Images were obtained after five minutes of incubation. Scale bar, 5 μm. . **(c)** Concentration of PPIA inside tau droplets. Recruitment ratios calculated on the basis of ~20 droplets for each tau:PPIA (black) and tau:PPIA(R55A) (gray) molar ratio, obtained from two independent experiments per condition. In the box and whisker plot, the middle line is the median, ends of the boxes represent the upper and lower quartiles, while whiskers extend until the highest and lowest observations. An unpaired t test gave no significant difference between PPIA and PPIA(R55A) recruitment ratios. ns stands for no significant difference, i.e., $p > 0.05$. **(d)** PPIA-induced dissolution of Tau droplets. Fluorescence images of Alexa488-labelled Tau droplets at increasing PPIA (top) and PPIA(R55A) (bottom) concentrations are shown from left to right. Images were obtained after five minutes of incubation. Scale bar, 30 μm. **(e)** Granular areas occupied by tau droplets 5 min after addition of wild-type PPIA (blue) or mutant PPIA(R55A) (red) for PR20:PPIA (or PPIA(R55A)) ratios of 1:1, 1:2.5, and 1:5. Granular areas in a control sample without PPIA are displayed in black. Granular area is taken as the average of area occupied by droplets, calculated from 24 images from three repeats (8 images from one repeat) per condition. Error bars represent standard deviation from average area.*

Next, PPIA was added to tau droplets at a tau:PPIA molar ratio of 1:0.5. Fluorescently labeled tau inside a region of the droplet was photobleached, and the recovery was recorded (Fig. 29a). *The recovery rate was comparable for tau droplets in the presence and absence of PPIA* (Fig. 29b). *Thus, for both droplet systems, tau and PR20/RNA, recruitment of PPIA did not cause a detectable change of the liquidity of the protein/polypeptide inside the droplets.*

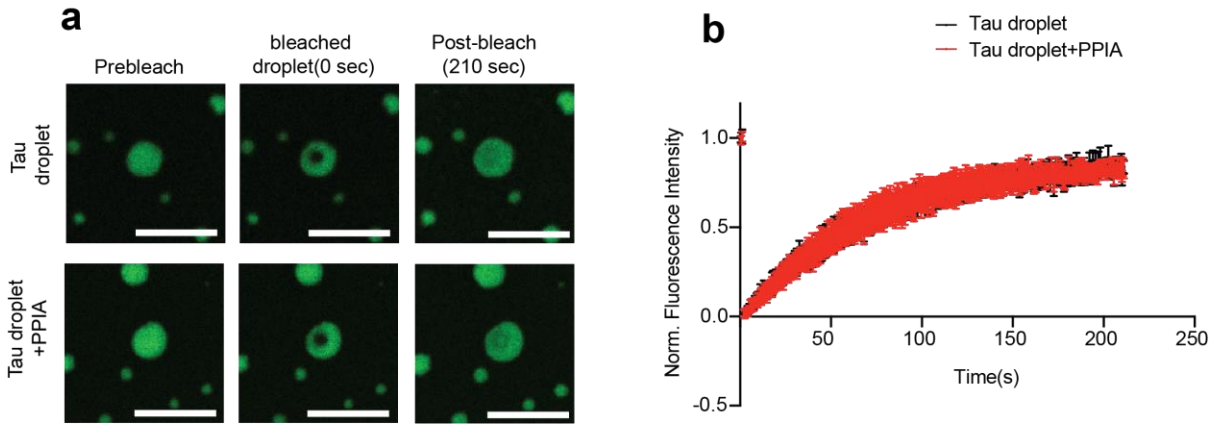

Figure 29*: Fluorescence recovery of Alexa488-labelled Tau inside Tau droplets.*
(a) *Micrographs showing Tau droplets (top row), and Tau droplets in the presence of PPIA (bottom row) before bleaching, immediately after bleaching (0 sec) and 210 seconds after bleaching. PPIA was added to preformed droplets of Tau at PR20:PPIA ratio of 1:0.5. Scale bar, 6 µm.* ***(b)*** *Averaged fluorescence recovery curve after photobleaching of Tau droplets alone (black), and in the presence of PPIA (red). Error bars represent standard deviation from average recovery curve calculated from three droplets per condition.*

6. Discussion: Part 2

This section contains excerpts directly taken from the following publication. They are written in italic font.

Babu, Maria, et al. Journal of the American Chemical Society 144.35, 16157-16163 (2022) ; DOI: https://doi.org/10.1021/jacs.2c07149

6.1. PPIA modulates the condensate of proline rich IDPs

Liquid-liquid phase separation of biomolecules facilitates formation of membraneless compartments in response to cellular needs[119]. As proteins inside condensate are susceptible to misfolding ad aggregation, the proper regulation of the condensate dynamics is essential. *Different chaperones have been investigated with respect to their regulatory role in biomolecular LLPS[160-164,230] but the role of PPIA or other prolyl isomerases, despite the abundance of phase separating proteins in its interactome[190], remained unexplored.*

We investigated the effect of PPIA on the complex coacervate of PR20 with RNA and the self-assembled condensate of Tau (Fig. 23, Fig. 28). We observed that PPIA can migrate into the self-assembled Tau condensate as well as the complex coacervate of PR20 with RNA. In addition, PPIA dissolved both the condensates at its stoichiometric concentrations. The ability of PPIA to modulate these proline-rich systems suggest their cellular role in regulating phase separation of proline-rich proteins

6.2. Isomerization of prolines in Tau by PPIA must be crucial for its dissolution

PPIAs are special when compared to other chaperones for two reasons: (i) they preferentially bind to proline residues, and (ii) they catalyze proline cis/trans isomerization. Generally, it is difficult to decouple these two processes, because both occur at the active site; that is, point mutations affect both processes. Despite the strong connection between binding to the active site and catalysis of proline isomerization, the modulatory action of PPIA on tau LLPS points to a significant contribution of proline isomerization to the PPIA-mediated dissolution of tau droplets (Fig. 28). *Binding of PPIA to tau is very weak such that in both the dilute phase and, even more, inside the droplets, where tau is highly concentrated, only a small fraction of tau molecules are bound to PPIA. When we make some simplifying assumptions such as (i) all tau is inside the droplet (in agreement with negligible tau fluorescence outside; Fig. 28a,d), (ii)*

the area occupied by the droplets is directly correlated to the volume, i.e., the third dimension of the slice observed under the microscope is considered negligible, and (iii) one-site binding of tau to PPIA, we estimated the fraction of PPIA-bound tau inside the droplets as ~1.5% at the tau:PPIA molar ratio of 1:0.25 (3.4% at the tau:PPIA molar ratio of 1:0.5). Because the recruitment of wild-type PPIA and mutant PPIA(R55A) into the droplets is very similar (Fig. 28c) *and the affinity of PPIA(R55A) is only ~2–3-fold lower* (Fig. 27e)*, this value changes only to ~1.2% at the tau:PPIA(R55A) molar ratio of 1:0.25 (2.7% at the tau:PPIA(R55A) molar ratio of 1:0.5). In contrast, we find that PPIA drastically remodels the conformational ensemble of tau as seen by PPIA-induced signal broadening of the tau backbone resonances* (Fig. 26d). *This remodeling is largely absent for the mutant PPIA* (Fig. 26d). *We thus suggest that the stronger dissolution power of PPIA when compared to PPIA(R55A)* (Fig. 28d,e) *is linked to the wild-type protein's ability to remodel the conformational ensemble of tau through proline isomerization.*

6.3. Outlook

In the current study we have investigated the regulatory role of the proline isomerase PPIA on liquid-like droplets freshly formed by two proline-rich IDPs. Changes in the material properties of droplets from a liquid-like state to more solid phases, however, have been linked to amyloid formation, for example in the case of the ALS/FTD-related protein FUS and also for tau[147,157]. It will therefore be interesting to study how PPIA and other proline isomerases modulate the maturation kinetics of condensates. Because of the strong changes induced in the conformational ensembles of IDPs by proline isomerization, the maturation kinetics of condensates could be affected by proline isomerases. Supportive for this hypothesis are studies in cells: PPIA expression was essential for stress granule formation in hematopoietic cells in conditions of oxidative stress[190], and knock out or age-dependent reduction of PPIA decreased stress granules[190].

In summary, our work establishes a regulatory role of proline isomerases on the liquid–liquid phase separation of proline-rich IDPs. Targeting proline isomerases by small molecules might thus provide a viable strategy to modulate disease-associated biomolecular condensates.

7. References

1. Bondi MW, Edmonds EC, Salmon DP. Alzheimer's Disease: Past, Present, and Future. *J Int Neuropsychol Soc.* 2017;23(9-10):818-831.
2. Sveinbjornsdottir S. The clinical symptoms of Parkinson's disease. *J Neurochem.* 2016;139 Suppl 1:318-324.
3. Roos RA. Huntington's disease: a clinical review. *Orphanet J Rare Dis.* 2010;5:40.
4. Mitchell JD, Borasio GD. Amyotrophic lateral sclerosis. *Lancet.* 2007;369(9578):2031-2041.
5. Levenson RW, Sturm VE, Haase CM. Emotional and behavioral symptoms in neurodegenerative disease: a model for studying the neural bases of psychopathology. *Annu Rev Clin Psychol.* 2014;10:581-606.
6. Ferrari R, Kapogiannis D, Huey ED, Momeni P. FTD and ALS: a tale of two diseases. *Curr Alzheimer Res.* 2011;8(3):273-294.
7. Soto C. Unfolding the role of protein misfolding in neurodegenerative diseases. *Nat Rev Neurosci.* 2003;4(1):49-60.
8. Hussain R, Zubair H, Pursell S, Shahab M. Neurodegenerative Diseases: Regenerative Mechanisms and Novel Therapeutic Approaches. *Brain Sci.* 2018;8(9).
9. Hung CW, Chen YC, Hsieh WL, Chiou SH, Kao CL. Ageing and neurodegenerative diseases. *Ageing Res Rev.* 2010;9 Suppl 1:S36-46.
10. Hou Y, Dan X, Babbar M, et al. Ageing as a risk factor for neurodegenerative disease. *Nat Rev Neurol.* 2019;15(10):565-581.
11. Boudoulas KD, Triposkiadis F, Stefanadis C, Boudoulas H. The endlessness evolution of medicine, continuous increase in life expectancy and constant role of the physician. *Hellenic J Cardiol.* 2017;58(5):322-330.
12. Morris JC. Neurodegenerative disorders of aging: the down side of rising longevity. *Mo Med.* 2013;110(5):393-394.
13. Grundke-Iqbal I, Iqbal K, Quinlan M, Tung YC, Zaidi MS, Wisniewski HM. Microtubule-associated protein tau. A component of Alzheimer paired helical filaments. *J Biol Chem.* 1986;261(13):6084-6089.
14. Glenner GG, Wong CW. Alzheimer's disease: initial report of the purification and characterization of a novel cerebrovascular amyloid protein. *Biochem Biophys Res Commun.* 1984;120(3):885-890.

15. Spillantini MG, Schmidt ML, Lee VM, Trojanowski JQ, Jakes R, Goedert M. Alpha-synuclein in Lewy bodies. *Nature.* 1997;388(6645):839-840.
16. Bruijn LI, Houseweart MK, Kato S, et al. Aggregation and motor neuron toxicity of an ALS-linked SOD1 mutant independent from wild-type SOD1. *Science.* 1998;281(5384):1851-1854.
17. Arai T, Hasegawa M, Akiyama H, et al. TDP-43 is a component of ubiquitin-positive tau-negative inclusions in frontotemporal lobar degeneration and amyotrophic lateral sclerosis. *Biochem Biophys Res Commun.* 2006;351(3):602-611.
18. Neumann M, Sampathu DM, Kwong LK, et al. Ubiquitinated TDP-43 in frontotemporal lobar degeneration and amyotrophic lateral sclerosis. *Science.* 2006;314(5796):130-133.
19. Nolan M, Talbot K, Ansorge O. Pathogenesis of FUS-associated ALS and FTD: insights from rodent models. *Acta Neuropathol Commun.* 2016;4(1):99.
20. DiFiglia M, Sapp E, Chase KO, et al. Aggregation of huntingtin in neuronal intranuclear inclusions and dystrophic neurites in brain. *Science.* 1997;277(5334):1990-1993.
21. McClellan AJ, Tam S, Kaganovich D, Frydman J. Protein quality control: chaperones culling corrupt conformations. *Nat Cell Biol.* 2005;7(8):736-741.
22. Amm I, Sommer T, Wolf DH. Protein quality control and elimination of protein waste: the role of the ubiquitin-proteasome system. *Biochim Biophys Acta.* 2014;1843(1):182-196.
23. Chen B, Retzlaff M, Roos T, Frydman J. Cellular strategies of protein quality control. *Cold Spring Harb Perspect Biol.* 2011;3(8):a004374.
24. Luh LM, Bertolotti A. Potential benefit of manipulating protein quality control systems in neurodegenerative diseases. *Curr Opin Neurobiol.* 2020;61:125-132.
25. Mrdjen D, Fox EJ, Bukhari SA, Montine KS, Bendall SC, Montine TJ. The basis of cellular and regional vulnerability in Alzheimer's disease. *Acta Neuropathol.* 2019;138(5):729-749.
26. Horvath I, Iashchishyn IA, Moskalenko RA, et al. Co-aggregation of pro-inflammatory S100A9 with alpha-synuclein in Parkinson's disease: ex vivo and in vitro studies. *J Neuroinflammation.* 2018;15(1):172.
27. Dormann D, Haass C. TDP-43 and FUS: a nuclear affair. *Trends Neurosci.* 2011;34(7):339-348.

28. Sieradzan KA, Mechan AO, Jones L, Wanker EE, Nukina N, Mann DM. Huntington's disease intranuclear inclusions contain truncated, ubiquitinated huntingtin protein. *Exp Neurol.* 1999;156(1):92-99.
29. Kotzbauer PT, Giasson BI, Kravitz AV, et al. Fibrillization of alpha-synuclein and tau in familial Parkinson's disease caused by the A53T alpha-synuclein mutation. *Exp Neurol.* 2004;187(2):279-288.
30. Polymeropoulos MH, Lavedan C, Leroy E, et al. Mutation in the alpha-synuclein gene identified in families with Parkinson's disease. *Science.* 1997;276(5321):2045-2047.
31. Choi W, Zibaee S, Jakes R, et al. Mutation E46K increases phospholipid binding and assembly into filaments of human alpha-synuclein. *FEBS Lett.* 2004;576(3):363-368.
32. Chen LX, Xu HF, Wang PS, Yang XX, Wu ZY, Li HF. SOD1 Mutation Spectrum and Natural History of ALS Patients in a 15-Year Cohort in Southeastern China. *Front Genet.* 2021;12:746060.
33. Hatters DM. Protein misfolding inside cells: the case of huntingtin and Huntington's disease. *IUBMB Life.* 2008;60(11):724-728.
34. von Bergen M, Barghorn S, Li L, et al. Mutations of tau protein in frontotemporal dementia promote aggregation of paired helical filaments by enhancing local beta-structure. *J Biol Chem.* 2001;276(51):48165-48174.
35. Nacharaju P, Lewis J, Easson C, et al. Accelerated filament formation from tau protein with specific FTDP-17 missense mutations. *FEBS Lett.* 1999;447(2-3):195-199.
36. Guo W, Chen Y, Zhou X, et al. An ALS-associated mutation affecting TDP-43 enhances protein aggregation, fibril formation and neurotoxicity. *Nat Struct Mol Biol.* 2011;18(7):822-830.
37. Redler RL, Das J, Diaz JR, Dokholyan NV. Protein Destabilization as a Common Factor in Diverse Inherited Disorders. *J Mol Evol.* 2016;82(1):11-16.
38. A. Didonna FB. Post-translational modifications in neurodegeneration. *AIMS Biophysics.* 2015;3(1):27-49.
39. Min SW, Chen X, Tracy TE, et al. Critical role of acetylation in tau-mediated neurodegeneration and cognitive deficits. *Nat Med.* 2015;21(10):1154-1162.
40. Jeganathan S, Hascher A, Chinnathambi S, Biernat J, Mandelkow EM, Mandelkow E. Proline-directed pseudo-phosphorylation at AT8 and PHF1 epitopes induces a compaction of the paperclip folding of Tau and generates a pathological (MC-1) conformation. *J Biol Chem.* 2008;283(46):32066-32076.

41. Mondragon-Rodriguez S, Perry G, Luna-Munoz J, Acevedo-Aquino MC, Williams S. Phosphorylation of tau protein at sites Ser(396-404) is one of the earliest events in Alzheimer's disease and Down syndrome. *Neuropathol Appl Neurobiol.* 2014;40(2):121-135.
42. Lindwall G, Cole RD. Phosphorylation affects the ability of tau protein to promote microtubule assembly. *J Biol Chem.* 1984;259(8):5301-5305.
43. Alonso AC, Zaidi T, Grundke-Iqbal I, Iqbal K. Role of abnormally phosphorylated tau in the breakdown of microtubules in Alzheimer disease. *Proc Natl Acad Sci U S A.* 1994;91(12):5562-5566.
44. Alonso A, Zaidi T, Novak M, Grundke-Iqbal I, Iqbal K. Hyperphosphorylation induces self-assembly of tau into tangles of paired helical filaments/straight filaments. *Proc Natl Acad Sci U S A.* 2001;98(12):6923-6928.
45. Wolozin B, Ivanov P. Stress granules and neurodegeneration. *Nat Rev Neurosci.* 2019;20(11):649-666.
46. Skrabana R, Sevcik J, Novak M. Intrinsically disordered proteins in the neurodegenerative processes: formation of tau protein paired helical filaments and their analysis. *Cell Mol Neurobiol.* 2006;26(7-8):1085-1097.
47. Uversky VN. A protein-chameleon: conformational plasticity of alpha-synuclein, a disordered protein involved in neurodegenerative disorders. *J Biomol Struct Dyn.* 2003;21(2):211-234.
48. Loughlin FE, Wilce JA. TDP-43 and FUS-structural insights into RNA recognition and self-association. *Curr Opin Struct Biol.* 2019;59:134-142.
49. Santamaria N, Alhothali M, Alfonso MH, Breydo L, Uversky VN. Intrinsic disorder in proteins involved in amyotrophic lateral sclerosis. *Cell Mol Life Sci.* 2017;74(7):1297-1318.
50. Lim L, Wei Y, Lu Y, Song J. ALS-Causing Mutations Significantly Perturb the Self-Assembly and Interaction with Nucleic Acid of the Intrinsically Disordered Prion-Like Domain of TDP-43. *PLoS Biol.* 2016;14(1):e1002338.
51. Uversky VN. What does it mean to be natively unfolded? *Eur J Biochem.* 2002;269(1):2-12.
52. Tompa P. Intrinsically unstructured proteins. *Trends Biochem Sci.* 2002;27(10):527-533.
53. Uversky VN. Amyloidogenesis of natively unfolded proteins. *Curr Alzheimer Res.* 2008;5(3):260-287.

54. Zhang YJ, Gendron TF, Ebbert MTW, et al. Poly(GR) impairs protein translation and stress granule dynamics in C9orf72-associated frontotemporal dementia and amyotrophic lateral sclerosis. *Nat Med.* 2018;24(8):1136-1142.
55. Yang H, Hu HY. Sequestration of cellular interacting partners by protein aggregates: implication in a loss-of-function pathology. *FEBS J.* 2016;283(20):3705-3717.
56. Pedersen JT, Heegaard NH. Analysis of protein aggregation in neurodegenerative disease. *Anal Chem.* 2013;85(9):4215-4227.
57. Fitzpatrick AWP, Falcon B, He S, et al. Cryo-EM structures of tau filaments from Alzheimer's disease. *Nature.* 2017;547(7662):185-190.
58. Gremer L, Scholzel D, Schenk C, et al. Fibril structure of amyloid-beta(1-42) by cryo-electron microscopy. *Science.* 2017;358(6359):116-119.
59. Li Y, Zhao C, Luo F, et al. Amyloid fibril structure of alpha-synuclein determined by cryo-electron microscopy. *Cell Res.* 2018;28(9):897-903.
60. Li Q, Babinchak WM, Surewicz WK. Cryo-EM structure of amyloid fibrils formed by the entire low complexity domain of TDP-43. *Nat Commun.* 2021;12(1):1620.
61. Rochet JC, Lansbury PT, Jr. Amyloid fibrillogenesis: themes and variations. *Curr Opin Struct Biol.* 2000;10(1):60-68.
62. Sunde M, Blake C. The structure of amyloid fibrils by electron microscopy and X-ray diffraction. *Adv Protein Chem.* 1997;50:123-159.
63. Sunde M, Serpell LC, Bartlam M, Fraser PE, Pepys MB, Blake CC. Common core structure of amyloid fibrils by synchrotron X-ray diffraction. *J Mol Biol.* 1997;273(3):729-739.
64. Soto C. Protein misfolding and disease; protein refolding and therapy. *FEBS Lett.* 2001;498(2-3):204-207.
65. Horwich A. Protein aggregation in disease: a role for folding intermediates forming specific multimeric interactions. *J Clin Invest.* 2002;110(9):1221-1232.
66. Li J, Uversky VN, Fink AL. Effect of familial Parkinson's disease point mutations A30P and A53T on the structural properties, aggregation, and fibrillation of human alpha-synuclein. *Biochemistry.* 2001;40(38):11604-11613.
67. Uversky VN, Eliezer D. Biophysics of Parkinson's disease: structure and aggregation of alpha-synuclein. *Curr Protein Pept Sci.* 2009;10(5):483-499.
68. Scotter EL, Chen HJ, Shaw CE. TDP-43 Proteinopathy and ALS: Insights into Disease Mechanisms and Therapeutic Targets. *Neurotherapeutics.* 2015;12(2):352-363.

69. Barmada SJ, Skibinski G, Korb E, Rao EJ, Wu JY, Finkbeiner S. Cytoplasmic mislocalization of TDP-43 is toxic to neurons and enhanced by a mutation associated with familial amyotrophic lateral sclerosis. *J Neurosci.* 2010;30(2):639-649.
70. Vance C, Rogelj B, Hortobagyi T, et al. Mutations in FUS, an RNA processing protein, cause familial amyotrophic lateral sclerosis type 6. *Science.* 2009;323(5918):1208-1211.
71. Cattaneo E, Rigamonti D, Goffredo D, Zuccato C, Squitieri F, Sipione S. Loss of normal huntingtin function: new developments in Huntington's disease research. *Trends Neurosci.* 2001;24(3):182-188.
72. Dragatsis I, Levine MS, Zeitlin S. Inactivation of Hdh in the brain and testis results in progressive neurodegeneration and sterility in mice. *Nat Genet.* 2000;26(3):300-306.
73. Yang H, Li JJ, Liu S, et al. Aggregation of polyglutamine-expanded ataxin-3 sequesters its specific interacting partners into inclusions: implication in a loss-of-function pathology. *Sci Rep.* 2014;4:6410.
74. Donaldson KM, Li W, Ching KA, Batalov S, Tsai CC, Joazeiro CA. Ubiquitin-mediated sequestration of normal cellular proteins into polyglutamine aggregates. *Proc Natl Acad Sci U S A.* 2003;100(15):8892-8897.
75. Olzscha H, Schermann SM, Woerner AC, et al. Amyloid-like aggregates sequester numerous metastable proteins with essential cellular functions. *Cell.* 2011;144(1):67-78.
76. Shelkovnikova TA, Robinson HK, Southcombe JA, Ninkina N, Buchman VL. Multistep process of FUS aggregation in the cell cytoplasm involves RNA-dependent and RNA-independent mechanisms. *Hum Mol Genet.* 2014;23(19):5211-5226.
77. Yerbury JJ, Ooi L, Dillin A, et al. Walking the tightrope: proteostasis and neurodegenerative disease. *J Neurochem.* 2016;137(4):489-505.
78. Abramzon YA, Fratta P, Traynor BJ, Chia R. The Overlapping Genetics of Amyotrophic Lateral Sclerosis and Frontotemporal Dementia. *Front Neurosci.* 2020;14:42.
79. Couratier P, Corcia P, Lautrette G, Nicol M, Marin B. ALS and frontotemporal dementia belong to a common disease spectrum. *Rev Neurol (Paris).* 2017;173(5):273-279.
80. Ling SC, Polymenidou M, Cleveland DW. Converging mechanisms in ALS and FTD: disrupted RNA and protein homeostasis. *Neuron.* 2013;79(3):416-438.

81. DeJesus-Hernandez M, Mackenzie IR, Boeve BF, et al. Expanded GGGGCC hexanucleotide repeat in noncoding region of C9ORF72 causes chromosome 9p-linked FTD and ALS. *Neuron.* 2011;72(2):245-256.
82. Renton AE, Majounie E, Waite A, et al. A hexanucleotide repeat expansion in C9ORF72 is the cause of chromosome 9p21-linked ALS-FTD. *Neuron.* 2011;72(2):257-268.
83. Leskela S, Huber N, Rostalski H, et al. C9orf72 Proteins Regulate Autophagy and Undergo Autophagosomal or Proteasomal Degradation in a Cell Type-Dependent Manner. *Cells.* 2019;8(10).
84. Corbier C, Sellier C. C9ORF72 is a GDP/GTP exchange factor for Rab8 and Rab39 and regulates autophagy. *Small GTPases.* 2017;8(3):181-186.
85. Jackson JL, Finch NA, Baker MC, et al. Elevated methylation levels, reduced expression levels, and frequent contractions in a clinical cohort of C9orf72 expansion carriers. *Mol Neurodegener.* 2020;15(1):7.
86. Ciura S, Lattante S, Le Ber I, et al. Loss of function of C9orf72 causes motor deficits in a zebrafish model of amyotrophic lateral sclerosis. *Ann Neurol.* 2013;74(2):180-187.
87. Therrien M, Rouleau GA, Dion PA, Parker JA. Deletion of C9ORF72 results in motor neuron degeneration and stress sensitivity in C. elegans. *PLoS One.* 2013;8(12):e83450.
88. Waite AJ, Baumer D, East S, et al. Reduced C9orf72 protein levels in frontal cortex of amyotrophic lateral sclerosis and frontotemporal degeneration brain with the C9ORF72 hexanucleotide repeat expansion. *Neurobiol Aging.* 2014;35(7):1779 e1775-1779 e1713.
89. Mizielinska S, Gronke S, Niccoli T, et al. C9orf72 repeat expansions cause neurodegeneration in Drosophila through arginine-rich proteins. *Science.* 2014;345(6201):1192-1194.
90. Gendron TF, Bieniek KF, Zhang YJ, et al. Antisense transcripts of the expanded C9ORF72 hexanucleotide repeat form nuclear RNA foci and undergo repeat-associated non-ATG translation in c9FTD/ALS. *Acta Neuropathol.* 2013;126(6):829-844.
91. Ash PE, Bieniek KF, Gendron TF, et al. Unconventional translation of C9ORF72 GGGGCC expansion generates insoluble polypeptides specific to c9FTD/ALS. *Neuron.* 2013;77(4):639-646.

92. Mori K, Weng SM, Arzberger T, et al. The C9orf72 GGGGCC repeat is translated into aggregating dipeptide-repeat proteins in FTLD/ALS. *Science.* 2013;339(6125):1335-1338.
93. Zu T, Liu Y, Banez-Coronel M, et al. RAN proteins and RNA foci from antisense transcripts in C9ORF72 ALS and frontotemporal dementia. *Proc Natl Acad Sci U S A.* 2013;110(51):E4968-4977.
94. Lee YB, Chen HJ, Peres JN, et al. Hexanucleotide repeats in ALS/FTD form length-dependent RNA foci, sequester RNA binding proteins, and are neurotoxic. *Cell Rep.* 2013;5(5):1178-1186.
95. Reddy K, Zamiri B, Stanley SYR, Macgregor RB, Jr., Pearson CE. The disease-associated r(GGGGCC)n repeat from the C9orf72 gene forms tract length-dependent uni- and multimolecular RNA G-quadruplex structures. *J Biol Chem.* 2013;288(14):9860-9866.
96. Conlon EG, Lu L, Sharma A, et al. The C9ORF72 GGGGCC expansion forms RNA G-quadruplex inclusions and sequesters hnRNP H to disrupt splicing in ALS brains. *Elife.* 2016;5.
97. Lee KH, Zhang P, Kim HJ, et al. C9orf72 Dipeptide Repeats Impair the Assembly, Dynamics, and Function of Membrane-Less Organelles. *Cell.* 2016;167(3):774-788 e717.
98. Lin Y, Mori E, Kato M, et al. Toxic PR Poly-Dipeptides Encoded by the C9orf72 Repeat Expansion Target LC Domain Polymers. *Cell.* 2016;167(3):789-802 e712.
99. Freibaum BD, Taylor JP. The Role of Dipeptide Repeats in C9ORF72-Related ALS-FTD. *Front Mol Neurosci.* 2017;10:35.
100. Tang X, Toro A, T GS, et al. Divergence, Convergence, and Therapeutic Implications: A Cell Biology Perspective of C9ORF72-ALS/FTD. *Mol Neurodegener.* 2020;15(1):34.
101. Tran H, Almeida S, Moore J, et al. Differential Toxicity of Nuclear RNA Foci versus Dipeptide Repeat Proteins in a Drosophila Model of C9ORF72 FTD/ALS. *Neuron.* 2015;87(6):1207-1214.
102. Boeynaems S, Bogaert E, Kovacs D, et al. Phase Separation of C9orf72 Dipeptide Repeats Perturbs Stress Granule Dynamics. *Mol Cell.* 2017;65(6):1044-1055 e1045.
103. May S, Hornburg D, Schludi MH, et al. C9orf72 FTLD/ALS-associated Gly-Ala dipeptide repeat proteins cause neuronal toxicity and Unc119 sequestration. *Acta Neuropathol.* 2014;128(4):485-503.

104. Chang YJ, Jeng US, Chiang YL, Hwang IS, Chen YR. The Glycine-Alanine Dipeptide Repeat from C9orf72 Hexanucleotide Expansions Forms Toxic Amyloids Possessing Cell-to-Cell Transmission Properties. *J Biol Chem.* 2016;291(10):4903-4911.
105. Wen X, Tan W, Westergard T, et al. Antisense proline-arginine RAN dipeptides linked to C9ORF72-ALS/FTD form toxic nuclear aggregates that initiate in vitro and in vivo neuronal death. *Neuron.* 2014;84(6):1213-1225.
106. Hartmann H, Hornburg D, Czuppa M, et al. Proteomics and C9orf72 neuropathology identify ribosomes as poly-GR/PR interactors driving toxicity. *Life Sci Alliance.* 2018;1(2):e201800070.
107. Kanekura K, Yagi T, Cammack AJ, et al. Poly-dipeptides encoded by the C9ORF72 repeats block global protein translation. *Hum Mol Genet.* 2016;25(9):1803-1813.
108. Loveland AB, Svidritskiy E, Susorov D, et al. Ribosome inhibition by C9ORF72-ALS/FTD-associated poly-PR and poly-GR proteins revealed by cryo-EM. *Nat Commun.* 2022;13(1):2776.
109. Moens TG, Niccoli T, Wilson KM, et al. C9orf72 arginine-rich dipeptide proteins interact with ribosomal proteins in vivo to induce a toxic translational arrest that is rescued by eIF1A. *Acta Neuropathol.* 2019;137(3):487-500.
110. Boeynaems S, Bogaert E, Michiels E, et al. Drosophila screen connects nuclear transport genes to DPR pathology in c9ALS/FTD. *Sci Rep.* 2016;6:20877.
111. Hayes LR, Duan L, Bowen K, Kalab P, Rothstein JD. C9orf72 arginine-rich dipeptide repeat proteins disrupt karyopherin-mediated nuclear import. *Elife.* 2020;9.
112. Jovicic A, Mertens J, Boeynaems S, et al. Modifiers of C9orf72 dipeptide repeat toxicity connect nucleocytoplasmic transport defects to FTD/ALS. *Nat Neurosci.* 2015;18(9):1226-1229.
113. Hutten S, Usluer S, Bourgeois B, et al. Nuclear Import Receptors Directly Bind to Arginine-Rich Dipeptide Repeat Proteins and Suppress Their Pathological Interactions. *Cell Rep.* 2020;33(12):108538.
114. Kwon I, Xiang S, Kato M, et al. Poly-dipeptides encoded by the C9orf72 repeats bind nucleoli, impede RNA biogenesis, and kill cells. *Science.* 2014;345(6201):1139-1145.
115. White MR, Mitrea DM, Zhang P, et al. C9orf72 Poly(PR) Dipeptide Repeats Disturb Biomolecular Phase Separation and Disrupt Nucleolar Function. *Mol Cell.* 2019;74(4):713-728 e716.

116. Hyman AA, Weber CA, Julicher F. Liquid-liquid phase separation in biology. *Annu Rev Cell Dev Biol.* 2014;30:39-58.
117. Alberti S. Phase separation in biology. *Curr Biol.* 2017;27(20):R1097-R1102.
118. Nakashima KK, Vibhute MA, Spruijt E. Biomolecular Chemistry in Liquid Phase Separated Compartments. *Front Mol Biosci.* 2019;6:21.
119. Banani SF, Lee HO, Hyman AA, Rosen MK. Biomolecular condensates: organizers of cellular biochemistry. *Nat Rev Mol Cell Biol.* 2017;18(5):285-298.
120. Zhou L, Shi H, Li Z, He C. Recent Advances in Complex Coacervation Design from Macromolecular Assemblies and Emerging Applications. *Macromol Rapid Commun.* 2020;41(21):e2000149.
121. Najafi S, Lin Y, Longhini AP, et al. Liquid-liquid phase separation of Tau by self and complex coacervation. *Protein Sci.* 2021;30(7):1393-1407.
122. Dignon GL, Best RB, Mittal J. Biomolecular Phase Separation: From Molecular Driving Forces to Macroscopic Properties. *Annu Rev Phys Chem.* 2020;71:53-75.
123. Alberti S, Gladfelter A, Mittag T. Considerations and Challenges in Studying Liquid-Liquid Phase Separation and Biomolecular Condensates. *Cell.* 2019;176(3):419-434.
124. Bolognesi B, Lorenzo Gotor N, Dhar R, et al. A Concentration-Dependent Liquid Phase Separation Can Cause Toxicity upon Increased Protein Expression. *Cell Rep.* 2016;16(1):222-231.
125. Alberti S, Hyman AA. Biomolecular condensates at the nexus of cellular stress, protein aggregation disease and ageing. *Nat Rev Mol Cell Biol.* 2021;22(3):196-213.
126. Murthy AC, Dignon GL, Kan Y, et al. Molecular interactions underlying liquid-liquid phase separation of the FUS low-complexity domain. *Nat Struct Mol Biol.* 2019;26(7):637-648.
127. Elbaum-Garfinkle S, Kim Y, Szczepaniak K, et al. The disordered P granule protein LAF-1 drives phase separation into droplets with tunable viscosity and dynamics. *Proc Natl Acad Sci U S A.* 2015;112(23):7189-7194.
128. Molliex A, Temirov J, Lee J, et al. Phase separation by low complexity domains promotes stress granule assembly and drives pathological fibrillization. *Cell.* 2015;163(1):123-133.
129. Smith J, Calidas D, Schmidt H, Lu T, Rasoloson D, Seydoux G. Spatial patterning of P granules by RNA-induced phase separation of the intrinsically-disordered protein MEG-3. *Elife.* 2016;5.

130. Das S, Lin YH, Vernon RM, Forman-Kay JD, Chan HS. Comparative roles of charge, pi, and hydrophobic interactions in sequence-dependent phase separation of intrinsically disordered proteins. *Proc Natl Acad Sci U S A.* 2020;117(46):28795-28805.
131. Ukmar-Godec T, Hutten S, Grieshop MP, et al. Lysine/RNA-interactions drive and regulate biomolecular condensation. *Nat Commun.* 2019;10(1):2909.
132. Franzmann TM, Alberti S. Protein Phase Separation as a Stress Survival Strategy. *Cold Spring Harb Perspect Biol.* 2019;11(6).
133. Wang J, Choi JM, Holehouse AS, et al. A Molecular Grammar Governing the Driving Forces for Phase Separation of Prion-like RNA Binding Proteins. *Cell.* 2018;174(3):688-699 e616.
134. Alberti S, Halfmann R, King O, Kapila A, Lindquist S. A systematic survey identifies prions and illuminates sequence features of prionogenic proteins. *Cell.* 2009;137(1):146-158.
135. Li P, Banjade S, Cheng HC, et al. Phase transitions in the assembly of multivalent signalling proteins. *Nature.* 2012;483(7389):336-340.
136. Martin EW, Thomasen FE, Milkovic NM, et al. Interplay of folded domains and the disordered low-complexity domain in mediating hnRNPA1 phase separation. *Nucleic Acids Res.* 2021;49(5):2931-2945.
137. Campos-Melo D, Hawley ZCE, Droppelmann CA, Strong MJ. The Integral Role of RNA in Stress Granule Formation and Function. *Front Cell Dev Biol.* 2021;9:621779.
138. Mitrea DM, Kriwacki RW. Phase separation in biology; functional organization of a higher order. *Cell Commun Signal.* 2016;14:1.
139. Brangwynne CP, Mitchison TJ, Hyman AA. Active liquid-like behavior of nucleoli determines their size and shape in Xenopus laevis oocytes. *Proc Natl Acad Sci U S A.* 2011;108(11):4334-4339.
140. Gomes E, Shorter J. The molecular language of membraneless organelles. *J Biol Chem.* 2019;294(18):7115-7127.
141. Zhang JZ, Mehta S, Zhang J. Liquid-liquid phase separation: a principal organizer of the cell's biochemical activity architecture. *Trends Pharmacol Sci.* 2021;42(10):845-856.
142. Guzikowski AR, Chen YS, Zid BM. Stress-induced mRNP granules: Form and function of processing bodies and stress granules. *Wiley Interdiscip Rev RNA.* 2019;10(3):e1524.

143. Protter DSW, Parker R. Principles and Properties of Stress Granules. *Trends Cell Biol.* 2016;26(9):668-679.
144. Burke KA, Janke AM, Rhine CL, Fawzi NL. Residue-by-Residue View of In Vitro FUS Granules that Bind the C-Terminal Domain of RNA Polymerase II. *Mol Cell.* 2015;60(2):231-241.
145. Vanderweyde T, Youmans K, Liu-Yesucevitz L, Wolozin B. Role of stress granules and RNA-binding proteins in neurodegeneration: a mini-review. *Gerontology.* 2013;59(6):524-533.
146. Kim HJ, Kim NC, Wang YD, et al. Mutations in prion-like domains in hnRNPA2B1 and hnRNPA1 cause multisystem proteinopathy and ALS. *Nature.* 2013;495(7442):467-473.
147. Patel A, Lee HO, Jawerth L, et al. A Liquid-to-Solid Phase Transition of the ALS Protein FUS Accelerated by Disease Mutation. *Cell.* 2015;162(5):1066-1077.
148. Mackenzie IR, Nicholson AM, Sarkar M, et al. TIA1 Mutations in Amyotrophic Lateral Sclerosis and Frontotemporal Dementia Promote Phase Separation and Alter Stress Granule Dynamics. *Neuron.* 2017;95(4):808-816 e809.
149. Hernandez-Vega A, Braun M, Scharrel L, et al. Local Nucleation of Microtubule Bundles through Tubulin Concentration into a Condensed Tau Phase. *Cell Rep.* 2017;20(10):2304-2312.
150. Baradaran-Heravi Y, Van Broeckhoven C, van der Zee J. Stress granule mediated protein aggregation and underlying gene defects in the FTD-ALS spectrum. *Neurobiol Dis.* 2020;134:104639.
151. Li YR, King OD, Shorter J, Gitler AD. Stress granules as crucibles of ALS pathogenesis. *J Cell Biol.* 2013;201(3):361-372.
152. Lattante S, Rouleau GA, Kabashi E. TARDBP and FUS mutations associated with amyotrophic lateral sclerosis: summary and update. *Hum Mutat.* 2013;34(6):812-826.
153. Colombrita C, Zennaro E, Fallini C, et al. TDP-43 is recruited to stress granules in conditions of oxidative insult. *J Neurochem.* 2009;111(4):1051-1061.
154. Gopal PP, Nirschl JJ, Klinman E, Holzbaur EL. Amyotrophic lateral sclerosis-linked mutations increase the viscosity of liquid-like TDP-43 RNP granules in neurons. *Proc Natl Acad Sci U S A.* 2017;114(12):E2466-E2475.
155. Niaki AG, Sarkar J, Cai X, et al. Loss of Dynamic RNA Interaction and Aberrant Phase Separation Induced by Two Distinct Types of ALS/FTD-Linked FUS Mutations. *Mol Cell.* 2020;77(1):82-94 e84.

156. Sprunger ML, Jackrel ME. Prion-Like Proteins in Phase Separation and Their Link to Disease. *Biomolecules.* 2021;11(7).
157. Wegmann S, Eftekharzadeh B, Tepper K, et al. Tau protein liquid-liquid phase separation can initiate tau aggregation. *EMBO J.* 2018;37(7).
158. Rai SK, Savastano A, Singh P, Mukhopadhyay S, Zweckstetter M. Liquid-liquid phase separation of tau: From molecular biophysics to physiology and disease. *Protein Sci.* 2021;30(7):1294-1314.
159. Arendt T, Stieler JT, Holzer M. Tau and tauopathies. *Brain Res Bull.* 2016;126(Pt 3):238-292.
160. Yu H, Lu S, Gasior K, et al. HSP70 chaperones RNA-free TDP-43 into anisotropic intranuclear liquid spherical shells. *Science.* 2021;371(6529).
161. Liu Z, Zhang S, Gu J, et al. Hsp27 chaperones FUS phase separation under the modulation of stress-induced phosphorylation. *Nat Struct Mol Biol.* 2020;27(4):363-372.
162. Gu J, Liu Z, Zhang S, et al. Hsp40 proteins phase separate to chaperone the assembly and maintenance of membraneless organelles. *Proc Natl Acad Sci U S A.* 2020;117(49):31123-31133.
163. Guo L, Kim HJ, Wang H, et al. Nuclear-Import Receptors Reverse Aberrant Phase Transitions of RNA-Binding Proteins with Prion-like Domains. *Cell.* 2018;173(3):677-692 e620.
164. Hofweber M, Hutten S, Bourgeois B, et al. Phase Separation of FUS Is Suppressed by Its Nuclear Import Receptor and Arginine Methylation. *Cell.* 2018;173(3):706-719 e713.
165. Yoshizawa T, Ali R, Jiou J, et al. Nuclear Import Receptor Inhibits Phase Separation of FUS through Binding to Multiple Sites. *Cell.* 2018;173(3):693-705 e622.
166. Wang K, Liu JQ, Zhong T, et al. Phase Separation and Cytotoxicity of Tau are Modulated by Protein Disulfide Isomerase and S-nitrosylation of this Molecular Chaperone. *J Mol Biol.* 2020;432(7):2141-2163.
167. Hartl FU, Bracher A, Hayer-Hartl M. Molecular chaperones in protein folding and proteostasis. *Nature.* 2011;475(7356):324-332.
168. Priya S, Sharma SK, Goloubinoff P. Molecular chaperones as enzymes that catalytically unfold misfolded polypeptides. *FEBS Lett.* 2013;587(13):1981-1987.

169. Muntau AC, Leandro J, Staudigl M, Mayer F, Gersting SW. Innovative strategies to treat protein misfolding in inborn errors of metabolism: pharmacological chaperones and proteostasis regulators. *J Inherit Metab Dis.* 2014;37(4):505-523.
170. Lang K, Schmid FX, Fischer G. Catalysis of protein folding by prolyl isomerase. *Nature.* 1987;329(6136):268-270.
171. Schmid FX. Prolyl isomerase: enzymatic catalysis of slow protein-folding reactions. *Annu Rev Biophys Biomol Struct.* 1993;22:123-142.
172. Schmid FX, Mayr LM, Mucke M, Schonbrunner ER. Prolyl isomerases: role in protein folding. *Adv Protein Chem.* 1993;44:25-66.
173. Weiss MS, Jabs A, Hilgenfeld R. Peptide bonds revisited. *Nat Struct Biol.* 1998;5(8):676.
174. Theillet FX, Kalmar L, Tompa P, et al. The alphabet of intrinsic disorder: I. Act like a Pro: On the abundance and roles of proline residues in intrinsically disordered proteins. *Intrinsically Disord Proteins.* 2013;1(1):e24360.
175. Stewart DE, Sarkar A, Wampler JE. Occurrence and role of cis peptide bonds in protein structures. *J Mol Biol.* 1990;214(1):253-260.
176. Dugave C, Demange L. Cis-trans isomerization of organic molecules and biomolecules: implications and applications. *Chem Rev.* 2003;103(7):2475-2532.
177. Torchia DA. Evidence for cis peptide bonds in copolypeptides of glycine and proline. *Biochemistry.* 1972;11(8):1462-1468.
178. Sarkar SK, Young PE, Sullivan CE, Torchia DA. Detection of cis and trans X-Pro peptide bonds in proteins by 13C NMR: application to collagen. *Proc Natl Acad Sci U S A.* 1984;81(15):4800-4803.
179. Wedemeyer WJ, Welker E, Scheraga HA. Proline cis-trans isomerization and protein folding. *Biochemistry.* 2002;41(50):14637-14644.
180. Nicholson LK, Lu KP. Prolyl cis-trans Isomerization as a molecular timer in Crk signaling. *Mol Cell.* 2007;25(4):483-485.
181. Schmid FX. Prolyl isomerases. *Adv Protein Chem.* 2001;59:243-282.
182. Camilloni C, Sahakyan AB, Holliday MJ, et al. Cyclophilin A catalyzes proline isomerization by an electrostatic handle mechanism. *Proc Natl Acad Sci U S A.* 2014;111(28):10203-10208.
183. Nigro P, Pompilio G, Capogrossi MC. Cyclophilin A: a key player for human disease. *Cell Death Dis.* 2013;4:e888.

184. Zydowsky LD, Etzkorn FA, Chang HY, et al. Active site mutants of human cyclophilin A separate peptidyl-prolyl isomerase activity from cyclosporin A binding and calcineurin inhibition. *Protein Sci.* 1992;1(9):1092-1099.
185. Nath PR, Isakov N. Insights into peptidyl-prolyl cis-trans isomerase structure and function in immunocytes. *Immunol Lett.* 2015;163(1):120-131.
186. Russi S, Gonzalez A, Kenner LR, Keedy DA, Fraser JS, van den Bedem H. Conformational variation of proteins at room temperature is not dominated by radiation damage. *J Synchrotron Radiat.* 2017;24(Pt 1):73-82.
187. Schonbrunner ER, Mayer S, Tropschug M, Fischer G, Takahashi N, Schmid FX. Catalysis of protein folding by cyclophilins from different species. *J Biol Chem.* 1991;266(6):3630-3635.
188. Zhou HX. Influence of crowded cellular environments on protein folding, binding, and oligomerization: biological consequences and potentials of atomistic modeling. *FEBS Lett.* 2013;587(8):1053-1061.
189. van den Berg B, Ellis RJ, Dobson CM. Effects of macromolecular crowding on protein folding and aggregation. *EMBO J.* 1999;18(24):6927-6933.
190. Maneix LI, P.; Moree, S. E.; King, J. C. K.; Sykes, D. B.; Hill, C. T.; Saez, B.; Spooner, E.; Krause, D. S.; Sahin, E. Cyclophilin A regulates protein phase separation and mitigates haematopoietic stem cell aging. . *bioRxiv* 2021.
191. Baker JD, Shelton LB, Zheng D, et al. Human cyclophilin 40 unravels neurotoxic amyloids. *PLoS Biol.* 2017;15(6):e2001336.
192. Favretto F, Flores D, Baker JD, et al. Catalysis of proline isomerization and molecular chaperone activity in a tug-of-war. *Nat Commun.* 2020;11(1):6046.
193. Torpey J, Madine J, Wood A, Lian LY. Cyclophilin D binds to the acidic C-terminus region of alpha-Synuclein and affects its aggregation characteristics. *Sci Rep.* 2020;10(1):10159.
194. Gerard M, Debyser Z, Desender L, et al. The aggregation of alpha-synuclein is stimulated by FK506 binding proteins as shown by fluorescence correlation spectroscopy. *FASEB J.* 2006;20(3):524-526.
195. Gerard M, Deleersnijder A, Daniels V, et al. Inhibition of FK506 binding proteins reduces alpha-synuclein aggregation and Parkinson's disease-like pathology. *J Neurosci.* 2010;30(7):2454-2463.

196. Boeynaems S, Holehouse AS, Weinhardt V, et al. Spontaneous driving forces give rise to protein-RNA condensates with coexisting phases and complex material properties. *Proc Natl Acad Sci U S A.* 2019;116(16):7889-7898.
197. Fischer G, Wittmann-Liebold B, Lang K, Kiefhaber T, Schmid FX. Cyclophilin and peptidyl-prolyl cis-trans isomerase are probably identical proteins. *Nature.* 1989;337(6206):476-478.
198. Kabsch W. Xds. *Acta Crystallogr D Biol Crystallogr.* 2010;66(Pt 2):125-132.
199. McCoy AJ, Grosse-Kunstleve RW, Adams PD, Winn MD, Storoni LC, Read RJ. Phaser crystallographic software. *J Appl Crystallogr.* 2007;40(Pt 4):658-674.
200. Murshudov GN, Skubak P, Lebedev AA, et al. REFMAC5 for the refinement of macromolecular crystal structures. *Acta Crystallogr D Biol Crystallogr.* 2011;67(Pt 4):355-367.
201. Emsley P, Lohkamp B, Scott WG, Cowtan K. Features and development of Coot. *Acta Crystallogr D Biol Crystallogr.* 2010;66(Pt 4):486-501.
202. Mlynarik V. Introduction to nuclear magnetic resonance. *Anal Biochem.* 2017;529:4-9.
203. Bovey FA, Peter A. Mirau, and H. S. Gutowsky. *Nuclear magnetic resonance spectroscopy.* Vol 2: Elsevier; 1988.
204. Rule GS, Hitchens TK. *Fundamentals of Protein NMR Spectroscopy.* Vol 5: Springer.
205. Keeler J. *Understanding NMR Spectroscopy.* John Wiley & Sons, Inc.; 2002.
206. Butts CP, Jones CR, Towers EC, Flynn JL, Appleby L, Barron NJ. Interproton distance determinations by NOE--surprising accuracy and precision in a rigid organic molecule. *Org Biomol Chem.* 2011;9(1):177-184.
207. Jeener JMBHM, B. H.; Bachmann, P.; Ernst, R. R. Investigation of exchange processes by two-dimensional NMR spectroscopy. *J Chem Phys* 1979;71 (11):4546–4553.
208. Monneau YR, Soufari H, Nelson CJ, Mackereth CD. Structure and activity of the peptidyl-prolyl isomerase domain from the histone chaperone Fpr4 toward histone H3 proline isomerization. *J Biol Chem.* 2013;288(36):25826-25837.
209. Bodenhausen GR, D. J. Natural abundance nitrogen-15 NMR by enhanced heteronuclear spectroscopy. *Chemical Physics Letters.* 1980;69:185-189.
210. Becker W, Bhattiprolu KC, Gubensak N, Zangger K. Investigating Protein-Ligand Interactions by Solution Nuclear Magnetic Resonance Spectroscopy. *Chemphyschem.* 2018;19(8):895-906.

211. Purslow JA, Khatiwada B, Bayro MJ, Venditti V. NMR Methods for Structural Characterization of Protein-Protein Complexes. *Front Mol Biosci.* 2020;7:9.
212. Pellecchia M, Sem DS, Wuthrich K. NMR in drug discovery. *Nat Rev Drug Discov.* 2002;1(3):211-219.
213. Furukawa A, Konuma T, Yanaka S, Sugase K. Quantitative analysis of protein-ligand interactions by NMR. *Prog Nucl Magn Reson Spectrosc.* 2016;96:47-57.
214. Vranken WF, Boucher W, Stevens TJ, et al. The CCPN data model for NMR spectroscopy: development of a software pipeline. *Proteins.* 2005;59(4):687-696.
215. Damian L. Isothermal titration calorimetry for studying protein-ligand interactions. *Methods Mol Biol.* 2013;1008:103-118.
216. Wiseman T, Williston S, Brandts JF, Lin LN. Rapid measurement of binding constants and heats of binding using a new titration calorimeter. *Anal Biochem.* 1989;179(1):131-137.
217. Freibaum BD, Lu Y, Lopez-Gonzalez R, et al. GGGGCC repeat expansion in C9orf72 compromises nucleocytoplasmic transport. *Nature.* 2015;525(7567):129-133.
218. Zhang K, Donnelly CJ, Haeusler AR, et al. The C9orf72 repeat expansion disrupts nucleocytoplasmic transport. *Nature.* 2015;525(7567):56-61.
219. Kuglstatter A, Mueller F, Kusznir E, et al. Structural basis for the cyclophilin A binding affinity and immunosuppressive potency of E-ISA247 (voclosporin). *Acta Crystallogr D Biol Crystallogr.* 2011;67(Pt 2):119-123.
220. Choi H, Larsen B, Lin ZY, et al. SAINT: probabilistic scoring of affinity purification-mass spectrometry data. *Nat Methods.* 2011;8(1):70-73.
221. Zhao Y, Ke H. Mechanistic implication of crystal structures of the cyclophilin-dipeptide complexes. *Biochemistry.* 1996;35(23):7362-7368.
222. Schlegel J, Armstrong GS, Redzic JS, Zhang F, Eisenmesser EZ. Characterizing and controlling the inherent dynamics of cyclophilin-A. *Protein Sci.* 2009;18(4):811-824.
223. Schaller T, Ocwieja KE, Rasaiyaah J, et al. HIV-1 capsid-cyclophilin interactions determine nuclear import pathway, integration targeting and replication efficiency. *PLoS Pathog.* 2011;7(12):e1002439.
224. Marquez CL, Lau D, Walsh J, et al. Kinetics of HIV-1 capsid uncoating revealed by single-molecule analysis. *Elife.* 2018;7.
225. Balendra R, Isaacs AM. C9orf72-mediated ALS and FTD: multiple pathways to disease. *Nat Rev Neurol.* 2018;14(9):544-558.

226. Mikol V, Kallen J, Pflugl G, Walkinshaw MD. X-ray structure of a monomeric cyclophilin A-cyclosporin A crystal complex at 2.1 A resolution. *J Mol Biol.* 1993;234(4):1119-1130.
227. Eisenmesser EZ, Bosco DA, Akke M, Kern D. Enzyme dynamics during catalysis. *Science.* 2002;295(5559):1520-1523.
228. McGhee JD, von Hippel PH. Theoretical aspects of DNA-protein interactions: co-operative and non-co-operative binding of large ligands to a one-dimensional homogeneous lattice. *J Mol Biol.* 1974;86(2):469-489.
229. Zhang X, Vigers M, McCarty J, et al. The proline-rich domain promotes Tau liquid-liquid phase separation in cells. *J Cell Biol.* 2020;219(11).
230. Darling AL, Dahrendorff J, Creodore SG, Dickey CA, Blair LJ, Uversky VN. Small heat shock protein 22 kDa can modulate the aggregation and liquid-liquid phase separation behavior of tau. *Protein Sci.* 2021;30(7):1350-1359.

8. Appendix

8.1. Protein and plasmid sequences

8.1.1. Wild type PPIA

Protein Sequence:
MGSSHHHHHHSSGLVPRGSHMASENLYFQ/GGSMVNPTVFFDIAVDGEPLGRVSFELFADKV
PKTAENFRALSTGEKGFGYKGSCFHRIIPGFMCQGGDFTRHNGTGGKSIYGEKFEDENFILKH
TGPGILSMANAGPNTNGSQFFICTAKTEWLDGKHVVFGKVKEGMNIVEAMERFGSRNGKTS
KKITIADCGQLE

Plasmid sequence:
ATGGGCAGCAGCCATCATCATCATCATCACAGCAGCGGCCTGGTGCCGCGCGGCAGCCA
TATGGCTAGCGAAAACCTGTATTTTCAGGGCGGATCCATGGTCAACCCCACCGTGTTCTT
CGACATTGCCGTCGACGGCGAGCCCTTGGGCCGCGTCTCCTTTGAGCTGTTTGCAGACAA
GGTCCCAAAGACAGCAGAAAATTTTCGTGCTCTGAGCACTGGAGAGAAAGGATTTGGTT
ATAAGGGTTCCTGCTTTCACAGAATTATTCCAGGGTTTATGTGTCAGGGTGGTGACTTCA
CACGCCATAATGGCACTGGTGGCAAGTCCATCTATGGGGAGAAATTTGAAGATGAGAAC
TTCATCCTAAAGCATACGGGTCCTGGCATCTTGTCCATGGCAAATGCTGGACCCAACACA
AATGGTTCCCAGTTTTTCATCTGCACTGCCAAGACTGAGTGGTTGGATGGCAAGCATGTG
GTGTTTGGCAAAGTGAAAGAAGGCATGAATATTGTGGAGGCCATGGAGCGCTTTGGGTC
CAGGAATGGCAAGACCAGCAAGAAGATCACCATTGCTGACTGTGGACAACTCGAATAA

8.1.2. Mutant PPIA(R55A)

Protein Sequence:
MGSSHHHHHHSSGLVPRGSHMASENLYFQ/GGSMVNPTVFFDIAVDGEPLGRVSFELFADKV
PKTAENFRALSTGEKGFGYKGSCFHAIIPGFMCQGGDFTRHNGTGGKSIYGEKFEDENFILKH
TGPGILSMANAGPNTNGSQFFICTAKTEWLDGKHVVFGKVKEGMNIVEAMERFGSRNGKTS
KKITIADCGQLE

Plasmid sequence:
ATGGGCAGCAGCCATCATCATCATCATCACAGCAGCGGCCTGGTGCCGCGCGGCAGCCA
TATGGCTAGCGAAAACCTGTATTTTCAGGGCGGATCCATGGTCAACCCCACCGTGTTCTT
CGACATTGCCGTCGACGGCGAGCCCTTGGGCCGCGTCTCCTTTGAGCTGTTTGCAGACAA
GGTCCCAAAGACAGCAGAAAATTTTCGTGCTCTGAGCACTGGAGAGAAAGGATTTGGTT
ATAAGGGTTCCTGCTTTCACGCAATTATTCCAGGGTTTATGTGTCAGGGTGGTGACTTCA
CACGCCATAATGGCACTGGTGGCAAGTCCATCTATGGGGAGAAATTTGAAGATGAGAAC
TTCATCCTAAAGCATACGGGTCCTGGCATCTTGTCCATGGCAAATGCTGGACCCAACACA
AATGGTTCCCAGTTTTTCATCTGCACTGCCAAGACTGAGTGGTTGGATGGCAAGCATGTG
GTGTTTGGCAAAGTGAAAGAAGGCATGAATATTGTGGAGGCCATGGAGCGCTTTGGGTC
CAGGAATGGCAAGACCAGCAAGAAGATCACCATTGCTGACTGTGGACAACTCGAATAA

8.1.3. Tau

Protein Sequence:
MAEPRQEFEVMEDHAGTYGLGDRKDQGGYTMHQDQEGDTDAGLKESPLQTPTEDGSEEPG
SETSDAKSTPTAEDVTAPLVDEGAPGKQAAAQPHTEIPEGTTAEEAGIGDTPSLEDEAAGHVT
QARMVSKSKDGTGSDDKKAKGADGKTKIATPRGAAPPGQKGQANATRIPAKTPPAPKTPPSS
GEPPKSGDRSGYSSPGSPGTPGSRSRTPSLPTPPTREPKKVAVVRTPPKSPSSAKSRLQTAPVP
MPDLKNVKSKIGSTENLKHQPGGGKVQIINKKLDLSNVQSKCGSKDNIKHVPGGGSVQIVYK
PVDLSKVTSKCGSLGNIHHKPGGGQVEVKSEKLDFKDRVQSKIGSLDNITHVPGGGNKKIET
HKLTFRENAKAKTDHGAEIVYKSPVVSGDTSPRHLSNVSSTGSIDMVDSPQLATLADEVSASL
AKQGL

Plasmid Sequence:
ATGGCTGAGCCCCGCCAGGAGTTCGAAGTGATGGAAGATCACGCTGGGACGTACGGGTT
GGGGGACAGGAAAGATCAGGGGGGCTACACCATGCACCAAGACCAAGAGGGTGACACG
GACGCTGGCCTGAAAGAATCTCCCCTGCAGACCCCCACTGAGGACGGATCTGAGGAACC
GGGCTCTGAAACCTCTGATGCTAAGAGCACTCCAACAGCGGAAGATGTGACAGCACCCT
TAGTGGATGAGGGAGCTCCCGGCAAGCAGGCTGCCGCGCAGCCCCACACGGAGATCCCA
GAAGGAACCACAGCTGAAGAAGCAGGCATTGGAGACACCCCCAGCCTGGAAGACGAAG
CTGCTGGTCACGTGACCCAAGCTCGCATGGTCAGTAAAAGCAAAGACGGGACTGGAAGC
GATGACAAAAAAGCCAAGGGGGCTGATGGTAAAACGAAGATCGCCACACCGCGGGGAG
CAGCCCCTCCAGGCCAGAAGGGCCAGGCCAACGCCACCAGGATTCCAGCAAAAACCCCG
CCCGCTCCAAAGACACCACCCAGCTCTGGTGAACCTCCAAAATCAGGGGATCGCAGCGG
CTACAGCAGCCCCGGCTCCCCAGGCACTCCCGGCAGCCGCTCCCGCACCCCGTCCCTTCC
AACCCCACCCACCCGGGAGCCCAAGAAGGTGGCAGTGGTCCGTACTCCACCCAAGTCGC
CGTCTTCCGCCAAGAGCCGCCTGCAGACAGCCCCCGTGCCCATGCCAGACCTGAAGAAT
GTCAAGTCCAAGATCGGCTCCACTGAGAACCTGAAGCACCAGCCGGGAGGCGGGAAGGT
GCAGATAATTAATAAGAAGCTGGATCTTAGCAACGTCCAGTCCAAGTGTGGCTCAAAGG
ATAATATCAAACACGTCCCGGGAGGCGGCAGTGTGCAAATAGTCTACAAACCAGTTGAC
CTGAGCAAGGTGACCTCCAAGTGTGGCTCATTAGGCAACATCCATCATAAACCAGGAGG
TGGCCAGGTGGAAGTAAAATCTGAGAAGCTTGACTTCAAGGACAGAGTCCAGTCGAAGA
TTGGGTCCCTGGACAATATCACCCACGTCCCTGGCGGAGGAAATAAAAAGATTGAAACC
CACAAGCTGACCTTCCGCGAGAACGCCAAAGCCAAGACAGACCACGGGGCGGAGATCGT
GTACAAGTCGCCAGTGGTGTCTGGGGACACGTCTCCACGGCATCTCAGCAATGTCTCCTC
CACCGGCAGCATCGACATGGTAGACTCGCCCCAGCTCGCCACGCTAGCTGACGAGGTGT
CTGCCTCCCTGGCCAAGCAGGGTTTG

8.2. Supplementary Figures

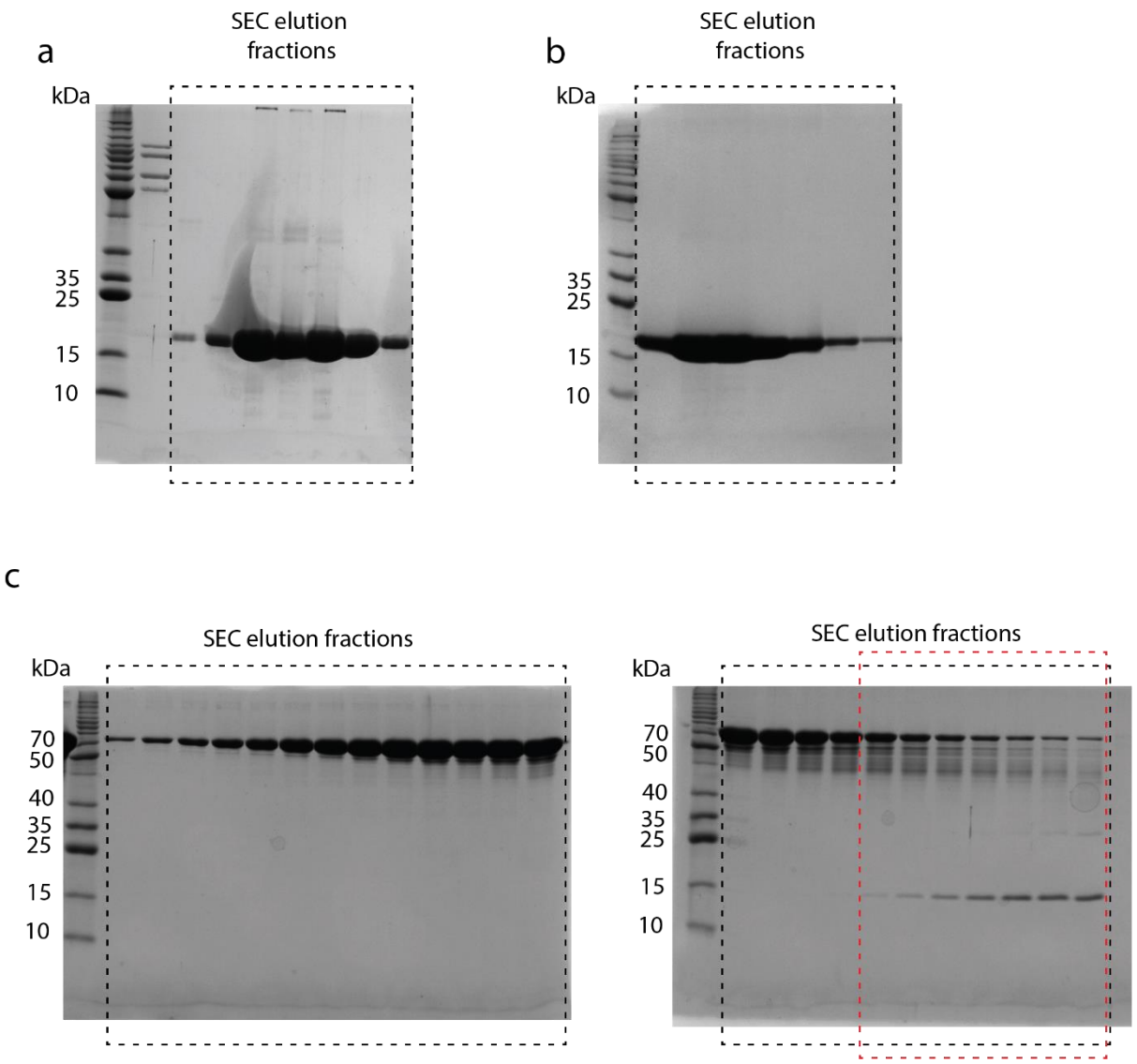

Supplementary Figure 1: SDS gels of purified proteins.

Fraction collected after gel filtration(shown inside black dotted column) of a) PPIA b) PPIA(R55A) and c) Tau tested on an SDS gel for its purity. For PPIA and PPIA(R55A), all the tested fractions were pure. For Tau, the fractions that contained impurity (marked in a dotted red box) were removed and the remaining fractions were pooled together.

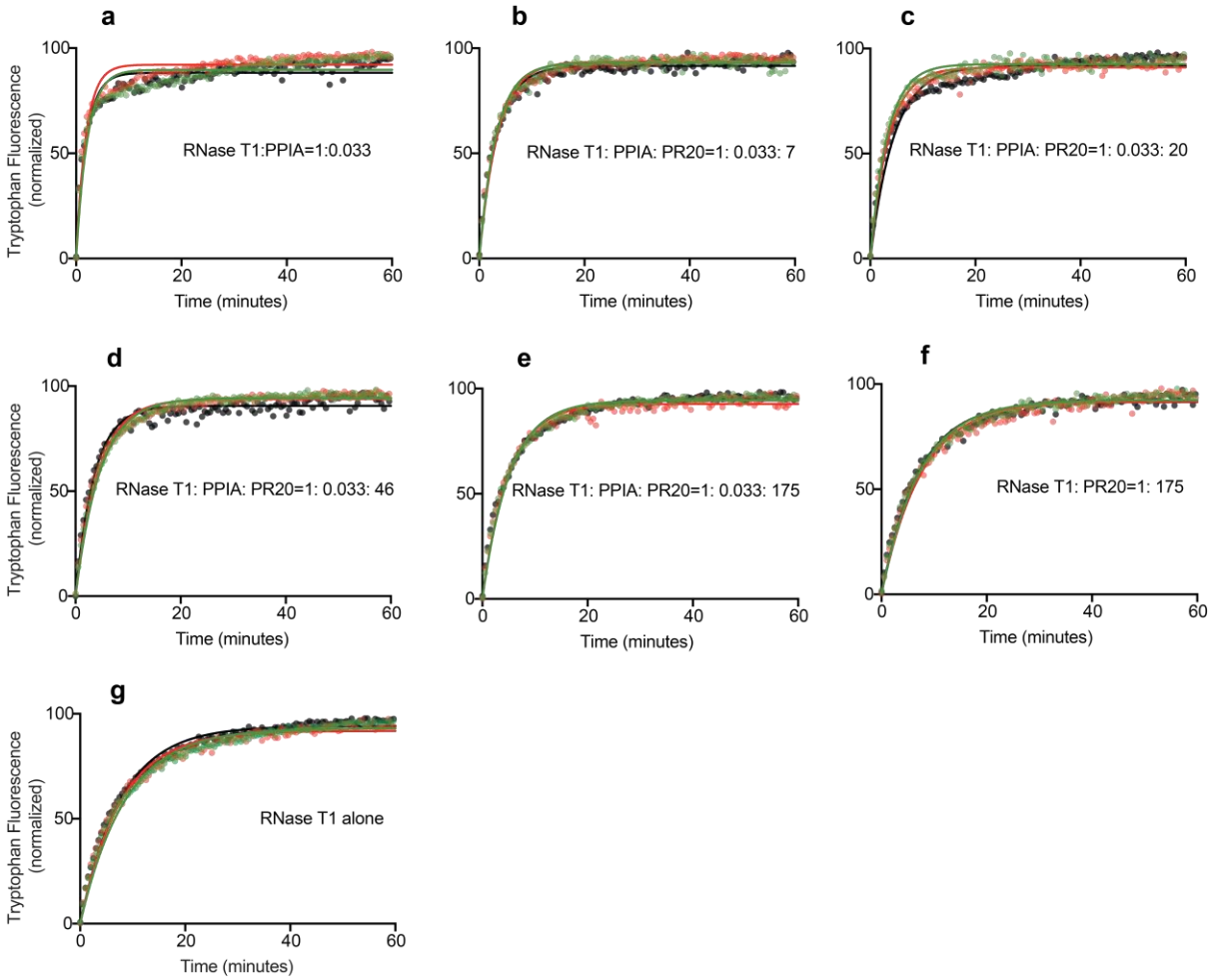

Supplementary Figure 2: Individual refolding curves of RNaseT1.

Green, pink and black dotted lines represent the three replicates of RNaseT1 folding under the conditions a) RNaseT1:PPIA=1:0.033, b) RNaseT1:PPIA:PR20=1:0.033:7, c) RNaseT1:PPIA:PR20=1:0.033:20, d) RNaseT1:PPIA:PR20=1:0.033:46, e) RNaseT1:PPIA:PR20=1:0.033:175, f) RNaseT1: PR20=1:175 and g) RNaseT1 alone. Mono-exponential fits corresponding to each replicate are shown in same colours using continuous lines. (Figure is reprinted from **Babu, Maria**, **et al.** Nature communications 12.1, 3396 (2021), with permission from Springer Nature.)

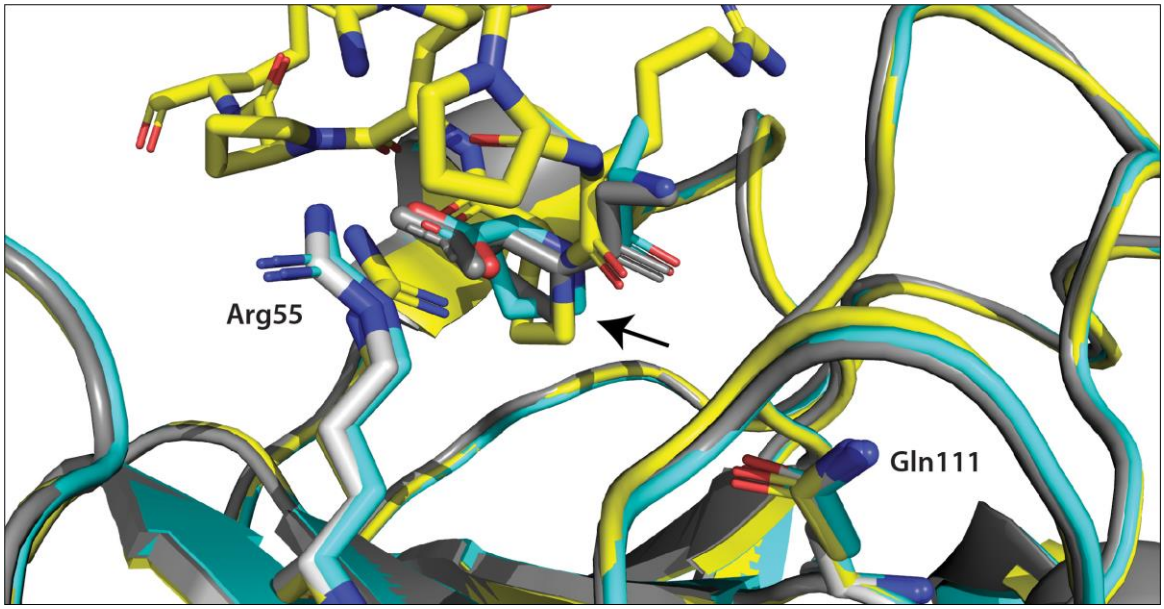

Supplementary Figure 3: Comparison of the structure of the active site of PPIA bound to PR20 and other Xaa-proline dipeptides.

PR20 (this work; yellow) and Xaa-proline dipeptides (grey; PDB code 5CYH; https://www.wwpdb.org/pdb?id=pdb_00005cyh; cyan PDB code 2CYH; https://www.wwpdb.org/pdb?id=pdb_00002cyh)[223] are compared in their complex with PPIA. The side chain of Arg55, which is critical for substrate binding and catalytic activity of PPIA, is labelled. Gln111 of PPIA does not make direct contacts with the substrates, but is part of a dynamic network of residues in the binding pocket[224]. The proline of the substrate is marked by an arrow. (Figure is reprinted from Babu, Maria, et al. Nature communications 12.1, 3396 (2021), with permission from Springer Nature.)

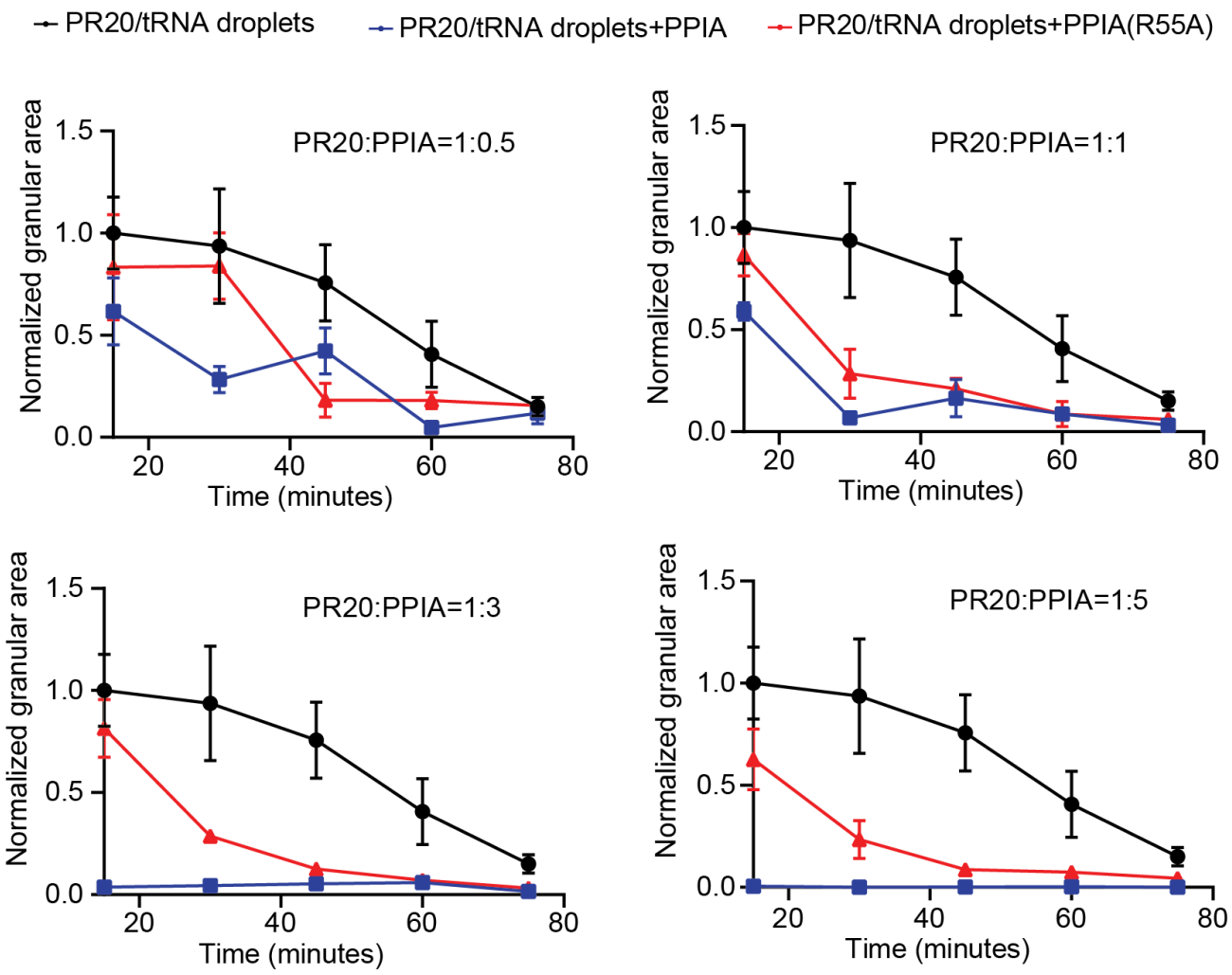

Supplementary Figure 4: Time dependent observation of PR20/tRNA droplets.

Average granular area occupied by PR20/tRNA droplets after addition of wild-type PPIA (blue) or mutant PPIA(R55A) (red), followed in time. Average granular area in a control sample without any PPIA variant is displayed in black. Error bars represent the standard deviation from average area calculated from four different micrographs. (Figure is reprinted with permission from Babu, Maria, et al. Journal of the American Chemical Society144.35, 16157-16163 (2022). Copyright 2022 American Chemical Society)

8.3. X-Ray data

Supplementary Table 1: X-ray data collection statistics.

(Reprinted from **Babu, Maria**, **et al.** Nature communications 12.1, 3396 (2021), with permission from Springer Nature.)

.

Data statistics	**PR20/CypA-complex**
Wavelength	1.0 Å
Beamline	SLS-X10SA
Detector	Dectris EIGER2 16M
Space group	$P6_1$
a	83.32 Å
b	83.32 Å
c	52.45 Å
α, β	90°
γ	120°
Resolution[a]	42.47-1.31 Å (1.34-1.31 Å)
Reflections measured	1,005,075
Unique reflections	49,424
Redundancy	20.06 (17.27)
Completeness(%)	98.7 (95.27)
Mean $I/\sigma(I)$	21.55 (1.6)
R_{int} (%)	6.56 (79.39)
R_{rim} (%)	3.7 (50)

[a]Values in parentheses are outer-resolution shell.

Supplementary Table 2: X-ray structure refinement statistics of the PR20/PPIA-complex.

(Reprinted from **Babu, Maria**, **et al.** Nature communications 12.1, 3396 (2021), with permission from Springer Nature.)

R-factor	13.4%
R_{free}[a]	16.6%
Solvent	55.68%
Mean B-value (Å^2)	
chain A	28.32
chain B	30.44
waters	40.76
No. of protein residues	171
No. of water residues	163
Root mean square deviations from ideal geometry	
Bond lengths	0.019 Å
Bond angles	2.14°
Ramachandran plot (%)	
Favoured	93.75
Allowed	6.25
Outliers	0

[a]R_{free} was determined using 5% of the data.

8.4. Resonance Assignments

Supplementary Table 3: Resonance Assignments of Wild Type PPIA

Condition: 25 mM HEPES, 100 mM NaCl, 1 mM DTT, 10% D_2O, pH 7.4, 298 K

Residues	F1 dimension	F2 Dimension
1Met	8.41703	122.5477
2Val	8.02542	121.3352
3Asn	8.5377	126.5397
5Thr	8.71615	115.0606
6Val	8.67841	120.385
7Phe	8.89095	119.2596
8Phe	9.48375	117.0429
9Asp	9.20859	124.2594
10Ile	8.97213	124.3419
11Ala	9.5528	132.5519
12Val	8.87387	118.4926
13Asp	9.78326	131.0921
14Gly	8.48993	101.7577
15Glu	7.98026	123.3666
17Leu	9.1272	126.1023
18Gly	7.17965	102.55
19Arg	8.28164	121.2996
20Val	9.30329	126.9439
21Ser	8.70324	120.3519
22Phe	9.44432	119.1031
23Glu	8.68006	123.2557
24Leu	8.10676	122.5483
25Phe	8.76536	124.7785
26Ala	8.36596	129.0443
27Asp	8.98416	114.3988
28Lys	7.47738	118.1274
29Val	8.30657	114.6812
31Lys	10.59685	123.8566
32Thr	10.21461	124.1034
33Ala	9.22297	125.737
34Glu	7.95942	117.3003
35Asn	7.06389	115.6711
36Phe	6.95251	117.9551
37Arg	8.87547	121.1381
38Ala	8.62526	119.1649
39Leu	8.11847	120.8006
40Ser	7.82738	119.3178
41Thr	7.91492	108.5391
42Gly	7.51462	108.3896
43Glu	7.9474	118.7723
44Lys	9.03984	118.545
45Gly	7.87111	105.6154

46Phe	6.35399	113.7647
47Gly	7.67499	104.7133
48Tyr	6.83431	113.8393
49Lys	8.40896	124.964
50Gly	9.41404	117.939
51Ser	8.32064	116.5247
52Cys	9.94816	115.334
53Phe	8.63542	123.0894
54His	7.53825	120.1923
55Arg	6.9775	123.204
56Ile	9.11056	126.5134
57Ile	8.65942	128.0119
59Gly	9.6757	114.2764
60Phe	8.10172	119.3521
61Met	8.01564	111.2045
62Cys	8.40601	114.9053
63Gln	9.58333	126.7253
64Gly	7.29255	110.8386
65Gly	9.28583	106.0149
66Asp	9.89511	124.0536
67Phe	6.55785	116.0784
68Thr	7.21943	108.97
69Arg	8.59716	122.0683
71Asn	7.42789	112.4481
72Gly	9.6071	110.6567
73Thr	7.86073	112.1878
74Gly	8.64841	114.0623
75Gly	8.03143	109.0659
76Lys	6.92161	115.4998
77Ser	7.65588	114.3455
78Ile	8.49085	111.33
79Tyr	7.98084	120.8942
80Gly	7.01776	106.4814
82Lys	7.7481	112.1274
83Phe	9.09295	116.5759
84Glu	9.1798	119.5562
85Asp	8.52869	118.8961
86Glu	9.39701	131.8023
87Asn	6.98143	106.8379
88Phe	8.26833	113.0036
89Ile	8.23722	119.9138
90Leu	7.67664	117.2989
91Lys	7.99766	119.0008
92His	10.63908	122.5981
93Thr	7.19118	110.483
94Gly	7.4232	107.335
96Gly	9.20712	110.3099
97Ile	6.69601	121.4729
98Leu	7.81415	128.8718
99Ser	8.2234	118.7521

100Met	8.48324	123.0586
101Ala	7.92321	125.9638
102Asn	8.03563	113.4284
103Ala	8.71047	123.4162
104Gly	8.11951	109.4138
106Asn	8.79901	119.1524
107Thr	10.14642	110.361
108Asn	7.30178	120.6551
109Gly	9.10552	110.7996
110Ser	8.69425	117.1333
111Gln	8.30831	124.507
112Phe	7.99233	117.8902
113Phe	9.73842	116.5513
114Ile	9.03984	118.545
115Cys	9.53795	125.554
116Thr	8.88208	115.767
117Ala	7.54	122.2741
118Lys	8.62329	119.862
119Thr	7.26519	119.1141
120Glu	9.01801	124.6321
121Trp	7.18192	117.8977
122Leu	6.95544	120.0621
123Asp	7.54	122.2741
124Gly	9.46407	111.3194
125Lys	7.66719	115.6597
126His	7.50023	119.9018
127Val	8.40948	124.9601
128Val	9.40624	133.0835
129Phe	8.03716	117.9021
130Gly	7.23898	110.8054
131Lys	8.28885	115.3273
132Val	8.96091	124.1956
133Lys	9.39701	131.8023
134Glu	7.47341	118.5122
135Gly	8.61428	108.0371
136Met	8.78163	122.6382
137Asn	8.84041	114.5091
138Ile	7.57529	124.3082
139Val	7.17952	122.0105
140Glu	8.22961	117.4233
141Ala	7.42992	121.109
142Met	8.20523	117.7268
143Glu	7.7729	116.4378
144Arg	6.96519	114.6257
145Phe	7.55971	115.4477
146Gly	7.45499	104.7884
147Ser	8.13798	110.0482
149Asn	7.81088	111.63
150Gly	7.97429	110.2652
151Lys	7.46113	119.9168

152Thr	8.7808	116.8136
153Ser	9.35034	117.0883
154Lys	7.46616	119.383
155Lys	8.72939	121.8806
156Ile	9.53855	134.4216
157Thr	9.17943	117.1418
158Ile	8.51892	121.7229
159Ala	8.81086	132.5717
160Asp	7.99694	111.5954
161Cys	8.52339	116.1621
162Gly	6.77736	104.1873
163Gln	8.99201	121.0616
164Leu	8.51077	126.113
165Glu	8.07086	126.3354

Supplementary Table 4: Resonance Assignments of mutant PPIA(R55A)

Condition: 25 mM HEPES, 100 mM NaCl, 1 mM DTT, 10 % D_2O, pH 7.4, 298 K

Assign F1	Position F1	Position F2
1Met	8.4179	122.5605
2Val	8.02518	121.3422
3Asn	8.53521	126.5342
5Thr	8.71281	115.0791
6Val	8.6753	120.4703
7Phe	8.8926	119.301
8Phe	9.48715	117.0589
9Asp	9.2082	124.3063
10Ile	8.96533	124.3144
11Ala	9.54709	132.5731
12Val	8.88355	118.5042
13Asp	9.78027	131.1036
14Gly	8.48993	101.7577
15Glu	7.98329	123.409
17Leu	9.12801	126.1378
18Gly	7.18393	102.54
19Arg	8.27895	121.3047
20Val	9.30392	126.9956
21Ser	8.70375	120.3771
22Phe	9.45267	119.1561
23Glu	8.67766	123.2813
24Leu	8.10747	122.5709
25Phe	8.76455	124.7926
26Ala	8.37014	129.0667
27Asp	8.99261	114.424
28Lys	7.48143	118.1524
29Val	8.30712	114.6203
31Lys	10.58761	123.8933
32Thr	10.21581	124.119
33Ala	9.22943	125.748
34Glu	7.95914	117.2974
35Asn	7.06246	115.7333
36Phe	6.95399	117.976
37Arg	8.88355	121.1843
38Ala	8.63003	119.1872
39Leu	8.11524	120.8491
40Ser	7.83102	119.3661
41Thr	7.91991	108.5728
42Gly	7.51377	108.4072
43Glu	7.94161	118.7963
44Lys	9.03838	118.5214
45Gly	7.86688	105.6444
46Phe	6.36204	113.7787
47Gly	7.67088	104.6694
48Tyr	6.84767	114.0384

49Lys	8.43166	125.1022
50Gly	9.40222	118.0282
51Ser	8.30019	116.5795
52Cys	9.9823	115.2759
53Phe	8.61678	123.1357
54His	7.39865	120.5841
55Ala	7.0571	124.284
56Ile	9.11271	123.2785
57Ile	8.75032	128.4764
59Gly	9.63893	114.2203
60Phe	8.12479	119.3847
61Met	8.05185	111.6046
62Cys	8.44434	115.4575
63Gln	9.69196	126.1885
64Gly	7.29105	111.1949
65Gly	9.36083	106.1514
66Asp	9.98903	124.2415
67Phe	6.56887	115.8372
68Thr	7.19945	108.8211
69Arg	8.61412	122.129
71Asn	7.4878	112.4259
72Gly	9.52381	110.4664
73Thr	7.83713	112.0289
74Gly	8.64914	114.2337
75Gly	8.05961	109.235
76Lys	6.92916	115.4871
77Ser	7.68255	114.4744
78Ile	8.48516	111.2632
79Tyr	7.98329	120.9463
80Gly	7.03005	106.5723
82Lys	7.76507	112.449
83Phe	9.11376	116.6561
84Glu	9.18363	119.57
85Asp	8.53043	118.9181
86Glu	9.40352	131.8384
87Asn	6.98349	106.8517
88Phe	8.26478	113.0041
89Ile	8.23687	119.9327
90Leu	7.68062	117.3246
91Lys	7.99105	119.0112
92His	10.64301	122.6301
93Thr	7.19169	110.4664
94Gly	7.42492	107.3612
96Gly	9.21079	110.2594
97Ile	6.70014	121.501
98Leu	7.80609	128.8593
99Ser	8.20815	118.7677
100Met	8.47995	123.036
101Ala	7.87723	126.1068
102Asn	8.14031	113.4733

103Ala	8.70137	123.3588
104Gly	8.12877	109.4373
106Asn	8.79947	119.1665
107Thr	10.15761	110.456
108Asn	7.30712	120.5982
109Gly	9.1306	110.8493
110Ser	8.70861	117.2616
111Gln	8.27303	124.6064
112Phe	8.02847	117.9655
113Phe	9.72818	116.7037
114Ile	9.03838	118.5214
115Cys	9.53499	125.6056
116Thr	8.88355	115.8552
117Ala	7.53964	122.2708
118Lys	8.61709	119.8494
119Thr	7.26671	119.1872
120Glu	9.00139	124.5396
121Trp	7.1904	117.9454
122Leu	6.9472	120.1157
123Asp	7.53964	122.2811
124Gly	9.47149	111.3353
125Lys	7.66639	115.7414
126His	7.49762	119.8493
127Val	8.41414	124.8993
128Val	9.40505	133.1109
129Phe	8.02571	117.9576
130Gly	7.24436	110.8004
131Lys	8.2795	115.3482
132Val	8.95727	124.2132
133Lys	9.40352	131.8591
134Glu	7.47884	118.5353
135Gly	8.60842	108.068
136Met	8.7782	122.6438
137Asn	8.83698	114.4996
138Ile	7.58361	124.3684
139Val	7.16487	122.0096
140Glu	8.22	117.366
141Ala	7.44974	121.2627
142Met	8.19588	117.7378
143Glu	7.71272	116.1477
144Arg	7.00124	114.7822
145Phe	7.57371	115.4955
146Gly	7.41842	104.6552
147Ser	8.23608	110.2147
149Asn	7.72123	111.7291
150Gly	7.94806	109.9683
151Lys	7.40868	119.6047
152Thr	8.78032	116.8761
153Ser	9.35049	117.1487
154Lys	7.4672	119.3941

155Lys	8.73513	121.9563
156Ile	9.55744	134.5288
157Thr	9.16423	117.0452
158Ile	8.51879	121.6913
159Ala	8.79947	132.4903
160Asp	7.99632	111.617
161Cys	8.52696	116.1759
162Gly	6.77395	104.1509
163Gln	8.99478	121.0911
164Leu	8.5162	126.1378
165Glu	8.0725	126.3422